Ocean Dynamics and Ice Fractures

Insights from Earth and Beyond

Poinelli, M.

DOI
10.4233/uuid:74137676-c3a5-41f2-9a47-8011de7d32c4

Publication date
2023

Document Version
Final published version

Citation (APA)
Poinelli, M. (2023). *Ocean Dynamics and Ice Fractures: Insights from Earth and Beyond*. [Dissertation (TU Delft), Delft University of Technology]. https://doi.org/10.4233/uuid:74137676-c3a5-41f2-9a47-8011de7d32c4

Important note
To cite this publication, please use the final published version (if applicable).
Please check the document version above.

Ocean Dynamics and Ice Fractures

Insights from Earth and Beyond

Mattia Poinelli

Ocean Dynamics and Ice Fractures

Insights from Earth and Beyond

Dissertation

for the purpose of obtaining the degree of doctor
at Delft University of Technology,
by the authority of the Rector Magnificus prof. dr. ir. T.H.J.J. van der
Hagen;
Chair of the Board of Doctorates,
to be defended publicly on
Monday 20 November at 17:30 o'clock

by

Mattia Poinelli

Master of Science in Aerospace Engineering,
Delft University of Technology, Delft, the Netherlands
born in Verona, Italy.

This dissertation has been approved by the promotors.

Composition of the doctoral committee:

Rector Magnificus,   chairperson
Dr. R. E. M. Riva   Delft University of Technology, promotor
Dr. M. Vizcaino   Delft University of Technology, co-promotor

Independent members:

Prof. dr. H. Seroussi   Dartmouth College, USA
Prof. dr. R. S. W. van de Wal   Utrecth University, Netherlands
Prof. dr. A. Jenkins   Northumbria University, UK
Prof. dr. C. A. Katsman   Delft University of Technology
Prof. dr. L. L. Vermeersen   Delft University of Technology (reserve)

Other members:

Dr. E. Larour   Jet Propulsion Laboratory, California Institute of
                   Technology, USA

Dr. E. Larour has significantly contributed to the realization of the content
of this thesis and acted as daily supervisor.

Ai miei nonni:
Arcangelo, Michele, Serafina, Lina

Acknowledgements

> ...California - wild, sweaty, important - the land of lonely and exiled and eccentric lovers come to forgather like birds, and the land where everybody somehow looked like broken-down, handsome, decadent movie actors.
>
> Jack Kerouak, On the Road

I am convinced that the acknowledgment section is always the most important part of any dissertation. This document is the result of more than 4 years of work spent between California, the Netherlands, and Italy. This PhD has been a roller coaster, and there are plenty of people who helped me navigate through the ups and downs. First of all, I deeply thank Eric Larour, my supervisor/mentor/guide/problem-solver at JPL, who has always believed in me, even at times when I was the first one starting to give up. You have helped me navigate through extremely difficult times during these past years. I have always been sure that you would find a solution for any problem we may have had, and so it has been, even though the problems we had were not easy ones.

Secondly, I want to thank my promotors, Riccardo and Miren, for letting me join the department of Geoscience and Remote Sensing and for giving me such freedom to choose the topic and tools for my PhD work. I have always enjoyed my visits to Delft in person, which were extremely important for a change in perspective and a literal breath of fresh air. Sometimes, it is all we need. I also want to thank my defense committee members: Helene, Adrian, Roderik, Caroline, and Bert for the time spent reading my dissertation and for your thoughtful feedback and comments.

I am sincerely thankful to Mathieu Morlighem and Eric Rignot for the support and openness during my transition to UCI, right in the middle of COVID. You hosted me without questions (at least directed to me) and welcomed me from the first day as if I were a member of your group. I want to thank the Sea Level And Ice group at JPL: Josh, Nicole, Dan, Lambert and Surendra, who have helped me grow as a researcher and a scientist. I also thank the ESS department at UCI: Enrico, Bernd, and all of Eric's, Mathieu's, and Isabella's PhD students and postdocs who provided a dynamic, rich, and fun academic environment, which was partially what I missed during my days at JPL. A heartfelt and profound thanks goes to Yoshihiro Nakayama. You probably don't know how much you helped. Chapter 3 wouldn't be here without you, and I can safely say you saved my PhD. Thank you.

I couldn't have done all of this without so many people in my personal life. Thank you to my surf crew: Al, Chris, Kristina, Nick, Giacomo, Ilaria, Brett. The ocean has been my meditation and my safe place during these years, and you all helped me in and out of the water. Surfing up and down the California coast has been a guilty pleasure, from angry Topanga all the way down to what you all know very well has been my to-go spot. Thanks to Michela and Gloria for the senzapersonalità support across three different continents (a record so far). Thanks to my friends in the Netherlands: Giulia, Zeynep, Coolio, Fabio (yes, Fabio, you are still in the Netherlands) and Arun for always making me feel at home when I was visiting from the US. You made my 'work' trips to the Netherlands feel like a treat. As always, I want to thank my old friends in Italy: Nico, Luca, my Yelton-AmmazzaCaffe' and PoliMi friends. Coming back to Italy always feels like home thanks to you.

Voglio ringraziare i miei genitori Mariella e Adriano, mio fratello Andrea, che mi sono sempre stati vicini. Grazie alla mia grande famiglia e a Sara, Raffaella e Tiziana per accompagnarmi fino in fondo a questa avventura.

Last but by far not the least, thank you, Holly. I still can't believe how immensely supportive you have been. You were so kind and loving during all these years while I was constantly busy, crunching numbers on my laptop. I can't be thankful enough. Thank you for patiently holding my hand during the thick and hard times, nonostante tutto. Grazie. I would have not made it without you. And you also became a mélange expert in the process. Oh yeah, thank you Luna, for your emotional support and for being a great study buddy (most of the times).

Mattia
Los Angeles, California
October 2023

Contents

Summary

Ice, a pervasive element across the Solar System, holds immense importance in understanding the response of the Earth to ongoing climate change as well as the dynamics of planetary bodies. This dissertation investigates ice fractures on terrestrial and planetary ice bodies, focusing on their impact on the melting of ice shelves in Antarctica and their dynamics on Europa, one of Jupiter's moons.

The urgency to understand the behavior of terrestrial ice shelves under environmental forcing is driven by the ongoing climate crisis. Antarctica is experiencing a rapid loss of mass, primarily due to increasing ocean-induced melting at the base of its ice shelves in response to global warming. The release of glacier meltwater into the world's oceans contributes to arising the global sea level. However, the rate and magnitude of sea-level rise are highly uncertain and the potential ice mass-loss from Antarctica could significantly accelerate sea-level rise throughout this century due to the instability of its ice shelves. Thus, accurately projecting Antarctica's contribution to global sea level necessitates a better understanding of the processes behind the loss of its ice shelves.

In this dissertation, I examine the thinning of Antarctic ice shelves caused by enhanced melting at their base due to warming oceans. Intrusion of ocean heat beneath the ice shelves indeed plays a crucial role in projecting their future. Through idealized ocean modeling using the Massachussetts Institute of Technology general circulation model (MITgcm), I simulate ocean dynamics under the ice, investigating the impact of fractures and ice front retreat on the sub-shelf ocean circulation. Results indicate that fractures may act as barriers, inhibiting the intrusion of warm water towards the inland sections of the ice shelves, and thereby reducing basal melt. Furthermore, I examine the impact of the separation of iceberg A-68 from the Larsen C ice shelf in July 2017 on the sub-shelf ocean dynamics. This specific retreat event leads to the redistribution of heat under the ice, resulting in enhanced melting in specific sections of the ice shelf, suggesting future destabilisation of Larsen C. These findings highlight the importance of considering updated ice-shelf coastlines to accurately project ocean circulation and its implications for ice shelf stability.

Furthermore, this dissertation explores the dynamics of specific lineament features observed on the surface of Europa, which are identified as ice fractures. Although limited observations restrict our understanding of ice fracturing events on this moon, insights from studying terrestrial ice sheets provide valuable knowledge. By extending an existing terrestrial-based numerical model of fracture propagation on ice shelves, I show that some lineaments on the surface of Europa exhibit a behavior that is similar to ice fractures on Antarctic ice shelves. The model depicts

the evolution of these lineament features as bursts of fracture propagation events interspersed with periods of inactivity, which is a typical behavior of fractures on terrestrial ice shelves.

Overall, this dissertation shows the potential for synergy between Earth and planetary science. By leveraging advances in our understanding of physical processes on Earth, terrestrial-based models and theories contribute to expanding our knowledge of physics on other celestial bodies. This interdisciplinary approach, supported and validated by remote sensing and *in-situ* missions, is fundamental in order to advance our understanding of ice fractures, their interaction with the surrounding environment and their dynamics throughout the Solar System. On Earth, a better understanding of the dynamics of Antarctic ice shelves is imperative to correctly project Antarctica's contribution to global sea level.

Samenvatting

IJs, een alomtegenwoordig element in het zonnestelsel, is van enorm belang voor het begrijpen van de reactie van de aarde op de voortdurende klimaatverandering en de dynamiek van planetaire lichamen. Dit proefschrift onderzoekt ijsbreuken op terrestrische en planetaire ijslichamen, en met name hun impact op het smelten van ijsplaten in Antarctica en hun dynamiek op Europa, een van de manen van Jupiter.

De urgentie om het gedrag van terrestrische ijsplaten onder invloed van omgevingsfactoren te begrijpen, wordt gedreven door de huidige klimaatcrisis. Antarctica ervaart een snelverlies van massa, voornamelijk als gevolg van het door de oceaan veroorzaakte toenemende smelten van ijs aan de voet van de ijsplaten als reactie op de opwarming van de aarde. Het vrijkomen van smeltwater van gletsjers in de oceanen draagt bij aan de stijging van de wereldwijde zeespiegel. De snelheid en omvang van de zeespiegelstijging zijn echter zeer onzeker en het potentiële verlies van ijsmassa van Antarctica zou, vanwege de instabiliteit van de ijsplaten, de zeespiegelstijging gedurende deze eeuw aanzienlijk kunnen versnellen. Om de bijdrage van Antarctica aan de wereldwijde zeespiegel nauwkeurig te voorspellen, is een beter begrip nodig van de processen achter het krimpen an zijn ijsplaten.

In deze dissertatie onderzoek ik het dunner worden van Antarctische ijsplaten veroorzaakt door het versnelde melten aan hun voet/onderkant als gevolg van de opwarmende oceanen. Het binnendringen van oceaanwarmte onder de ijsplaten speelt inderdaad een cruciale rol bij het voorspellen van hun toekomst. Door middel van geïdealiseerde oceaanmodellering met behulp van het Massachussetts Institute of Technology algemene circulatiemodel (MITgcm), simuleer ik de oceaandynamiek onder het ijs, en onderzoek ik de impact van breuken en terugtrekking van het ijsfront op de oceaancirculatie onder ijsplaat. De resultaten geven aan dat breuken kunnen fungeren als barrières, waardoor het binnendringen van warm water naar de landinwaarts gelegen delen van de ijsplaten wordt geremd, en daardoor de basale smelting wordt verminderd. Verder onderzoek ik de impact van de afsplitsing van ijsberg A-68 van de Larsen C-ijsplaat in juli 2017 op de sub-shelf oceaandynamiek. Deze specifieke terugtrekking leidt tot de herverdeling van warmte onder het ijs, wat resulteert een versnelde smelting in specifieke delen van de ijsplaat, wat duidt op toekomstige destabilisatie van Larsen C. Deze bevindingen benadrukken het belang van het bijwerken om de oceaancirculatie en de implicaties ervan voor de stabiliteit van de ijsplaat nauwkeurig te voorspellen.

Verder onderzoekt dit proefschrift de dynamiek van specifieke lijnen die op het oppervlak van de maan Europa worden waargenomen en die worden geïdentificeerd als ijsbreuken. Hoewel beperkte waarnemingen ons begrip van ijs-fractuur gebeurte-

nissen op deze maan beperken, bieden inzichten uit het bestuderen van terrestrische ijskappen waardevolle informatie. Door een bestaand op de terrestrische situatie gebaseerd numeriek model van breukvorming/breuk vermeerdering? op ijsplaten uit te breiden, laat ik zien dat sommige elementen op het oppervlak van Europa een gedrag vertonen dat vergelijkbaar is met ijsbreuken op Antarctische ijsplaten. Het model geeft de evolutie van deze lineament-kenmerken weer als korte uitbarstingen van breukvoortplantingsgebeurtenissen afgewisseld met perioden van inactiviteit, wat een typisch gedrag is van breuken op terrestrische ijsplaten.

'Samenvattend toont dit proefschrift het potentieel voor synergie tussen aardse- en planetaire wetenschap. Door gebruik te maken van de vooruitgang in ons begrip van fysieke processen op aarde, dragen terrestrische modellen en theorieën bij aan het uitbreiden van onze kennis van de natuurkunde over andere hemellichamen. Deze interdisciplinaire aanpak, ondersteund en gevalideerd door remote sensing en in-situ-missies, is van fundamenteel belang om ons begrip van ijsbreuken, hun interactie met de omgeving en hun dynamiek in het hele zonnestelsel te vergroten. Op aarde is een beter begrip van de dynamiek van Antarctische ijsplaten absoluut noodzakelijk om de bijdrage van Antarctica aan het wereldwijde zeeniveau correct tevoorspellen/modelleren.

The abstract was translated in Dutch by Harm Brouwer

Sommario

Le calotte polari sono fondamentali per una corretta comprensione dei meccanismi di risposta della Terra ai cambiamenti climatici. Questa tesi si concentra sulle fratture su calotte polari e su piattaforme di ghiaccio galleggianti, sia in ambito terrestre che planetario: in Antartide e sulla crosta ghiacciata di Europa, una delle lune di Giove.

L'urgenza di comprendere le reazioni delle piattaforme di ghiaccio terrestri sotto l'azione di stimoli ambientali è guidata dalla crisi climatica in corso. Il ghiaccio marino e continentale in Antartide sta rapidamente diminuendo e la causa é da ritrovarsi principalmente nel progressivo aumento delle temperature atmosferiche e oceaniche. In particolare, l'arrivo di correnti oceaniche calde sotto le piattaforme di ghiaccio in Antartide implicano un aumento di energia termica nei punti più critici per la stabilita' della calotta glaciale. Di conseguenza, lo scioglimento dai ghiacciai che riversano direttamente nel oceano e' il fattore che più contribuisce all'aumento dei livelli marini. La velocità di innalzamento dei livelli marini e la potenziale perdita di massa di ghiaccio dall'Antartide potrebbero accelerare significativamente nel corso di questo secolo a causa dell'instabilità delle sue piattaforme. E' quindi cruciale che si migliori la precisione delle stime del contributo dell'Antartide al livello globale del mare. Questo richiede una migliore comprensione dei processi di interazione ghiaccio-oceano alla base delle sue piattaforme di ghiaccio.

Attraverso simulazioni numeriche basate sul modello di circolazione generale sviluppato all'MIT (Massachusetts Institute of Technology general circulation model, MITgcm), questa tesi si concentra sulla dinamica oceanica sotto le piattaforme di ghiaccio in Antartide. In particolare, il modello simula l'impatto delle fratture e della separazione di iceberg sulla circolazione di correnti oceaniche che trasportano calore verso il continente. I risultati presentati qui indicano che le fratture possono agire come barriere, inibendo l'intrusione di acqua calda verso le sezioni più interne delle piattaforme di ghiaccio e riducendo quindi lo scioglimento alla base. Inoltre, questa tesi esamina l'impatto della separazione dell'iceberg A-68 dalla piattaforma di ghiaccio Larsen C nel luglio 2017 sulla dinamica delle correnti oceaniche vicino alla costa. Questo specifico evento porta ad una sostanziale redistribuzione del calore sotto il ghiaccio, con un conseguente aumento dello scioglimento in specifiche sezioni, suggerendo una futura destabilizzazione della piattaforma Larsen C. I risultati presentati qui evidenziano l'importanza di una corretta mappatura delle coste adiacenti alle piattaforme di ghiaccio. Questi processi sono fondamentali per estimare con precisione la dinamica oceanica e le sue implicazioni per la stabilità dei ghiacciai in Antartide nel presente e nel futuro.

Infine, questa dissertazione esplora le dinamiche di specifiche caratteristiche

morfologiche osservate sulla superficie di Europa, una delle lune di Giove. Linea-
menti sulla superficie sono da tempo identificati come fratture sulla superficie ghiac-
ciata della luna. Estendendo un modello numerico basato sulla propagazione delle
fratture sulle piattaforme di ghiaccio in Antartide, questa tesi indica che alcune frat-
ture caratteristiche sulla superficie di Europa dimostrano un comportamento simile
a cosa accade nel ghiaccio dell'Antartide. Il modello presentato qui simula la dinam-
ica di queste fratture come eventi istantanei di propagazione, intervallati da periodi
di inattività. Questo è un comportamento tipico delle fratture sulle piattaforme di
ghiaccio terrestri.

Concludendo, questa tesi mostra come una sinergia tra la scienza della Terra e
quella planetaria possa migliorare la nostra comprensione dei fenomeni naturali che
governano le calotte polari. Sfruttando lo studio dei processi fisici sulla Terra, mod-
elli e teorie basate sulla fisica terrestra possono migliorare la nostra comprensione
della fisica di altri corpi celesti. Questo approccio interdisciplinare, che deve neces-
sariamente essere supportato e validato da missioni di osservazione e rilevamento
remoto e locale, è fondamentale per avanzare nella comprensione delle fratture del
ghiaccio, della loro interazione con l'ambiente circostante e delle loro dinamiche in
tutto il Sistema Solare. In particolare, una migliorata comprensione delle dinamiche
delle piattaforme di ghiaccio dell'Antartide è fondamentale per una corretta stima
del contributo dello scioglimento dei ghiacci in Antartide ai livelli marini globali.

Chapter 1

Introduction

> We are at a fork in the road for where we
> stand as a species.
>
> ———————————————————————
> Al Gore

1.1 Preface

Ice is a common element throughout our Solar System, ranging from glaciers on Earth to icy comets orbiting the Sun, Martian ice deposits, rings and ice-covered moons around distant giant planets. Ice cracks, in particular, are a familiar occurrence in our daily interactions with frozen water. The topic of this dissertation spans across fracture on ice on both terrestrial and planetary ice bodies. More specifically, I focus my attention on ice fractures and their significant implications for the dynamics of Earth's ice sheets and icy moons in our Solar System. Despite their importance, understanding the origin and behavior of ice fractures at regional and planetary scales remains challenging.

The urgency to better understand how terrestrial ice sheets behave and respond to environmental forcing is driven by the ongoing climate warming crisis. Ice sheets are formed from layers of snow that accumulate over thousands of years and compress into thick ice. Ice sheets contain about 99% of the Earth's freshwater, making them a crucial component of the planet dynamics. Today, there are only two ice sheets in the world: the Antarctic ice sheet and the Greenland ice sheet. As ice sheets flow toward the coastlines, they can extend over the ocean, creating what are known as ice shelves. Ice shelves play a role in regulating the flow of ice from the interior of the ice sheet to the ocean. They help slow down the discharge of ice into the ocean and act as a buttress, holding back the flow of the ice sheet. When ice shelves melt or collapse, they allow the ice from the interior to flow more rapidly into the ocean which contributes to sea-level rise.

Numerous fieldwork campaigns and remote sensing observations are becoming increasingly available, with a further need for numerical models to project the dynamics of ice sheets and ice shelves nested within the complicated Earth system. In

contrast, the dynamics of ice in the rest of the Solar System remain largely unknown due to the paucity of observations. In particular, the Jovian moon Europa is covered by an ice crust that overlays a global liquid ocean. Despite Europa having been identified as one of the most likely sites for life in the Solar System, making it one of the most interesting environments in the Solar System to further investigate, processes occurring on its surface and, specifically, the dynamics of fractures on its ice shell remain vastly unexplored. In this dissertation, I aim to improve our understanding of pathways of ocean heat delivery under Antarctic ice shelves, with a particular focus on locations where large ice fractures are a common features. Furthermore, I aim to build on an existing terrestrial-based numerical model of fracturing of Antarctic ice shelves to simulate ice lineaments observed on the surface of the Jupiter moon Europa.

This introductory chapter is divided into three parts. Firstly, Sections 1.2-1.6 discuss the importance of Antarctic ice shelves and their vulnerability in the context of global warming. A particular focus is given to ice fractures and the impact of these features on ice and ocean dynamics. Secondly, Section 1.7 briefly introduces Europa, the smallest of Jupiter's Galilean moons, which displays unique fractures on its icy surface and hosts a potentially habitable sub-surface ocean. However, the dynamics of these lineaments on this moon remain poorly understood, despite their potential for providing the only possible access to the moon's habitable interior. Lastly, Section 1.8 summarizes the knowledge gaps and introduces the research objectives of this dissertation, which will be discussed in subsequent chapters.

1.2   Climate change, sea-level rise and ice sheets

Direct observations taken on and above the surface of the Earth indicate that the planet's climate is significantly warming (e.g. Brohan et al., 2006; Hartmann et al., 2013; Rahmstorf et al., 2017). Since the mid 19th century, the average temperature on the Earth's surface has progressively increased. Most of this rise occurred in the past 40 years, while global surface temperature in the first two decades of the 21st century alone was around 1°C higher than the average 1850-1900 (e.g. Morice et al., 2012). Years 2016 and 2020 broke the record as warmest years since the beginning of modern instrumental record (NOAA, 2021). Causes of such dramatic changes are unequivocally attributed to human-related activity; 97% of publishing climate scientists agrees that human activity and emission of greenhouse gases are the key causes of global warming, based on the consensus of 11944 research papers from 1991 to 2011 (Cook et al., 2013, 2016). Unfortunately, there is also high confidence that global temperatures will continue to rise, with critical consequences in the climate and in the daily life of millions of people (McGranahan et al., 2007; Kopp et al., 2014). The Intergovernmental Panel on Climate Change (IPCC) is the international body for assessing the science related to climate change and it periodically releases comprehensive reports regarding the state of knowledge on topics related to climate change.

Ongoing climate warming is causing the global sea level to rise at an accelerated

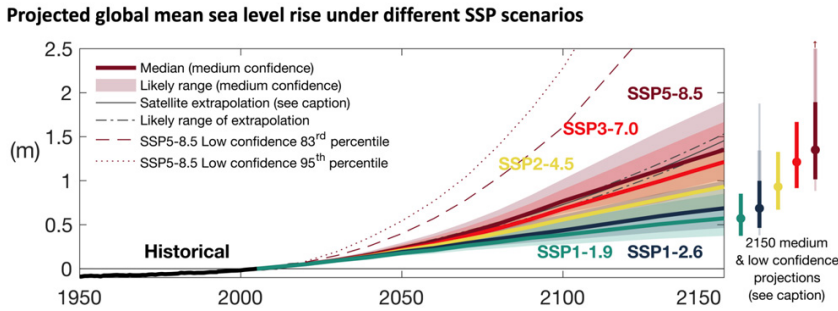**Projected global mean sea level rise under different SSP scenarios**

Figure 1.1: Global mean sea level change from 1900 to 2150, observed (1900 - 2018) and projected under the Shared Socio-economic Pathways (SSP) scenarios (2000 - 2150), relative to a 1995 - 2014 baseline, after the Sixth Assessment Report (AR6) by the IPCC (Masson-Delmotte et al., 2021). The report distinguishes between "very low" emissions scenario (SSP1-1.9), "low" (SSP1-2.6) and "intermediate" (SSP2-4.5), through to "high" (SSP3-7.0) and "very high" (SSP5-8.5). The bold lines indicate the median projection of models that include only medium-confidence processes, while the shading represents the "likely" range of those same models. The bars to the right show the median and likely ranges of projections for models that include both medium- and low-confidence processes such as the instability of Antarctic ice shelves.

pace. Projections also indicate that this trend will continue in the future, putting communities living in low-lying coastal areas at risk (e.g. Nicholls and Cazenave, 2010). From 1900 to 2018, global sea level has already risen by approximately 20 cm (Gregory et al., 2013; Hay et al., 2015; Frederikse et al., 2020). The Sixth Assessment Report (AR6) by the IPCC (Masson-Delmotte et al., 2021) quantifies how future emissions will determine global warming and sea level rise scenarios (Figure 1.1). These scenarios range from high CO_2 emissions without climate change mitigation to a low CO_2 emissions scenario achieving net zero CO_2 emissions. In the lowest emission scenario, global temperature increase will be limited to below 1.5^oC, with global sea level rise confined to a maximum of 55 cm relative to the 1995-2014 average. Conversely, the most extreme emission scenario may result in a temperature increase of up to 5.7^oC and a global sea level rise of as much as 1 meter.

Global warming contributes to sea level rise through two main mechanisms: thermal expansion and the melting of glaciers and ice sheets worldwide. Since the early 1990s, land ice mass loss has become the largest contributor to sea level rise, surpassing thermal expansion (Frederikse et al., 2020). Therefore, understanding the mechanisms of freshwater discharge from the world's ice reservoirs is crucial for improving our predictions of future sea level change.

The two largest reservoirs of glacial freshwater on Earth are the Greenland Ice Sheet in the northern hemisphere and the Antarctic Ice Sheet in the southern hemisphere. Although Greenland is losing ice at a relatively higher pace, approximately 270 Gt per year, compared to Antarctica's average ice loss of around 150 Gt per year (Kjeldsen et al., 2015; Sasgen et al., 2020; Otosaka et al., 2023), Antarctica

still represents the largest mass of ice on Earth. If the entire ice sheet were to melt and discharge as freshwater into the global ocean, it would contribute approximately 58 m to sea level rise, whereas Greenland would contribute 7.4 meters (Morlighem et al., 2014, 2020). While projections of future Greenland ice mass loss are primarily driven by increased surface melt under all emissions scenarios (Goelzer et al., 2020; Hofer et al., 2020), significant uncertainty remains regarding the evolution and contribution of the Antarctic Ice Sheet. This uncertainty is primarily related to the potential abrupt and widespread onset of instability in its ice shelves (DeConto and Pollard, 2016). To better understand and predict future sea level rise, it is imperative to investigate the dynamics of ice shelves in the Southern Hemisphere and the mechanisms by which Antarctica is losing mass.

The contribution of the Antarctic ice sheet to sea level rise between 1979 and 2017 is estimated to be approximately 3.60 mm per decade, resulting in a total sea level contribution of 14 mm (Rignot et al., 2019). From 2009 to 2017, about 63% of the total loss comes from a relatively small area in Western Antarctica, which includes the fast melting of ice shelves such as Thwaites and Pine Island (e.g. Graham et al., 2022). However, there are several large glaciers around Antarctica that are currently stable but may begin to accelerate their release of freshwater into the global ocean as global warming worsens. One of the key factors that will determine this acceleration is the evolution of the downstream ice shelves. In the next section, I will delve into the importance of ice shelves in maintaining the stability of the Antarctic Ice Sheet.

1.3   The Antarctic ice sheet and the importance of ice shelves

The Antarctic Ice sheet covers an area of almost 14 million square kilometers (1.6 times the size of the United States) and contains 26.5 million cubic kilometers of ice, which is approximately 90% of the total ice and 70% of the total freshwater on Earth (e.g. Fretwell et al., 2013). Almost all precipitation in Antarctica is in the form of snow which accumulates as ice, after snow consolidates (van Wessem et al., 2018). However, ice does not accumulate indefinitely since high-altitude land ice flows through glaciers toward lower altitudes around the entire perimeter of the continent, due to gravity (Cuffey and Paterson, 2006). Eventually grounded ice reaches the coastline and starts floating on the ocean surface, forming tabular extensions of continental ice: the so-called ice shelves. The location at which grounded ice becomes afloat and separates from the continent is termed grounding line.

Ice shelves exert a buttressing force on the land ice and restrain the upstream continental ice from sliding and discharging into the ocean (Dupont and Alley, 2005; Scambos et al., 2004). As a consequence, ice shelf ablation causes the upstream glaciers to accelerate their flow toward the coastline and the consequent freshwater discharge into the ocean (Rott et al., 2002; Rignot et al., 2004), which adds to the global sea level. As ice shelves are in contact with atmosphere and ocean - both of which are warming up - they are highly vulnerable to global warming (Obase
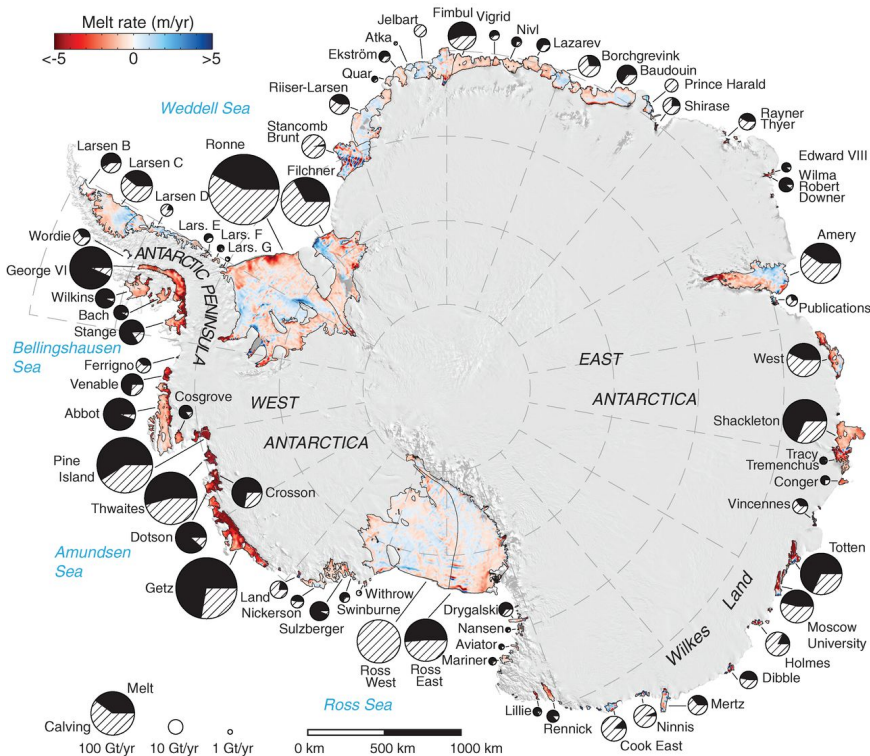
Figure 1.2: Total basal melt of ice shelves around the Antarctic continent. Ice-shelf perimeters in 2007 and 2008, excluding ice rises and ice islands, are thin black lines. Color-code ranges between freezing (blue) to melting (red) and is overlaid on a 2009 mosaic of Antarctica. Each circle graph is proportional in area to the mass loss from each shelf, in Gt/year, partitioned between iceberg calving (hatch fill) and basal melting (black fill). Figure and caption are adapted from Rignot et al. (2013).

et al., 2017) and represent the dominant mechanism by which the Antarctic ice sheet loses mass. It is important to notice that ice shelf ablation does not contribute to sea level rise per se, as these tabular extensions of grounded ice are already afloat. Their presence is therefore already accounted in the global sea level. However, the commitment to sea level occurs when ice flows faster and thins, in response to the weakening of the buttressing force generated by ice shelves.

There are two main mechanisms by which ice shelves lose mass: basal melt and iceberg calving (Figure 1.2). Calving refers to the release of icebergs which are separated ("calved") from the ice shelves after ice fractures evolve and propagate. This process leads to ice front retreat. However, given the complexity of fracturing processes and the variability of environmental factors different for each individual ice shelf, determining universal calving laws is extremely challenging (a review of calving laws is in Emetc et al., 2018). Icebergs are formed after ice fractures eventually separate tabular portions of floating ice into the open ocean. Fractures on the ice shelves are mainly distinguished between ice rifts - if the crack propagates through

the entire shelf thickness (namely creating an interface between ocean and atmosphere) - or ice crevasses, when the crack initiates either on the surface or at the bottom but its tip is confined within the ice layer. Rifting naturally occurs on Antarctic ice due to various environmental and glaciological factors (Walker and Gardner, 2019; Walker et al., 2015), and is often originated along lateral boundaries of outlet streams feeding the ice shelf (Hulbe et al., 2010). Rifts often propagate in a direction transverse to the ice flow. Iceberg calving represents the second largest ablation process of Antarctic ice shelves, with an estimate of 45% of the total ice mass loss (Rignot et al., 2013).

The largest contributor to contemporary ice shelf loss is ocean-induced basal melting, which contributes roughly 55% of the total ablation of Antarctic ice shelves (Pritchard et al., 2012; Rignot et al., 2013). Ice shelves are flushed by the Southern ocean, which is increasingly accounting for a disproportionate heat gain in response to climate warming of recent decades (Schmidtko et al., 2014). In particular, the Southern ocean was estimated to have accumulated an average of up to 62% of the total global ocean heat excess estimated over the period between 2005 and 2017) (Poertner et al., 2019, Ch. 3). The interactions between ocean water and Ice shelves are complicated and largely depend on the effective pathways of ocean heat that bring warm water from lower latitudes close to the Antarctic continent.

In particular, basal melt is often the highest where the ice shelf is the deepest, namely near the grounding line where the floating ice has just lost contact with the underlying bedrock. Observations show that increased melting near the grounding line - especially when warm water has direct access to that region (e.g. Nakayama et al., 2018, 2019) - causes the grounding line to migrate landward (Rignot and Jacobs, 2002; Bamber et al., 2009). Where that happens on a reverse bed slope it results in the glacier becoming grounded in deeper water with a greater ice thickness. Ice thickness at the grounding line is a key factor in controlling flux across the grounding line (Joughin and Alley, 2011), so thicker ice grounded in deeper water would result in increased discharge, floatation, basal melting, increased iceberg production, and further retreat within a positive feedback loop. These processes are known to further accelerate freshwater discharge from outlet glaciers into the ocean (Thomas et al., 2004).

Despite the discussed importance of ocean-induced melting in order to accurately quantify the total ice loss of the Antarctic ice sheet, mechanisms of ice shelf ablation remain uncertain for the most part. In particular, a better understanding of the interaction between ice and ocean as well as how rifting leads to ice front retreat is imperative to accurately project the future of the Antarctic Ice Sheet and, in turn, its future commitment to sea level rise. *The main goal of this dissertation is to explain the impact of large rifts and ice front retreat on pathways of ocean forcing under the ice shelf*. In the following sections, I review the current understanding of ocean dynamics around the Antarctic continent, with a focus on the mutual interactions between ice shelves and the ocean.
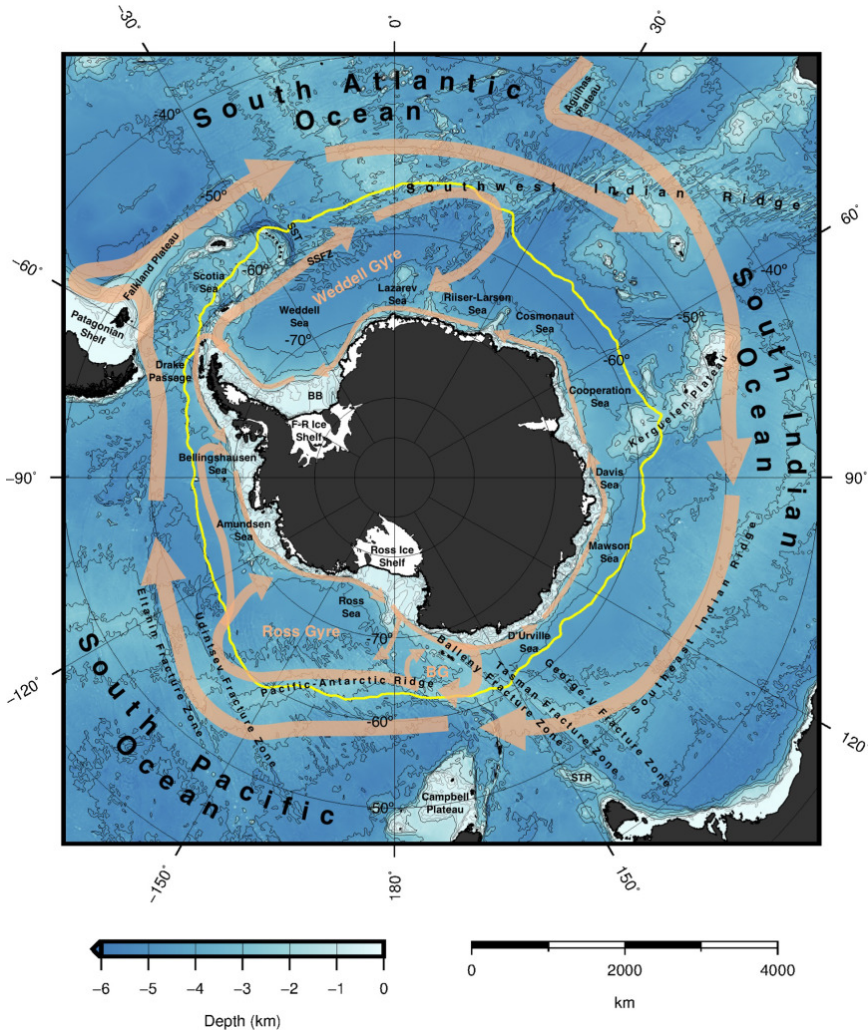
Figure 1.3: Bathymetric map of the Southern ocean, adjacent oceans, and marginal seas. The floating ice shelves of the Antarctic ice sheets are shown in white bounded by thick black lines, while grounded ice (and other land areas) is shown in dark gray. Circulation features are shown in orange, including the Antarctic Circumpolar Current (ACC, the thickest orange arrows), the Antarctic Slope Current (ASC), and the Ross, Weddell, and Balleny Gyres (BG). Yellow line is the mean 15% sea ice concentration in September. Abbreviations used on the map are SST, South Sandwich Trench; SSFZ, South Sandwich Fracture Zone; STR, South Tasman Rise; F-R Ice Shelf, Filchner-Ronne Ice Shelf; and BB, Berkner Bank. Figure and caption are from Armitage et al. (2018)

1.4 Ocean circulation around Antarctica

The Antarctic ice sheet and its ice shelves are flushed by the Southern ocean along its entire perimeter (Figure 1.3, 1.4). The Southern ocean is the only ocean on Earth
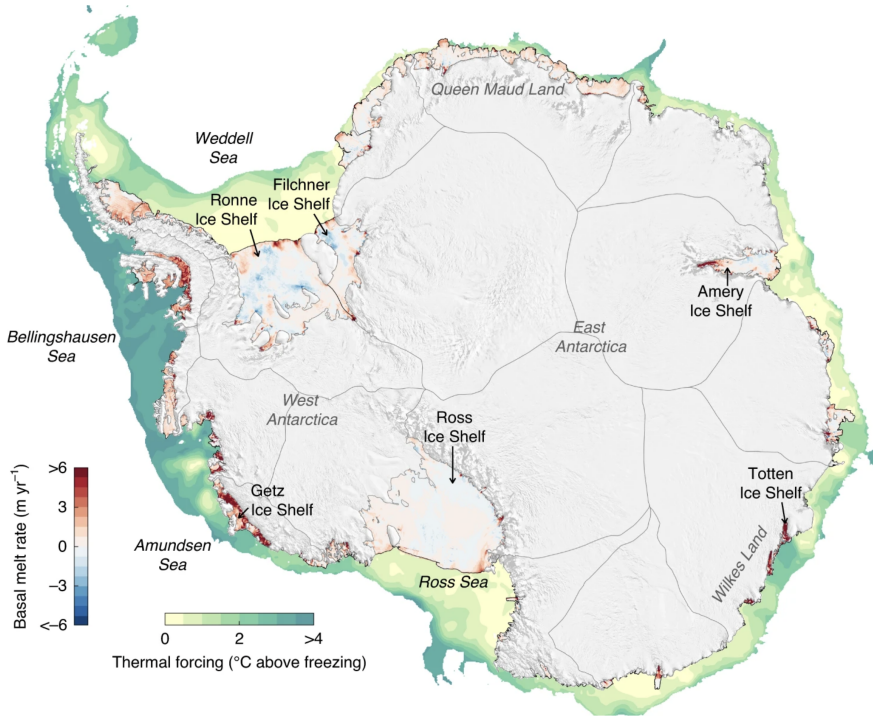
Figure 1.4: Basal melt are averaged over the time period between 2010 and 2018. The units are m of ice equivalent per year, assuming an ice density of 917 kg m^{-3}. The thermal forcing, defined as the temperature above the in situ freezing point of seawater, is mapped for water depths above 1500 m. For water depths less than 200 m, the seafloor thermal forcing is shown, and for water depths below 200 m, the maximum thermal forcing between 200 and 800 m is shown. Figure and caption are from Adusumilli et al. (2020).

that is not surrounded by continental land masses. This establishes a "water band" that extends around the entire Antarctic perimeter, connecting Indian, Atlantic and Pacific ocean basins with pivotal implication in the transport and mixing of nutrients, marine life and water masses. A clock-wise (as seen from the South Pole) flow is established from west to east as water flows around Antarctica without encountering any north-south land barrier (Tomczak and Godfrey, 1994). This eastward current is termed Antarctic Circumpolar Current and represents the strongest current on Earth, with a mean transport of 134 Sv (1 Sv = 10^6 m^3/s) (e.g. Donohue et al., 2016). The Antarctic Circumpolar Current is driven by strong westerly winds that flow around the continent in combination with sharp density gradients in the ocean. These occur between warmer subtropical/temperate zones and the colder polar zones (Rintoul, 2009).

The density gradient in the transition between warm and light waters that dominate the subtropical/temperate zones and cold and denser waters that are found near Antarctica leads isopycnals (levels of constant ocean density) to slope up to-

ward the Antarctic continent. Westerly winds enhance this effect and the Antarctic Circumpolar current flows along it, accelerating when the slope is steeper (Tomczak and Godfrey, 1994). As a consequence, this current separates the two temperature regimes and maintains the Antarctic continent largely isolated from heat accumulated at lower latitudes. Climate change is impacting the Antarctic Circumpolar current in major ways. Surprisingly, the ongoing warming of the Southern ocean (Schmidtko et al., 2014) and the intensification of westerly winds (Lin et al., 2018) has not been correlated to strengthening of this pan-Antarctic current (Böning et al., 2008). On the other hand, these processes were found to be responsible for enhancing eddy-induced heat transport toward the Antarctic continent (Hogg et al., 2015) and to lead the southern boundary of the Antarctic Circumpolar current to migrate poleward (Yamazaki et al., 2021). As a consequence, progressively more heat reaches Antarctic ice shelves in response to global warming.

The Antarctic Circumpolar current leads to the formation of two large gyres as the eastward flow encounters two indentations along the Antarctic continent: one immediately east of the Antarctic Peninsula in the Weddell sea and one adjacent to the Ross sea. These two indentation in the Antarctic coastline form the Weddell and Ross gyre as water flowing toward the east deviates south and returns westward along the Antarctic coastline. This motion along the coast feeds the Antarctic Slope current, which flows westward in a near-circumpolar, anticyclonic fashion along the Antarctic continent slope (Thompson et al., 2018). These two large cyclonic (i.e. rotating clock-wise) gyres are extremely important in mixing processes between deep and surface waters as well as gases exchanges between atmosphere and ocean (Tomczak and Godfrey, 1994).

1.5   Ice shelf-ocean interactions

The hydrography and the various ocean masses on the Antarctic continental shelf and the interaction with Antarctic ice shelves[1] are revealed by looking at meridional cross sections of the ocean basins around the continent (Figure 1.5). The deepest and densest water mass in the Southern ocean is the Antarctic Bottom Water (AABW), which sits below 4000 m. Above AABW in the Antarctic Circumpolar current lays the Circumpolar Deep Water (CDW). This water is also the warmest water mass around Antarctica, with a characteristic temperature of around 1^oC (Tomczak and Godfrey, 1994). CDW lays just below 500 m - roughly at the depth of the Antarctic continental shelf - and has therefore the potential to spill onto the continental shelf, and to reach the continent and its ice shelves. As the temperature of CDW can be 4^oC higher than the in-situ freezing point of seawater, direct contact between ice shelves and CDW necessarily leads to basal melting. Depending on whether CDW has direct access to the ice shelves or not, conditions in the Antarctic ocean can be roughly divided into two thermal regimes (e.g. Petty et al., 2013; Dinniman et al., 2016): "warm water"

---

[1]It is important to note that there is a difference between an ice shelf and a continental shelf. The former are the extension of land ice into the ocean, while the latter is a portion of a continent that is submerged under an area of relatively shallow water.

and "cold water", which are dominated by completely different ice-ocean processes (Figure 1.4).

Concerning the "cold water" regime, examples are in the Weddell and Ross seas. These locations are dominated by abundant sea ice production, where cold winter temperatures remove heat and bring surface water to freezing. This process is very efficient in coastal polynyas, semi-permanent areas of open ocean where strong katabatic winds clear the ocean surface from existing sea ice and favours further freezing of the ocean surface. In turn, winter sea ice production leads to brine rejection and salinification of surface water, which is often labeled as Winter Water (WW). The mix of these dense and cold water masses - at the freezing point of seawater, i.e. approximately -1.9^{o}C - is often termed High Salinity Shelf Water (HSSW) and tends to sink due to decreased buoyancy after water salinification (Nicholls et al., 2009). As a result, the Weddell and Ross seas are dominated by cold and saline water (Orsi and Whitworth, 2005), with limited interaction with CDW, and ice shelves in these areas are often referred to as "cold water ice shelves".

The interaction between CDW and the various colder water masses near the Antarctic continent redistributes the heat in proximity of the ice front. For example, the Weddell and Ross gyres isolate the Antarctic coastline and the nearby basin from relatively warmer conditions of the Antarctic Circumpolar current and in particular from CDW, its dominant and warmest component (Jenkins et al., 2016). As a consequence, ice shelves in the Weddell and Ross seas are substantially shielded from direct (or modified) CDW intrusion. However, dense and hypersaline HSSW can also intrude under the ice base (Nicholls et al., 2009) and reach into deep sections of the ice cavity (defined as the portion of water below the ice shelf). Despite being sourced at the surface freezing temperature (-1.9^{o}C), HSSW has the potential to melt the ice bottom because the freezing point of seawater decreases with depth. This type of ice base melting is often referred to as Mode 1, based on the classification introduced by Jacobs et al. (1992). As a consequence, cold water ice shelves in the Weddell and Ross seas melt at a relatively slow pace ($\sim$0.1-1 m/yr) and can therefore extend seaward for hundreds of kilometers.

Concerning the "warm water" regime, examples are in the Amundsen and Bellinghausen seas. Ice shelves in these locations experience a direct flooding from warm CDW which directly spills onto the continental shelf. In these areas, surface production of cold and dense water is weaker than in the Ross and Weddell sea and, as a consequence, the protection provided by down-welling of surface water is substantially absent (Jenkins et al., 2016). Warm CDW follows the topography of the ocean bottom (bathymetry) and is therefore driven toward the grounding line (e.g. Nakayama et al., 2018, 2019), and drives high melting in these deep locations. Warm water ice shelves are currently melting at a relatively fast pace ($\sim$10-100 m/yr) and are therefore generally much smaller than those in the Ross and Weddell seas. This type of ice base melting - where CDW has direct access to the ice shelf cavity - is often referred to as Mode 2.

Basal melting of small warm water ice shelves after Mode 2 represents by far the largest contributor to ice mass loss in Antarctica (Paolo et al., 2015; Adusumilli
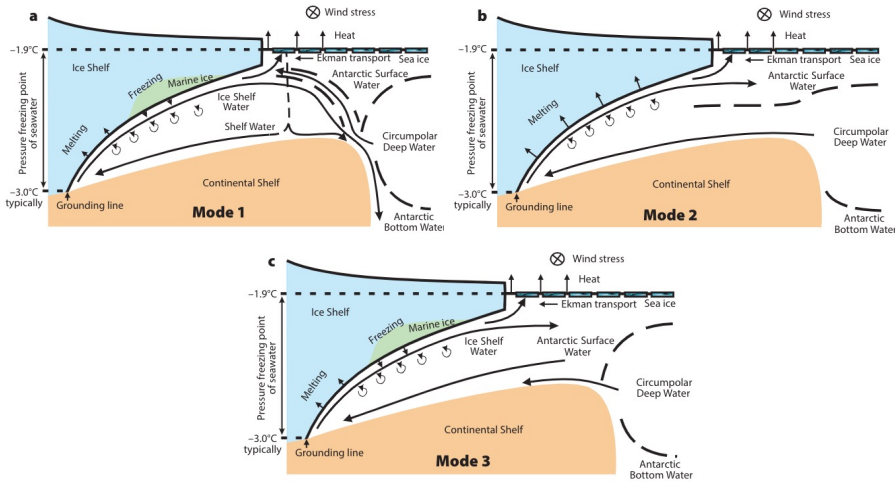
Figure 1.5: Three modes of sub-ice-shelf circulation and associated stratification on the continental shelf. (a) In Mode 1, dense Shelf Water, formed by brine rejection beneath growing sea ice, dominates the sub-ice cavity and drives (slow) melting. (b) Mode 2 dominates if Shelf Water is absent and Circumpolar Deep Water spills onto the continental shelf and is drives fast melting and rapid grounding line retreat. (c) Mode 3 dominates where both Shelf Water and Circumpolar Deep Water are absent, leaving Antarctic Surface Water as the densest water on the shelf. Figure and caption are after Jacobs et al. (1992) and Jenkins et al. (2016).

et al., 2020). In particular, the largest melt signal from the Southern continent is concentrated in West Antarctica - a relatively small sector of around 2400 km spanning from George VI to Land glaciers - with a total contribution of 63% of the total loss in Antarctica (Rignot et al., 2019), and its ablation has increased by 70% in the past decade. Furthermore, the progressive southward migration of CDW is expected to get closer to cold water ice shelves near the Filchner ice shelf, with the potential for these ice shelves to transition to a warmer regime (Hattermann et al., 2021) and to a Mode 2 type of melting.

Furthermore, the classic classification of mechanisms of ice shelf ablation proposed by Jacobs et al. (1992) identifies a further melting mode, Mode 3. In this last mechanism, both CDW and HSSW are absent and the melting is generally controlled by surface water. In particular, the intrusion of relatively cold WW into the ice shelf cavity is similar to HSSW but summer atmosphere-warming of surface water can significantly enhance melting near the ice front and in ice shelves where the grounding line is sufficiently shallow. Mode 3 is observed in Ronne-Filchner and Fimbulisen ice shelves in the Weddell sea (e.g. Hattermann et al., 2012), and the Ross and McMurdo ice shelves in the Ross Sea (e.g. Arzeno et al., 2014). Despite the general theory behind ocean-induced ice shelf thinning is well described by the three melting modes of Jacobs et al. (1992), real case scenarios are much more complicated and dependent to the local hydrography and the shape of the ice shelf cavity (Schodlok et al., 2012;

Goldberg et al., 2012).

In this dissertation, I examine ice shelf-ocean interactions and the mechanisms of ocean heat intrusion under the ice shelves with a particular focus on the Antarctic Peninsula (Figure 1.6). Given its relatively low latitude, the Antarctic Peninsula is the first region of Antarctica to respond to a changing environment, as progressively warmer oceanic and atmospheric conditions arise in the polar regions. In the last few decades, most of the ice shelves in this location have either substantially retreated or completely disintegrated (Cook and Vaughan, 2010) in response to global warming, with a consequent acceleration of the freshwater discharge into the Southern ocean from upstream glaciers. In the next section, I describe the current understanding of the dynamics of ice and ocean in the eastern Antarctic peninsula, with focus on the Larsen C Ice Shelf, which will be the case study in this dissertation.

1.6 The Larsen C Ice shelf and the calving of iceberg A-68

Before the mid 90s, the northern-most ice shelves in the eastern Antarctic peninsula were the Prince Gustav and the Larsen A ice shelves. These ice shelves grew and their ice front advanced from 1902 until approximately 1975. Until 1963 these relatively large ice shelves were surrounded by wide areas of fast-ice (Skvarca, 1993). During more than 70 years, the ice shelf lost mass through quasi-periodic calving of large icebergs (Skvarca, 1994), as a natural interruption of the ice shelf advance (Cuffey and Paterson, 2006). In the mid 70s, this process was replaced by calving of small elongated icebergs following ice front retreat. In late January 1995, both the Prince Gustav and Larsen A ice shelves rapidly disintegrated over the course of just a few days (Rott et al., 1996).

Between February and March 2002, the Larsen B ice shelf, immediately south of Larsen A, experienced similar ablation processes which led to a collapse of most of its area (Scambos et al., 2003). The disintegration of these large cold ice shelves in the eastern Antarctic peninsula was likely due to progressive weakening of the ice shelf in response to penetration of atmospheric-induced meltwater during the Antarctic summer. According to this theory - often referred to as hydrofracturing - progressively warmer summers (Fahnestock et al., 2002; Torinesi et al., 2003) cause superficial melting that is sufficient to saturate the firn layer - defined as the layer of light snow at the surface - and to accumulate ponds of liquid water on the ice-shelf surface. Surface water-filled hydrofractures can then propagate toward the bottom of the ice shelf (Van der Veen, 1998b; Weertman, 1973), and their penetration can compromise the mechanical integrity and the stability of an ice shelf (Scambos et al., 2000).

Until the mid to late 80s, no melting ponds were actually observed on the surface of the various Larsen ice shelves. Melting features were firstly observed at the north of Ektoria and Evan outflows as well as on the Larsen A ice shelf in the summer season of 1988 (Scambos et al., 2003). As summer seasons lengthen from the 80s

Figure 1.6: Map of the Antarctic peninsula for year 2011. Shared relief from NASA data. Credits Giovanni Fattori, Santiago, Chile

up until the early 00s (Fahnestock et al., 2002; Torinesi et al., 2003), melting features migrated southward, initiated hydrofracturing processes and the consequent disintegration of Larsen A. Melting ponds were also observed just north of Cape Disappointment in the Larsen B ice shelf in the summer of 1999. Further melting and generalized hydrofracturing also characterized the exceptionally warm summer in 2002, when Larsen B collapsed (Van den Broeke, 2005).

Despite providing the most reasonable explanation for the collapse of Larsen A and B, the hydrofracturing framework is not sufficient to explain the early retreat of ice shelves north of Larsen C which began decades before the appearance of superficial melting ponds. Differently than hydrofracturing-induced collapse - where ice shelves progressively disintegrate after calving of small icebergs in a relatively fast timeframe - calving of large icebergs in response of rift propagation possibly compromise the ice shelf stability and preconditioned the following disintegration (Doake et al., 1998). For example, Larsen C ice shelf calved iceberg A-68 in July 2017 - the middle of the Antarctic winter - after years of propagation of a single ice rift, whilst in complete absence of melting features and hydrofractures. Although the calving event did not completely destabilize the Larsen C ice shelf (Fürst et al., 2016), it brought the ice-front into a vulnerable position. Further ice-front retreat events may lead to irreversible collapse with a potential sea level rise equivalent from the upstream glacier of up to 1500 Gt of ice in the next 300 years (Rignot et al., 2019).

The recent study of Larour et al. (2021) uses the Ice Sheet and Sea Level System Model (ISSM, Larour et al., 2012) to propose that thinning of ice under critical pinning points - in response to warm water intruding into the ice shelf cavity - may have reactivated rifting processes that eventually led to the separation of iceberg A-68. During ice-front retreat events, the temporary front location is often pinned by ice rises, rumples, islands, and shallow bathymetric features that buttress ice flow Thomas (1979). Such critical pinning points are crucial in the overall stability of the ice-shelf. On the Larsen C Ice Shelf, basal melting around pinning points such as the Gipps and Bawden Ice Rises is indeed thought to reactivate local rifts (Holland et al., 2009; Borstad et al., 2013; Kulessa et al., 2014), potentially leading to calving events such as the one in 2017. *However, pathways of ocean heat intrusion under Larsen C during and after the calving of iceberg A-68, along with the impact on basal ablation near local pinning points, remain poorly constrained.* In particular, long-term *in-situ* data are sparse as persistent sea-ice makes these locations particularly inaccessible and therefore under-sampled.

The rift that separated iceberg A-68 nucleated in the summer of 2005 near the Gibbs Ice Rise in an area that is heavily filled with accreted ice mélange (Jansen et al., 2015; McGrath et al., 2014), possibly due to large lateral shear stresses. Ice mélange is a term that was conceived by Eric Rignot and Douglas MacAyeal to identify a combination of accreted sea ice, marine ice, windblown snow and fragments of ice shelf, mixed in an heterogeneous material that is often observed in front of ice shelves and within ice rifts (Rignot and MacAyeal, 1998; MacAyeal et al., 1998). Between 2005 and 2008 the rift rupture tip advanced for around 10 km before stopping in the ice mélange-filled suture zone downstream of the Joerg peninsula. A suture zone is the location where two tributary glacier outflows merge together, this area is characterized by strong shear and is therefore warmer than meteoric ice flow units (directly downstream of outlet glaciers). These areas often coincide with crack arrest (Hulbe et al., 2010). Indeed, ice heterogeneity (ice mélange-filled suture zones vs meteoric ice) is thought to be one of the main factors controlling rift propagation (Borstad et al., 2017). As a matter of fact, rift A-68 took almost 8 years to propagate
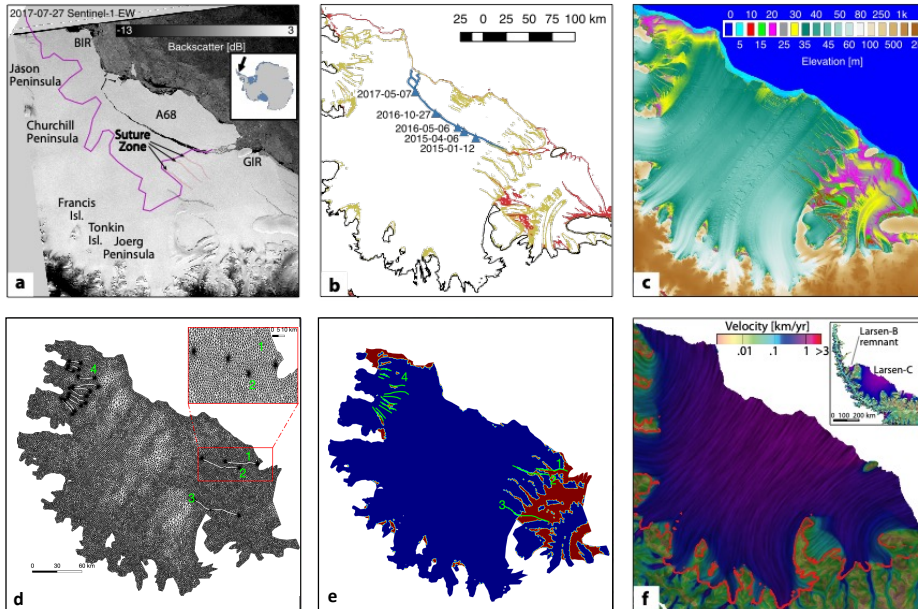
Figure 1.7: Model domain of the numerical work of Larour et al. (2021). Larsen Ice Shelf, Antarctic Peninsula with (A) backscatter image from Sentinel-1 EW on 27 July 2017 with Inset map for location in Antarctica and the location of the compressive arch of stability of the ice shelf (purple); (B) color-coded 20- (red), 40- (brown), and 100-m (black) contour levels in surface elevation with time-tagged (blue triangles) position of the rupture tip of A-68 from Sentinel-1a interferometric SAR; (C) surface elevation above mean sea level (in meters) from TanDEM-X digital elevation model in years 2013 and 2014; (D) ISSM finite-element mesh which is refined (Inset) around the rupture tips to capture the stress singularities. Rift 1 is the fracture that eventually calved iceberg A-68 (E) spatial distribution of ice mélange (red) deduced from the TanDEM-X digital elevation model using a threshold 250-m thickness within the active rifts 1 to 4 colored green; and (F) surface speed (in meters per year) on a logarithmic scale color coded from slow (brown) to fast (blue/red) with grounding line position (red) from ERS-1/2 differential SAR interferometry. Figure and adapted caption are from Larour et al. (2021).

through warm and soft suture zones, and then rapidly extended through cold and relatively brittle meteoric ice flow units after 2014. Finally, November 2016 marked the sudden reactivation of the rift, which - in less than one year - culminated with the iceberg separation, bringing the ice front into its inland-most known position.

The key result of Larour et al. (2021) is that the only numerical scenario that leads to accelerated opening of rift A-68 in 2016 is thinning of ice mélange, finding that ice shelf thinning alone cannot explain the rift propagation. So rift A-68 may have become unstable following a prolonged period of ice mélange ablation, which can be caused by a combination of warmer air and/or ocean temperature. Ice mélange filling critical pinning points of the ice shelf therefore offers a link between climate forcing and rifting, and in extension ice shelf stability. Since, ice mélange can

respond to climate forcing even decades before the main ice shelf unit, its evolution is pivotal in the ice shelf stability.

Several works have addressed how warm water can intrude into the Larsen C ice shelf cavity and curtail (a) ice mélange accretion processes and (b) enhance rift formation and propagation (Holland et al., 2009; Nicholls et al., 2012; Hutchinson et al., 2020; Harrison et al., 2022). The estimation of pathways of heat intrusion in the ice cavity and the impact on basal ablation at critical locations of the ice shelf such as ice rises is indeed crucial. Sustained basal thinning and enhanced rifting may indeed compromise the stability of the ice shelf (Borstad et al., 2013), decades before the appearance of superficial melting ponds. This has important consequences in the ice flow dynamics and in the rate at which upstream glaciers discharge freshwater in the Southern ocean. It is however unknown how the presence of the rift and the consequent calving of icebergs affected sub-shelf circulation patterns and the ocean heat delivery under the ice.

In particular, the following research questions (RQ) remain open, and they are addressed in Chapters 2 and 3:

RQ1 To what extent is the ocean dynamics underneath an ice shelf affected by the presence of a prominent kilometer-wide rift?

RQ2 To what extent is the ocean dynamics underneath an ice shelf affected by ice front retreat?

1.7   Ice fractures on the Jupiter moon Europa

Perhaps some of the most puzzling findings of the NASA *Voyager* mission toward the edges of the Solar System came from the investigation of moons around the gas giants Jupiter and Saturn. In the late 70s, *Voyager* retrieved a batch of images from the Jovian system and a team at the NASA's Jet Propulsion Laboratory (JPL) looked for the first time at curious lineaments features on the surface of the smallest of the four Galilean moons orbiting Jupiter: Europa. This relatively small moon showed a surface that is completely covered by lineaments, some of which with a dimension that is comparable with the moon's diameter. Since early studies, scientists have speculated that these lineaments consist of cracks of the icy surface - not very different from those observed on terrestrial ice shelves - with a variety of different implications in the dynamics and the possible habitability of this small Jovian moon (Pappalardo et al., 2009).

A couple of decades after the arrival of *Voyager* in the Jovian environment, the humanity had the chance to take a closer look at Europa, this time through the eyes of another NASA mission: *Galileo*. One of the most important discoveries of the *Galileo* mission is the evidence of an induced magnetic field on Europa. Surprisingly, the on-board magnetometer detected anomalies and peaks in the background magnetic field of Jupiter, while flying by the moon. These anomalies could have been due to two different causes: either Europa itself was producing a magnetic field or the observed magnetic field was induced by Jupiter. According to Khurana et al. (1998), magnetic measurements coming from the E4 and E14 passes of the spacecraft in the northern hemisphere of the moon alone could not determine whether Europa was indeed producing its own permanent magnetic field. Other measurements, especially in the southern hemisphere, were necessary in order to corroborate the direction and the amplitude predicted by numerical models. The E26 flyby was specifically designed for taking measurements of the orientation of the magnetic dipole, in order to distinguish whether it had variable direction or not. By the comparison with the signal obtained during previous flybys, scientists confirmed the presence of an induced magnetic field on Europa (Kivelson et al., 2000).

The evidence of an induced magnetic field played a pivotal role in the physical description of Europa's interior. An induced magnetic field, in order to be maintained in time, needs a conductive layer and a decoupled layer. This process is referred to in physics as a Faraday disk dynamo. The only possible explanation that would support the concept of an induced magnetic field is the presence of a global and saline (hence conductive) ocean layer right beneath the ice surface. The concept that Europa hosts a global subsurface ocean underneath an icy crust would also support the suggestions that the wide catalog of features that *Voyager* and *Galileo* observed on the surface of the moon would indeed resemble fractures on ice (Pappalardo et al., 1999).

The current representation of Europa's interior consists of a layered object (Anderson et al., 1998), which is characterized by a metallic core, surrounded by a rock mantle and a salty water ice-liquid outer shell. The thickness of the various layers remains poorly constrained given the paucity of available data (Hussmann et al.,
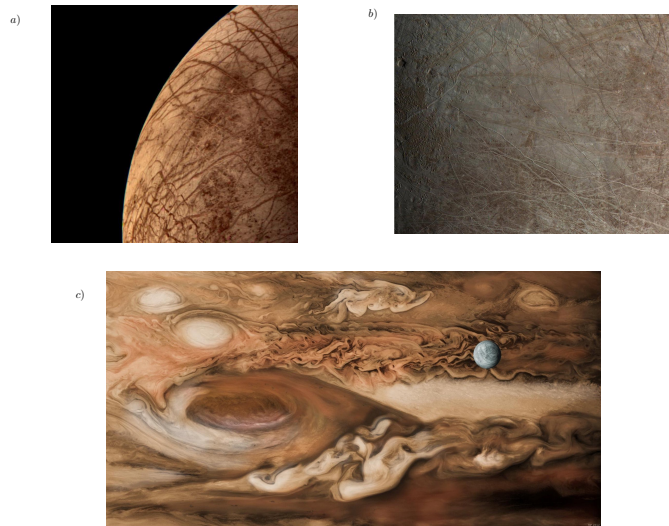
Figure 1.8: a) One of the first images retreived by NASA *Voyager* mission b) NASA *Galileo* mission c) Europa (on the right) in perspective with Jupiter's Great Red Spot.   Credit: NASA/JPL/Michael Benson/Kinetikon Pictures.

2016). In particular, the effective vertical dimension of the outer icy crust and the boundary between ice and ocean is vastly unconstrained. Numerical models based on the scarce observations estimate a thickness of the ice crust that spans between a few hundred meters to hundreds of kilometers (Billings and Kattenhorn, 2005). Most likely, the vertical dimension of the ice layer is not uniform across the moon, but varies with the geographical location. An accurate estimate of the ice layer is important in determining the habitability of this tiny ocean moon as the solid layer of ice could potentially shield the interior ocean from strong radiation from Jupiter, possibly providing energy and nourishing ingredients required for life. Given its pe- culiar stratification, Europa has indeed been identified as one of the most likely sites for life in the solar system (Greenberg et al., 2000). As thus, fractures observed on its surface may provide the only possible connection with the interior of this moon (Roth et al., 2014; Sparks et al., 2017). The evolution and origin of these lineaments therefore remain one of the most fascinating and important aspects to investigate.

Future explorations missions will further investigate the environment of Europa in order to address questions regarding the nature of the surface and interior and the prospect for material exchange between the two. In particular, *Europa Clipper* is a NASA spacecraft that will be sent to Europa to study its surface, subsurface ocean, and potential habitability. The mission aims to explore Europa's geology, composi- tion, and structure, as well as the interactions between its ice shell, ocean, and under- lying rocky mantle. The spacecraft will carry several scientific instruments, including cameras, spectrometers, and a radar to study the moon's surface and subsurface. The mission will conduct multiple flybys of Europa to gather data and images of the moon

and will improve our understanding of lineament features observed on the surface. These are particularly important as they aid planetary studies to understand past geological processes and reveal clues to subsurface oceans that may contain life. The following sections summarize the proposed causes for the formation of lineament patterns on Europa and briefly present the different types of features observed on its surface.

However, the dynamic evolution of fractures on the icy surface is poorly understood as observations are limited to the passing of *Voyager, Galileo* and a few flybys by the *Cassini* mission in the early 2000s. A common approach to interpret and better understand features observed on planetary bodies is to apply terrestrial-based morphological models and theories which are much more advanced given the large availability of in-situ and remote observations. The following research question (RQ) remains open and is addressed in Chapter 4:

> RQ3 Can we successfully apply terrestrial ice fracturing models to investigate how cracks propagate on the surface of Europa?

1.7.1 What causes the ice crust of Europa to fracture?

The most compelling theory that explains the presence of the lineament features observed on the surface of Europa is that the ice crust deforms and cracks due to the massive tidal forcing excerted by the moon's host planet: Jupiter. Europa, Io, and Ganymede - known as the Galilean moons - orbit Jupiter in a 1:2:4 Laplace resonance. This means that every time Ganymede completes one orbit around Jupiter, Europa completes two, and Io completes four. Furthermore, these moons are very close to being tidally locked to Jupiter, meaning their rotation period is roughly synchronous with their revolution period. This is similar to the relationship between the Earth and the Moon, where the rotation period is also synchronous with the revolution period.

The Laplacian resonance forces the Galilean moons to have a slight eccentricity, which means that variations in the distance between the moons and Jupiter cause a differential gravitational attraction within a single orbit (which takes 3.55 days for Europa). As a consequence, the tidal bulge experiences variations in intensity that range from a minimum at the apocenter to a maximum at the pericenter, causing a strong diurnal tidal oscillation. The tidal bulge's oscillations due to the slightly non-circular orbit of Europa lead to the primary tidal component reaching an amplitude of 200 m (Greenberg et al., 1998). Besides the tidal component related to non-zero eccentricity, there are two other sources of diurnal stress acting on Europa. Firstly, Europa's rotation axis is slightly inclined with respect to the orbital plane (Bills, 2005), which introduces a latitudinal oscillation in the tidal bulge. Secondly, the tidal bulge of the icy moon is forced to oscillate in longitude (and in latitude) (Rambaux, N. et al., 2011). These oscillations, that would also happen even in a circular orbit, are called physical libration and may induce further torque on the decoupled icy crust (Rhoden et al., 2010b). Given the extremely low temperatures at the surface of Eu-
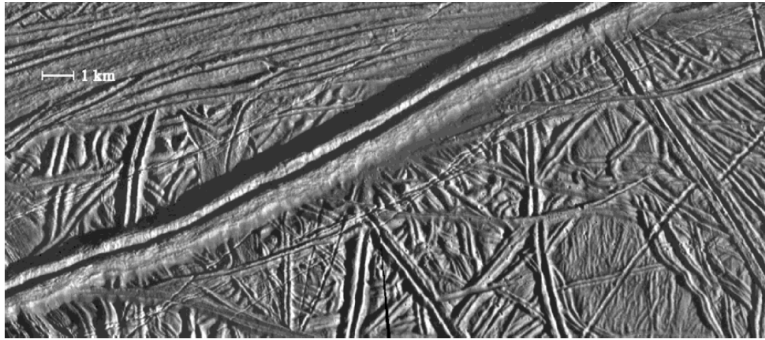
Figure 1.9: Ice ridge in the area of Bright Plains, from *Galileo* images taken during the flyby E6 (Greenberg et al., 1998). A central rift is surrounded by accumulated material, due to the progressive opening and closure of the fracture. Other similar ridges can be seen in the same image.

ropa (about 100 K (Spencer et al., 1999), constant surface deformation in response to such intensity in tidal oscillation is sufficient to explain the presence of lineaments as fractures on brittle ice.

However, Europa shows geological features that require a deformation field much larger than diurnal tides to be explained. A plausible cause of substantially higher stress on the surface is the slight asynchronicity of the rotation period with respect to the revolution. This relatively slow rotation of Europa around its axis could induce further accumulation of stress on the surface over timescales that are significantly higher than the revolution period. Although the timescale of non-synchronous stress is estimated to be on the order of 10^4 years (Greenberg et al., 1998, 2002; Hoppa et al., 1999), the physical representation of this secular motion is still unknown. Another secular forcing that affects the stress field on Europa could be polar wander due to asymmetry in the moon's mass, which alters the moment of inertia and leads the rotation axis to shift (Ojakangas and Stevenson, 1989). In conclusion, tides are considered the stress sources that continuously deform the brittle ice crust of Europa at different temporal and spatial scales. This leads to the formation of a wide catalog of ice fractures and lineaments observed on the surface.

1.7.2   Brief catalogue of Europa lineament features

The next sub-sections provide a brief summary of the most recognizable lineament features on the surface of Europa and the physical mechanisms that could potentially explain their presence.

Ridges

Ridges are perhaps the most commonly observed feature on the surface of Europa. They consist of a central lineament surrounded by accumulated material on both sides (Figure 1.9). One of the first attempts to describe the physics of ridges on

Europa was made by Pappalardo and Coon (1996), who drew similarities with ridge formation observed in Arctic sea ice. The authors proposed that these features are subject to opening and closing processes along the central fracture in response to tidal deformation, with material being progressively ejected from underneath the surface. Ridges imply a certain amount of time for substantial material to accumulate at their edges, so some of these features are thought to be the oldest lineaments on the surface of Europa.

Strike-Slips

Another type of lineament observed on the surface of Europa are strike-slips, which are fractures where two ice slabs slide parallel to each other. On Earth, strike-slips are common in rocks and solid materials. Examples of terrestrial strike-slips include the San Andreas fault in California and the Anatolia fault in Northern Anatolia. One of the largest lineaments observed on Europa is Astypalaea Linea in the southern hemisphere of the moon, whose length is around 800 km. The fault was discovered using *Voyager 2* images, based upon the presence of familiar strike-slip features including linearity, pull-aparts, and possible braids, and upon the offset of multiple piercing points (Tufts et al., 1999). The dynamic of strike-slip formation on Europa is again thought to be related to the diurnal tidal oscillation, which redistributes tensile and compressive stress along one orbit around Jupiter. Within a single orbit of Europa around Jupiter, the shear stress direction along a lineament changes from right-lateral to left-lateral in a process referred to as tidal walking (Hoppa et al., 1999, 2001a). The result is often a fracture that has substantial differential stress between the two flanks.

Cycloids

Besides ridges and strike-slips, some of the most puzzling lineaments observed on Europa are characterized by arcuate and cuspate segments around 100 km in length. The most evident cycloids can be seen in the southern hemisphere of the moon, and the further the cycloid is from the equator, the more arcuate pattern it resembles. The common understanding of cycloid formation is that after a fracture initiates and propagates throughout, the tensile stress threshold, which is caused by tidal forcing and is the driver of fracturing, may no longer be reached. After a tidal cycle has passed, the tensile strength is reached again at the point where the crack has stopped propagating. As a consequence, the crack starts to initiate again, with a direction different from the previous propagation event. This point, where the first crack ends and the new one is formed, is named a cusp.

1.8   Research objectives and dissertation outline

As detailed in this chapter, there are still many unanswered questions about ice fractures and their impact on the surrounding environment, both on terrestrial and planetary ice bodies. On Earth, the urgency of better understanding how ice behaves and how ice sheets will evolve in the future is driven by the current climate crisis. The ongoing loss of terrestrial ice sheets directly causes the global sea level to rise which, in turn, severely affects the lives of millions of people. Assessing the processes that contribute to ice loss is crucial to accurately project future rates of sea level rise. Moreover, the insights gained from studying terrestrial ice sheets can contribute to expanding our understanding of physics on other celestial bodies. With a focus on ice fractures, this dissertation explores their significant implications for the dynamics of Antarctic ice shelves, their interaction with the surrounding ocean, and the dynamics of icy moons within the Solar System.

In the rest of this document, I will focus on the impact of ice fractures and iceberg separation on the delivery of ocean heat under Antarctic ice shelves. Furthermore, I will apply a terrestrial-based fracture model to reproduce the behavior of ice fractures observed on the surface of Europa. Specifically, the following research questions will be addressed:

1. **To what extent is ocean dynamics underneath an ice shelf affected by the presence of a prominent kilometer-wide rift?**
   The ongoing thinning of Antarctic ice shelves - largely due to enhanced melting at their base in response to warming oceans - is known to accelerate the release of glacier meltwater into the world oceans, augmenting global sea level. Therefore, mechanisms of ocean heat intrusion under the ice base are crucial for projecting the future of Antarctic ice shelves. Furthermore, ice shelves are weakened by the presence of kilometer-wide full-thickness ice rifts, which are observed near the ice front of multiple ice shelves in Antarctica. However, their impact on ocean circulation around and below ice shelves has been largely unexplored, as ocean models are commonly characterized by resolutions that are too coarse to resolve the presence of rifts. In this thesis, I use the Massachusetts Institute of Technology general circulation model at high-resolution to investigate the sensitivity of sub-shelf ocean dynamics and ice shelf melting to the presence of a kilometer-wide rift in proximity to the ice front. This question is addressed in Chapter 2.

2. **To what extent is the ocean dynamics underneath an ice shelf affected by ice front retreat?**
   The calving of iceberg A-68 in July 2017, one of the largest icebergs ever observed, did not completely destabilize the Larsen C ice-shelf. However, this event brought the ice-front into a vulnerable position, which may lead to irreversible retreat in response to future calving. During ice-front retreat events, the temporary front location is often pinned by ice rises, rumples, islands, and shallow bathymetric features that buttress ice flow. On the Larsen C Ice Shelf,

basal melting around pinning points such as the Gipps and Bawden Ice Rises is thought to reactivate local rifts, potentially leading to calving events such as the one in 2017. However, pathways of ocean heat intrusion under Larsen C during and after the calving of iceberg A-68, along with the impact on basal ablation around local pinning points, remain poorly constrained. In this thesis, I use the Massachusetts Institute of Technology general circulation model at high-resolution to investigate the impact of ice front retreat on the sub-shelf ocean dynamics of the Larsen C ice shelf. This question is addressed in Chapter 3.

3. **Can we successfully apply terrestrial ice fracturing models to investigate how cracks propagate on the surface of Europa?**
Existing lineaments on the surface of the Jovian moon Europa are thought to be the result of ongoing crack formation. Perhaps some of the most puzzling lineaments observed on Europa are characterized by arcuate and cuspate segments of around 100 km in length. These features are called cycloids, and their orientation can be explained by formation due to tensile cracking. Although cycloids have been extensively studied, their propagation rate and the total duration of fracturing events have not been sufficiently described in past models. In this thesis, I apply an existing terrestrial fracture mechanics model to reproduce the shape and propagation of cycloids on the icy surface of this Jupiter moon. This question is addressed in Chapter 4.

Lastly, I will conclude this dissertation in Chapter 5, where I summarize the key findings of the three research projects. Here, I will also describe the extent to which these research objectives have been achieved and draw conclusions and final remarks.

Chapter 2

Ocean dynamics underneath cracked ice shelves

> Make everything as simple as possible, but not simpler.
>
> — Albert Einstein

2.1 Summary

Land ice discharge from the Antarctic continent into the ocean is restrained by ice shelves, floating extensions of grounded ice that buttress the glacier outflow. The ongoing thinning of these ice shelves - largely due to enhanced melting at their base in response to global warming - is known to accelerate the release of glacier meltwater into the world oceans, augmenting global sea level. Mechanisms of ocean heat intrusion under the ice base are therefore crucial to project the future of Antarctic ice shelves. Furthermore, ice shelves are weakened by the presence of km-wide full-thickness ice rifts, which are observed all around Antarctica. However, their impact on ocean circulation around and below ice shelves has been largely unexplored as ocean models are commonly characterized by resolutions that are too coarse to resolve their presence. Here, we apply the Massachusetts Institute of Technology general circulation model at high-resolution to investigate the sensitivity of sub-shelf ocean dynamics and ice-shelf melting to the presence of a km-wide rift in the proximity of the ice front. We find that (a) the rift curtails water and heat intrusion beneath the ice-shelf base and (b) the basal melting of a rifted ice shelf is on average 20 % lower than for an intact ice shelf under identical forcing. Notably, we calculate a significant reduction in melting rates of up to 30 % near the grounding line of a rifted ice shelf. We therefore posit that rifts and their impact on the sub-shelf dynamics are

important to consider in order to accurately reproduce and project pathways of heat intrusion into the ice-shelf cavity.

2.2   Introduction

The Antarctic Ice Sheet (AIS) is losing mass at an accelerated pace (Paolo et al., 2015). Between 2009 and 2017, its ablation rate was approximately 252 Gigatons of ice every year (Gt yr^{-1}), with an estimated acceleration of 94 Gt yr^{-1} each decade since 1979 (Rignot et al., 2019). The AIS stores an amount of freshwater that - if completely released in the world oceans - would arise the global sea level by 58 m (Morlighem et al., 2020). Recent projections indicate an increase in the future commitment of the AIS to global sea level by up to 2.8 m within the next 300 years (Poertner et al., 2019), in response to past and ongoing global warming.

The discharge of glacier ice from the Antarctic continent into the ocean is restrained by floating extensions of the AIS along most of its perimeter. These extensions are called ice shelves and form when the seaward margin of the continental ice detaches from the underlying bedrock and becomes afloat at a location called the grounding line. Ice shelves are critical in the stability of the AIS as they act as a "cork in the bottle", by buttressing upstream grounded ice from further sliding into the ocean (Dupont and Alley, 2005). Therefore, the loss of floating ice shelves - despite not directly adding to sea level - leads to accelerated mass discharge from outlet glaciers into the ocean (Rignot et al., 2004; Scambos et al., 2004), arising the global sea level. So understanding the evolution of ice shelves is crucial to reconstruct AIS mass loss.

The strongest ablation process of Antarctic ice shelves occurs at their base (Rignot et al., 2013), where ice is flushed by ocean water and melts from underneath. As the southern ocean is currently warming (Schmidtko et al., 2014) in response to climate change, the AIS mass loss is accelerating (Paolo et al., 2015). Observations show that sustained melting at the grounding line - when warm water has direct access (e.g. Nakayama et al., 2018, 2019) - causes it to migrate landward (e.g. Rignot and Jacobs, 2002). This process leads to further ungrounding of continental ice and accelerates freshwater discharge from outlet glaciers into the ocean (e.g Thomas et al., 2004). Albeit critical in the ice shelf-ocean dynamics, the pathways by which ocean heat reaches the grounding line remain elusive, and direct measurements in these locations are sparse because of the challenges of obtaining them.

Ice shelves are often categorized as "cold water" or "warm water", depending on the water mass that dominates the continental shelf and the melting processes that drive basal ablation (e.g. Dinniman et al., 2016). In the proximity of cold water ice shelves, a water mass that is commonly found is High Salinity Shelf Water. It is formed by brine rejection during winter sea ice formation and can down-well near the coast due to its increased density. This hypersaline water can intrude into deep sections of the ice cavity (Nicholls et al., 2009) and - despite being sourced at the surface freezing temperature (-1.9^{o}C) - melts the ice bottom because the freezing point of seawater decreases with increasing pressure. These processes are observed under

large ice shelves in the Weddell and Ross seas, where sea ice production is abundant. In contrast, small warm water ice shelves in the Bellingshausen and Amundsen seas are directly flooded by Circumpolar Deep Water that spills onto the continental shelf and often has direct access to the grounding line (e.g. Nakayama et al., 2018, 2019). As a result of this warm water mass (1^oC) reaching the location where the ice detaches from the underlying bedrock, these ice shelves are rapidly retreating and thinning (e.g. Shepherd et al., 2004; Seroussi et al., 2017).

Iceberg calving represents the second largest ablation process of Antarctic ice shelves (Rignot et al., 2013). The seaward extension of ice shelves is often curtailed by full-thickness ice rifts - usually propagating in a direction transverse to the ice flow - that episodically separate ("calve") large tabular icebergs. While ice rift width is usually less than 10 km, their length can extend up to 300 km. Rifting may cause the ice front to recede inland of the so-called "compressive arch". If rifts break beyond this critical threshold - where the ice shelf transitions from uni-axial to bi-axial extension (Lipovsky, 2020) - its buttressing force may be compromised (Fürst et al., 2016) and the ice-shelf retreat may become irreversible (Doake et al., 1998). Rifts are known to propagate as a series of nearly instantaneous events, but they can also experience periods of inactivity that can last up to several months and years (Bassis et al., 2005; Walker et al., 2015; Banwell et al., 2017). The relatively long periods of dormancy raise questions about whether rifts may have any impact on oceanic processes beneath the fractured ice shelf. In this paper, we aim to build understanding of this topic.

Evidence shows that rifts are often capped with ice mélange - a combination of accreted ice, windblown snow, and ice-shelf fragments - whose thickness is one to two orders of magnitude larger than regular sea ice (Orheim et al., 1990; Breyer and Fricker, 2022) and which possibly holds rift flanks together (Rignot and MacAyeal, 1998; Larour et al., 2021). Besides sea ice accretion from atmospheric cooling, Khazendar and Jenkins (2003) showed that ice rifts can be filled with marine ice, growing from ocean freezing. According to this process, buoyant plumes - formed after light meltwater is released from lower parts of the rift sidewalls - may freeze after relatively cold seawater drops below the freezing temperature in shallower sections of the rift, as the freezing temperature of seawater decreases with depressurization ("ice-pump" mechanism, Lewis and Perkin, 1983). This theory could explain (a) the presence of water below the freezing point observed in basal fractures (Orheim et al., 1990; Lawrence et al., 2023) and (b) the possible downwelling of dense water to compensate for the upwelling at the sidewalls (firstly hypothesized by Potter and Paren, 1985). Further numerical simulations of Jordan et al. (2014) confirmed these results by arguing that frazil ice deposition in the upper parts of the rift is a key driver in the overturning circulation within ice fractures.

Nevertheless, previous studies on rift-ocean interactions are limited to a 2-D representation of the rift environment (horizontal-vertical) and neglect the impact of rifts and water formed within them on the dynamics of deeper sections of the ice-shelf cavity, despite the known importance of accurately representing the cavity geometry (Goldberg et al., 2012; Schodlok et al., 2012). Moreover, regional ocean models of

Antarctic ice shelves usually employ resolutions that are too coarse to capture km-wide rifts, hence their interaction with the sub-shelf dynamics is often neglected. Mixing processes under rifted ice shelves and pathways of heat intrusion toward the grounding line remain therefore particularly unresolved.

In order to determine whether ice rifts impact the ocean heat intrusion toward the grounding line beneath ice shelves, in this paper we assess (a) the sensitivity of sub-shelf ocean circulation and basal melt distribution to the presence of a km-wide ice-capped rift near the ice-shelf front and (b) the impact of such a rift on the intrusion of off-shelf water. To this end, we run a 3-D ocean model with idealized bathymetry and ice-shelf geometry, at a resolution (250 m) that can capture a km-wide rift. To further investigate the impact, we employ a suite of sensitivity simulations for a range of rift widths, thermal ocean forcing, and magnitude/direction of off-shelf ocean currents.

2.3   Methodology

2.3.1   Model set-up

To perform our sensitivity study, we use the Massachusetts Institute of Technology general circulation model (MITgcm). Ocean dynamics is governed by the hydro-static 3-D Navier-Stokes equations under the Bousinessq approximation. A non-linear second-order flux-limiter advection scheme is applied. The equation of state follows the modified UNESCO formula (Jackett and McDougall, 1995). Eddy diffusivities of temperature and salinity are held constant to 5.44×10^{-7} $m^2 s^{-1}$ in the vertical dimension, while we use a lateral biharmonic Leith eddy viscosity factor of 2. Vertical ocean mixing is governed by shear instability and internal wave activity and approximated in MITgcm with the non-local K-Profile parameterization (KPP, Large et al., 1994). Ice-ocean processes at horizontal and vertical interfaces are represented by the three-equation model. Equations and adopted approximations are sketched in Section 2.8.1.

We employ an idealized ice shelf-ocean model configuration that relies on a Cartesian coordinate system (100 km x 200 km x 600 m, Figure 2.1a-b) on an f-plane with Coriolis frequency set to -1.4×10^{-4} rad s^{-1}, which corresponds to a latitude of 75°S. Horizontal and vertical grid spacings are set to 250 m and 10 m, which constrain the time-step to 30 s in order to ensure numerical convergence. The model relies on an isotropic mesh and uses a partial cell formulation (Adcroft et al., 1997), with a minimum open cell fraction of 30 %. It is important to acknowledge that the resolution employed here does not resolve melt-driven plumes (Xu et al., 2012; Burchard et al., 2022) nor the physics of frazil ice accretion within the water column.

The ice-shelf thickness at the ice front (located at km 85 east) is set to 200 m slightly increasing to 250 m from km 35 east along a constant ice-shelf slope towards the grounding line (km 0 east). Our simulations include a rift as a discontinuity in the ice-shelf draft. Its west flank is located at a fixed distance (67.5 km) from the grounding line and rifts are introduced with variable width. Melting and freezing
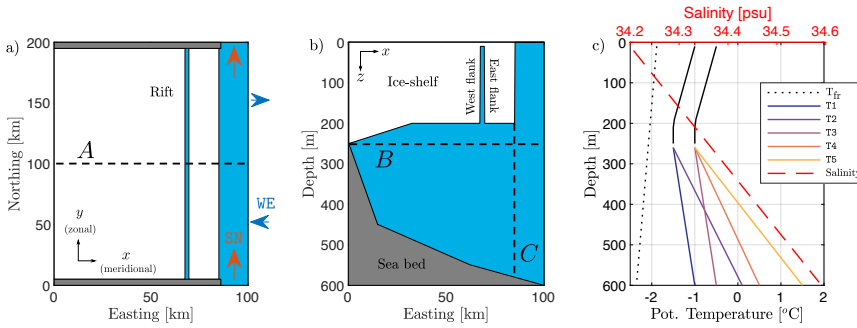
Figure 2.1: Model domain sketches and ocean profiles. Panel a shows a schematic view of a horizontal cross-section of the ice shelf (white), rift and ocean (blue), and seabed (grey) at 150 m depth. Red and blue arrows are directions of the alternative boundary conditions, which are termed here as south-to-north (SN) and west/eastward (WE) flow. In the simulations with a rift, the west flank of the rift is fixed at km 67.5 east. Beside runs with an intact shelf, the rift is introduced with a width of 1, 2 and 3 km and is filled with 15 m of ice shelf. Panel b shows a schematic view of a vertical cross-section of the model domain at km 100 north. Black dashed lines labeled *A*, *B* and *C* are horizontal and vertical cross-sections useful to visualize model results. Panel c shows potential temperature and salinity profiles as initial and boundary conditions of the sensitivity experiments. Solid lines are initial and boundary conditions of temperature for "cold water" and "warm water" regimes. Cold and warm profiles are characterized by two (T1, T2) and three (T3, T4, T5) bottom temperatures. The red dashed line is the salinity profile, constant in all experiments. Black dotted line is the freezing temperature of seawater (T_{fr}).

processes are active at horizontal and vertical interfaces between the ice and ocean, including the ice base, ice front, rift top, and rift sidewalls. Since the ice-shelf geometry is fixed in time, the location of the ice-ocean interfaces does not change with melting and freezing.

Furthermore, the rift is filled with 15 m of ice shelf, as a buffer layer between the atmosphere and ocean, which approximates an "ice-capped" rift and does not aim to reproduce ice mélange properties. Although ice mélange is often thought to be controlled by processes that are similar to those of sea ice, evidence shows that the heterogeneous material filling km-wide rifts reaches thicknesses that are one to two orders of magnitude larger than sea ice (Orheim et al., 1990; Breyer and Fricker, 2022). Such a thick layer of ice can completely separate the liquid ocean from the atmosphere (Khazendar and Jenkins, 2003). By adopting the "ice-capped" approximation, we only focus our analysis on sub-shelf ocean processes introduced by the rift, while atmospheric and sea ice formation processes in the open ocean are neglected in this study.

The bathymetry consists of a prograde slope, deepening from the grounding line depth of 250 m to a maximum depth of 600 m at the eastern boundary (km 100 east). A grounding line depth between 200 m and 300 m, while relatively shallow, is characteristic of ice shelves such as some regions of the Larsen C ice shelf

in the East Antarctic Peninsula (cold water) or the Wilkins and Bach ice shelves in the West Antarctic Ice Sheet (warm water). Furthermore, although bathymetric sills and wedges can substantially alter the sub-shelf circulation by squeezing the water column and acting as a topographic barrier (Bradley et al., 2022), their presence is not considered here in order to generalize the seabed geometry as far as possible.

Finally, it is important to note that our simulations disregard sub-glacial discharge at the grounding line. While this assumption may neglect important mixing processes where the ice shelf detaches from the underlying bedrock (Wei et al., 2020; Nakayama et al., 2021), it helps to focus our analysis on the impact of on-shelf water intrusion and its interaction with the rift.

2.3.2   Simulations design

We performed a total of 120 simulations with combinations of rift width, ocean temperature, velocity, and direction of ocean currents flowing in the open ocean (Table 2.1).

Our simulations include a rift as a discontinuity in the ice-shelf draft which is introduced with a width of 1, 2 or 3 km, beside a control run with an intact ice shelf (no rift). Ocean circulation in the open ocean is prescribed as an inflow of varying magnitude (1, 5 and 10 cm s^{-1}) as Dirichlet boundary condition at the open ocean section of the south, north and east boundaries. We perform two sets of experiments with alternative open boundaries (Figure 2.1a). In the first - which we term here as south-to-north flow case (SN) - we "close" the eastern boundary (non-penetration condition) and prescribe an inflow at the southern boundary which is balanced by an outflow at the northern boundary to conserve mass. In the second - which we term here as west/eastward flow case (WE) - we close northern and southern boundaries and, at the eastern bound, we impose an inflow between km 0 - 100 north which is balanced by an outflow between km 100 - 200 north. The SN scenario can be seen as an idealization of along-ice front ocean currents, while WE cases represent across-shelf currents.

We initialize and force the simulations with idealized temperature-salinity profiles, distinguishing between "warm" and "cold" regimes, which are prescribed as initial and boundary conditions (Figure 2.1c). Each profile is characterized by a mixed layer for the upper 250 m which linearly changes to (a) two different bottom temperatures in the cold regime, and (b) three different bottom temperatures in the warm regime (-0.5^{o}C in experiment T3, 0.5^{o}C in T4 and 1.5^{o}C in T5). The salinity profile increases linearly from 34.2 psu at the surface to 34.6 psu at 600 m depth in all experiments. The chosen temperature profiles are representative of temperature ranges observed nearby ice shelves in Antarctica (Orsi and Whitworth, 2005). Warm water ice shelves in the Amundsen and Bellingshausen seas are represented by experiments under T5 forcing. In contrast, cold scenarios under T1 are similar to real conditions of cold water ice shelves in the Weddell and Ross seas. The remaining scenarios (T2–4) can be seen as representative of "in-between" ice shelves, e.g. Totten Ice Shelf on the Sabrina Coast.

Table 2.1: Matrix of sensitivity experiments. Our study addresses the sensitivity of sub-shelf ocean dynamics to: four rift width configurations, two flow directions, three flow velocities and five temperature profiles, for a total of 120 experiments. In the following naming schema, R refers to rift width of 0 (intact shelf), 1, 2 or 3 km, SN/WE1–10 refers to velocity at the open boundaries for south-to-north and west/eastward cases with intensity of 1, 5 or 10 cm s^{-1} and T refers to temperature.

	T1	T2	T3	T4	T5
R0	SN/WE1-10	SN/WE1-10	SN/WE1-10	SN/WE1-10	SN/WE1-10
R1	SN/WE1-10	SN/WE1-10	SN/WE1-10	SN/WE1-10	SN/WE1-10
R2	SN/WE1-10	SN/WE1-10	SN/WE1-10	SN/WE1-10	SN/WE1-10
R3	SN/WE1-10	SN/WE1-10	SN/WE1-10	SN/WE1-10	SN/WE1-10

2.3.3 Formal analysis

All experiments are integrated for seven years. A quasi-steady state is reached in all simulations during the fifth year. To assess the impact of the rift on the sub-shelf dynamics, we focus on differences in modeled melt rate (equations in Section 2.8.1), heat transport toward the ice shelf interior (equations in Section 2.8.2) and sub-shelf circulation between simulations with intact and rifted ice shelves. To do so, we use average values from the last year of integration, unless differently specified.

The discussion on the sub-shelf circulation and entrainment of water masses under the ice shelf is supported by the temporal evolution of virtual passive tracers. Tracers are initially released in the ice shelf cavity (tr01) and in the rift (tr02), with concentrations set at 1.0 at the beginning of the fifth year. Passive tracers do not affect the local density and advect with the local water flow for two years, until the end of the simulations.

2.4 Results

Section 2.4.1 presents and discusses spatially-averaged melt rates and heat transport toward the interior of the ice shelf cavity across the 120 experiments, with emphasis on the sensitivity of basal melt to rift widths, thermal ocean forcing and magnitude/direction of off-shelf ocean currents.

Furthermore, we focus on the differences between intact and rifted simulations while sensitivity parameters are fixed to temperature profile T2 and current velocity of 5 cm s^{-1} in either SN or WE direction, unless differently specified. This sub-set is chosen as representative simulations. Section 2.4.2 shows the distribution of melt rate along the ice-shelf base discussing differences between intact and rifted experiments. Additionally, section 2.4.3 shows the distribution of melt and freeze rates along the rift surfaces. Finally, section 2.4.4 discusses the sub-shelf circulation by analysing barotropic streamfunction and the evolution of passive tracers tr01 and tr02 under intact and rifted ice shelves. The temporal evolution of the horizontal
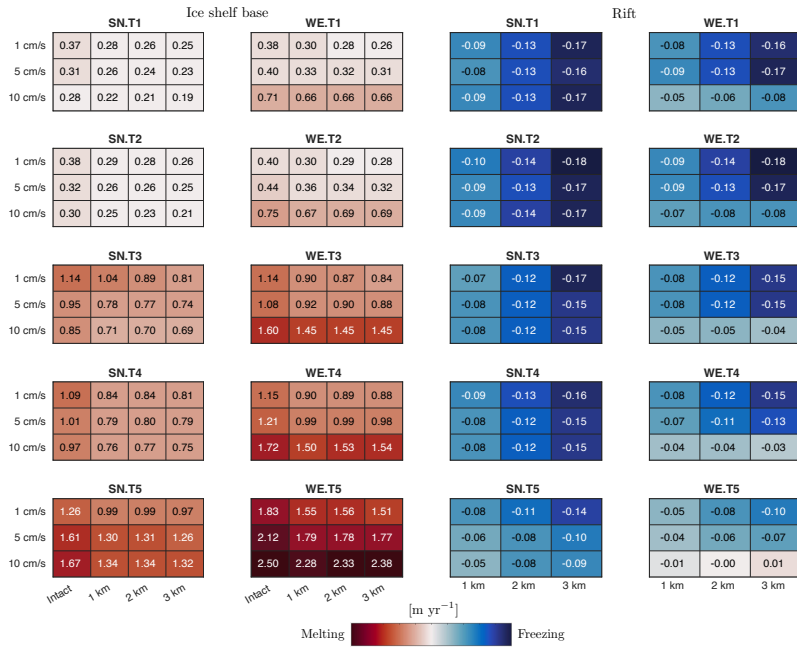
Figure 2.2: Heat-maps of average melt rate integrated along the ice-shelf base (columns one and two) and in the rift (columns three and four) for the 120 sensitivity experiments. Values are calculated with respect to temperature profile (panel), flow velocity (row) and rift width (column).

distribution of `tr01` across a horizontal cross-section of the model domain (255 m, cross-section *B* in Figure 2.1b) is provided as video supplement.

2.4.1 Average melt rate across all simulations

In order to summarize the impact of the selected sensitivity parameters on ice-shelf melting, we calculate spatially-averaged melt rate integrated along (a) ice-shelf base and (b) rift surfaces (both rift top and sidewalls are active ice-ocean interfaces) for the 120 simulations (Figure 2.2). The intrusion of off-shelf water supplies the heat for melting the ice base, and our simulations show that heat transport toward the grounding line increases with higher thermal forcing (Figure 2.3), with a consequent increase in basal melt rate for higher ocean temperatures.

Furthermore, the intensity of basal melt depends on the direction and velocity of the applied boundary condition. In order to conserve potential vorticity, ocean flow tends to maintain its motion along lines of constant depth (isobaths). So water columns are "stiff" in the vertical direction (Taylor columns) and tend to deflect along isobaths. In our case, isobaths are parallel to the ice front by model design. The abrupt gradient in the water column thickness that is introduced by the ice front therefore acts as a barrier that limits the flow entering the cavity (e.g Grosfeld et al., 1997; Wåhlin et al., 2020).
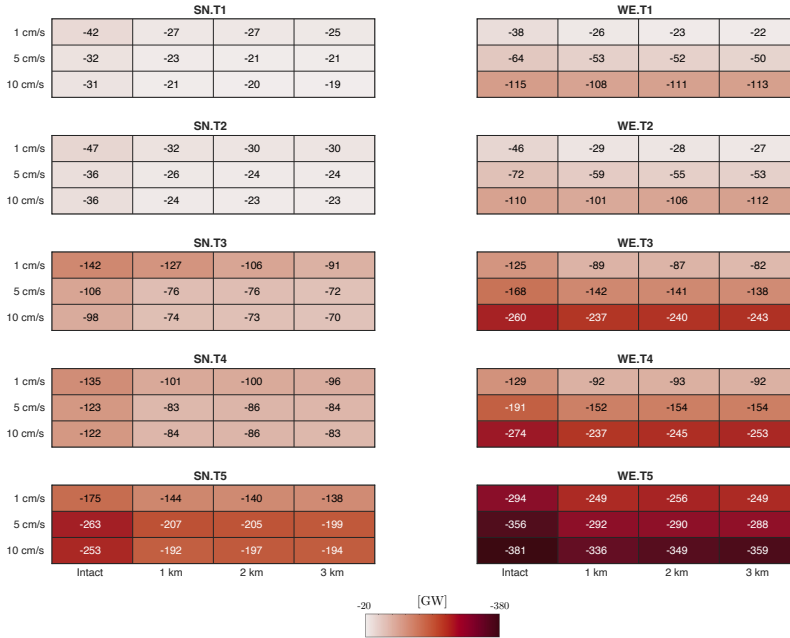
SN.T1

	Intact	1 km	2 km	3 km
1 cm/s	-42	-27	-27	-25
5 cm/s	-32	-23	-21	-21
10 cm/s	-31	-21	-20	-19

WE.T1

	Intact	1 km	2 km	3 km
1 cm/s	-38	-26	-23	-22
5 cm/s	-64	-53	-52	-50
10 cm/s	-115	-108	-111	-113

SN.T2

	Intact	1 km	2 km	3 km
1 cm/s	-47	-32	-30	-30
5 cm/s	-36	-26	-24	-24
10 cm/s	-36	-24	-23	-23

WE.T2

	Intact	1 km	2 km	3 km
1 cm/s	-46	-29	-28	-27
5 cm/s	-72	-59	-55	-53
10 cm/s	-110	-101	-106	-112

SN.T3

	Intact	1 km	2 km	3 km
1 cm/s	-142	-127	-106	-91
5 cm/s	-106	-76	-76	-72
10 cm/s	-98	-74	-73	-70

WE.T3

	Intact	1 km	2 km	3 km
1 cm/s	-125	-89	-87	-82
5 cm/s	-168	-142	-141	-138
10 cm/s	-260	-237	-240	-243

SN.T4

	Intact	1 km	2 km	3 km
1 cm/s	-135	-101	-100	-96
5 cm/s	-123	-83	-86	-84
10 cm/s	-122	-84	-86	-83

WE.T4

	Intact	1 km	2 km	3 km
1 cm/s	-129	-92	-93	-92
5 cm/s	-191	-152	-154	-154
10 cm/s	-274	-237	-245	-253

SN.T5

	Intact	1 km	2 km	3 km
1 cm/s	-175	-144	-140	-138
5 cm/s	-263	-207	-205	-199
10 cm/s	-253	-192	-197	-194

WE.T5

	Intact	1 km	2 km	3 km
1 cm/s	-294	-249	-256	-249
5 cm/s	-356	-292	-290	-288
10 cm/s	-381	-336	-349	-359

[GW]   -20   -380

Figure 2.3: Heat-maps of total heat transport HT (eq. A4) across the meridional cross-section passing through the ice front (km 85 east, cross-section C in Figure 2.1b) for the 120 sensitivity experiments. The negative sign means that the heat transport is directed toward the ice cavity interior. Values are calculated with respect to temperature profile (panel), flow velocity (row) and rift width (column).

Our WE experiments are a representation of across-shelf water currents that are forced perpendicularly to the ice front and are therefore associated with stronger on-shelf mass and heat intrusion as the forced flow across isobaths intensifies. As a consequence, basal melt increases with stronger WE flow and large melt occurs near the ice front (further discussion in section 2.4.2), regardless of thermal forcing and/or rift presence/width. On the other hand, SN simulations are representative of along-front water currents. Stronger SN currents therefore imply an enhanced tendency of the flow to follow along-front isobaths and, in turn, to further isolate the ice shelf cavity from mass and heat intrusion. As a consequence, SN experiments show a much lower heat intrusion when compared to WE experiments, which also results in large melt differences. Furthermore, we find that intact SN experiments under thermal scenario T1 to T4 show a drop in melt rate with a strengthening of the boundary flow. The only set of SN experiments that shares with WE the same trend between melt and boundary flow intensity are experiments under T5 forcing.

The reason behind this discrepancy in basal melt with respect to boundary flow between SN experiments T1–4 and T5 resides in the higher heat transport that the latter boundary flow implies (heat transport in T5 is twice as large as in T4, Figure 2.3, while T4 temperature is only 1°C colder than T5). Extreme warm cases under thermal forcing T5 result in a much higher heat transport across the ice front in

response to a stronger flow, with a consequent higher average melt rate. In this case, the largest contribution to the average melt rate increase is indeed concentrated near the ice front.

On average, across all experiments, melting in rifted simulations is 20 % lower and the heat intrusion is 20 % weaker than that computed for intact shelves under an identical forcing scenario. Our simulations also show that melt rate generally decreases with rift widening in all SN experiments and in WE experiments forced with a weak boundary flow (1 and 5 cm s^{-1}). The only exceptions are WE experiments under a 10 cm s^{-1} boundary flow, where basal melt increases with rift widening. The differences in melting with respect to rift presence/width can be further investigated by evaluating heat fluxes in the rift.

The melt regime inside the rift is indeed very different from the ice-shelf base, as we find that this environment is dominated by freezing in almost all experiments. The only exceptions are WE experiments at 10 cm s^{-1} under thermal forcing T5, where freezing in the 3 km rift is stopped. Following the three-equation model (Section 2.81), melting at the ice base freshens the ambient water and increases its buoyancy while freezing in the rift leads to water salinification and loss of buoyancy. These processes can also be quantified as a (negative) salt flux at the rift base (Figure 2.12), whose intensity trends match the dependency of freezing rate with respect to sensitivity parameters. Freeze distribution along the rift surfaces is further investigated in section 2.4.3.

Freeze rate in the rift shows the same dependency on thermal forcing as the basal melt rate discussed above. As the ocean temperature increases, freezing processes in the rift are inhibited and freeze rate decreases. However, differently than in the case of basal melt, we find that strengthening the boundary currents returns a negligible impact on the freeze rate in most experiments. The only exceptions are SN experiments under thermal forcing T5 and WE experiments at 5 and 10 cm s^{-1}, where the stronger currents lead to progressively lower freeze rate.

Finally, we find that freezing in the rift and the associated salt flux at the rift base increases with rift widening in almost all experiments with the only exception being WE experiments under a 10 cm s^{-1} boundary flow. The anomaly of this last case can be explained with the analysis of melt/freeze pattern in the rift and its dependency to rift width (section 2.4.3).

2.4.2   Melt pattern at the ice-shelf base

In this section, we discuss the basal melt distribution along the ice-shelf base and the calculated anomalies between intact and rifted shelves.

For simulations with an intact shelf, it is possible to distinguish three meridional regions (Figure 2.4a,e). These are characterized by distinct melting regimes, which can be quantified with the spatially-averaged melt rate over the chosen regions (Figure 2.5). We term these regions as grounding line (km 0 - 32.50 east), center (km 32.50 - 70.75 east) and front (km 70.75 - 85 east). The western-most region of intact experiments, adjacent to the grounding line, is dominated by similar average melt
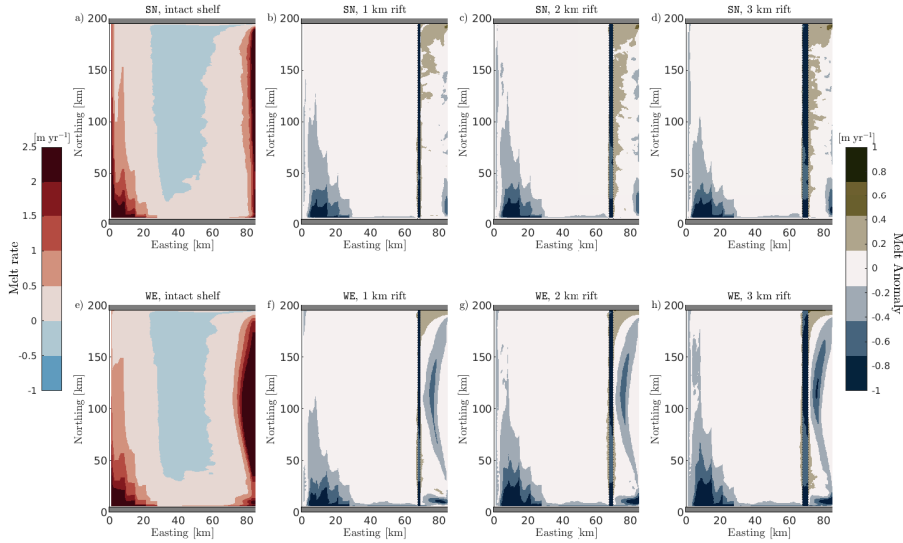
Figure 2.4: Comparison of horizontal distribution of ice-shelf basal melt rates for different rift widths. Upper and lower panels correspond to SN and WE boundary currents of 5 cm s^{-1}, respectively. The cold temperature profile T2 is used for all simulations. The first column shows the horizontal distribution of melt rate of intact experiments (a,e). Panels b-d and f-h show the horizontal distribution of melt anomaly, which is calculated as the difference between melt rate in the rifted shelf simulations with respect to intact cases under the same forcing conditions. Left colorbar refers to melt rate, while right colorbar refers to melt anomaly.

between SN and WE cases. These are also the deepest sections of the ice shelf (255 m), and we show in section 2.4.3 that fresh meltwater that is formed here tends to buoyantly rise along the ice-shelf slope. The shallower center region (200 m) shows large patches of water freezing, as water drops below the freezing temperature since this increases with lower pressure. On average, this region melts at a negligible rate in both SN and WE intact experiments. Finally, the front region - directly in contact with water transport in the open ocean - experiences melting rates that are about twice as large in the WE case with respect to the SN case.

The introduction of the rift results in a redistribution of heat along the entire ice-shelf base, which can be quantified in each meridional region identified for intact cases (Figure 2.4, 2.5 and Figure 2.11 for relative change). Some of the impact is found in the central region, where the rift is actually located. In the intact case, this region is dominated by slow melting. Freezing processes that occur in the rift drive here a reduction in melt rate, which is progressively reduced by increasing the rift width. As a consequence, central regions of rifted cases show a generalized freezing. We indeed find that average freezing in the rift increases with larger rifts, with the only exception of WE experiments under 10 cm s^{-1}. The general behavior is due to a progressively larger area that is brought in contact with cold water dropping below
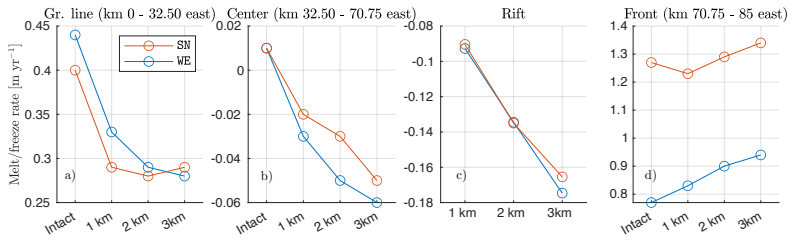
Figure 2.5: Spatially-averaged melt/freeze rate as a function of rift width for the three regions defined as grounding line, center and front. Values are referring to SN and WE experiments at 5 cm s^{-1} while the temperature profile is fixed to T2. Positive means melting and negative means freezing.

the freezing point, which increases with wider rifts.

The presence of the rift also leads to faster melting in the frontal region, where the model simulates a relative increase in melt rate of 2 % in the SN case and of 12 % in the case of WE on average with respect to intact cases. Finally, our model results show that the region adjacent to the grounding line in rifted experiments returns a negative anomaly in the average melt rate with respect to intact simulations. When the rift is introduced, the grounding line region experiences 30 % less melt rate than in the intact case under both SN and WE. WE simulations also show a net drop in melt rate in this region with rift widening, while in SN cases rift widening results in a negligible impact.

2.4.3   Melt pattern in the rift

It has been already discussed how the majority of experiments show that, on average, the rift environment is dominated by freezing (Figure 2.2). In this section, we address how freezing patterns are distributed along the rift boundaries. The following analysis refers to SN and WE experiments with a 2 km wide rift and boundary flow at 5 cm s^{-1} and 10 cm s^{-1} under thermal forcing T2.

Along the rift sidewalls, our simulations show that melting occurs at their deeper levels and freezing at the top (Figure 2.6). This bimodal pattern along the rift flanks is a result of the ice-pump mechanism active within the rift (Khazendar and Jenkins, 2003), as the freezing point of seawater increases with decreasing pressure. After melting in deeper sections of the rift, cold and fresh meltwater rises along the west flank (Figure 2.6), following an overturning pattern that is similar to the "melt-driven" experiments of Jordan et al. (2014). Meltwater reaches the freezing point at a depth of around 120 m and water re-freezes above this level and at the rift top. Freezing in shallow portions of the rift leads to salinification of the ambient water and a consequent loss of buoyancy. The upwelling of buoyant water along the west flanks is generally balanced by the sinking of denser water along the east flank. We term the water mass that interacts with the rift as Rift Water. This water is tracked by passive tracer tr02, which is released in the rift environment at the beginning of the 2 years of simulations. The downward transport of Rift Water can also be quantified
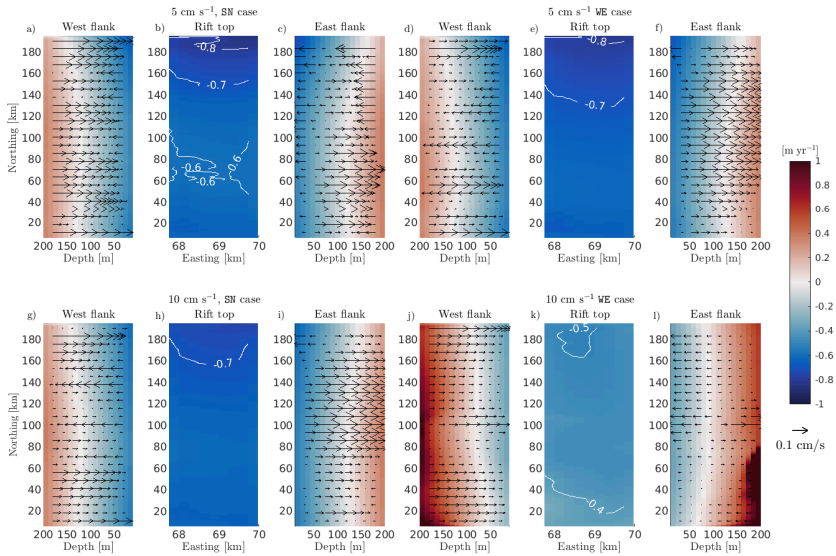
Figure 2.6: Comparison of melt rate distribution (both color-map and contour lines) along rift flanks and top of a 2 km wide rift under 5 and 10 cm s^{-1} boundary forcing. The cold temperature profile T2 is used for all simulations. West flank is closer to the grounding line while the east flank is closer to the ice front (see Figure 2.1b). Panels a-f correspond to SN and WE boundary currents of 5 cm s^{-1}, while panels g-n correspond to boundary currents of 10 cm s^{-1}. Positive means melting and negative freezing. Arrows are vertical velocity along the rift flanks.

as a (negative) salt flux through the rift base (Figure 2.12).

While the SN flow increases from 5 to 10 cm s^{-1}, the impact on the rift freeze is negligible (Figure 2.6a-c to g-i). In contrast, strengthening the WE flow to 10 cm s^{-1} (Figure 2.6d-f to j-l) has a major impact in the heat budget in the rift, as faster off-shelf water is forced to penetrate deeper into the western-most regions of the ice cavity. This water can therefore intrude within the rift environment along the east flank (2.6h), increasing the melt rate of deeper levels of the rift flanks and inhibiting freezing processes in shallower layers (Figure 2.6j-l).

This behavior explains why WE experiments at 10 cm s^{-1} result in a progressive decrease in freezing rate with rift widening. Forcing the model with a 10 cm s^{-1} flow flushing the cavity perpendicularly to the ice front allows the inflow to reach the inland-most section of the ice cavity, when compared to weaker forcing and/or the SN set of experiments. As the east flank of the rift gets progressively closer to the ice front as the rift widens, off-cavity water eventually intrudes into progressively larger rifts (with a consequent switch in the sign of the salt flux across the rift base, Figure 2.12) and inhibits freezing within. This behavior also explains why average basal melting increases with rift widening in the case of experiments WE under a strong 10 cm s^{-1} boundary flow, until the extreme case of WE under thermal forcing T5 with a

3 km rift in which the rift is dominated by slow melting (Figure 2.2). On the other hand, the rest of the experiments (majority) show the opposite trend, where the larger the rift the wider the area subjected to freezing, hence the faster the average freezing rate. We should note that our assumption that the rift widens only toward the east (hence closer to the ice front) may bias these results. This is because the proximity of the rift to the open ocean could potentially obscure the actual effects of rift widening by promoting enhanced interaction with off-shelf water.

2.4.4   Sub-shelf circulation

In this section, we address how sub-shelf circulation and ocean stratification are affected by the rift presence using modeled barotropic and overturning streamfunction together with the concentration of passive tracers `tr01` and `tr02` under the ice-shelf base.

Horizontal circulation

Our simulations show that horizontal ocean dynamics under intact ice shelves is governed by the intrusion of off-shelf water, which is partially blocked by the ice front. The ice-shelf front indeed represents a sharp discontinuity in the water column thickness that acts as if the topographic barrier extended along the entire water column (Taylor-Proudman theorem). This limits the amount of off-shelf water that enter the cavity, as it tends to flow along isobaths (parallel to the ice front by model design) in order to conserve potential vorticity.

The simulated water transport in the open ocean (not shown here) is almost 6 times stronger in the WE experiments when compared to the SN case, despite their prescribed velocity at the boundary being the same. As the former boundary condition is applied to the east boundary, the flux of water entering in the model domain is much larger than in the latter case. As a further consequence, water transport flowing in the open ocean penetrates much further in intact case forced with WE versus the case of SN (Figure 2.7a,e). This also explains the larger melt rates in the proximity of the ice front for WE currents, where the ice is directly in contact with water transport in the open ocean (Fig 2.4a,e).

In both SN and WE experiments, inner regions of the ice shelf cavity are dominated by a cyclonic gyre, centered in the north section of the model domain (yellow star). This cyclonic system is driven by off-shelf water masses at -1.5^{o}C that enters the cavity along the southern boundary (Figure 2.7i,m, Figure 2.13a,e). This intrusion also provides heat for melting the ice base (Figure 2.3), so off-shelf water reaches and melts the western-most extension of the ice shelf cavity. In turn, melting along the grounding line region drives the formation of buoyant meltwater (at around -1.9^{o}C), which flows northward along the ice shelf slope (Figure 2.13i,m) and returns toward the ice front along the northern edge, closing the circulation pattern.

In the case of a rifted ice shelf, the intrusion along the southern bound resembles intact experiments. Nevertheless, the intensity of mass and heat intrusion toward
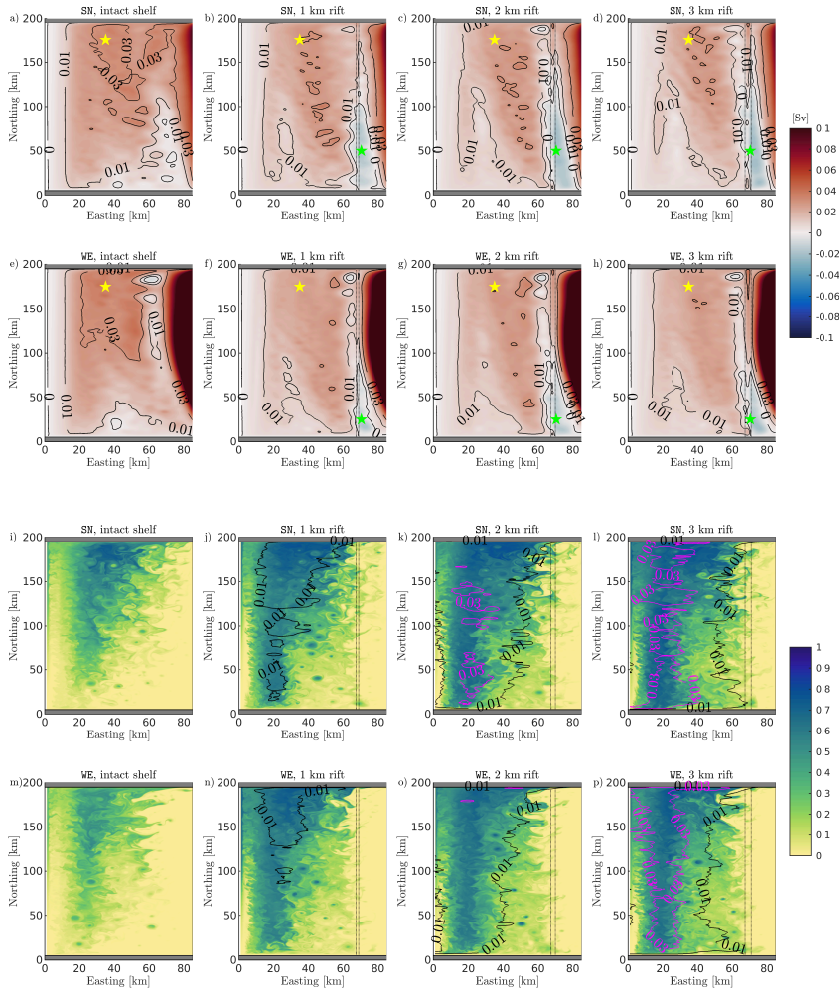
Figure 2.7: Comparison of barotropic streamfunction and horizontal concentration of passive tracers for experiments with different rift widths. First and third row (second and fourth row) correspond to SN (WE) boundary currents of 5 cm s⁻¹, respectively. The cold temperature profile T2 is used for all simulations. Dashed line is the rift location. Panels a-h compare the horizontal distribution of barotropic streamfunction (both color-map and contour lines). Positive means clockwise rotation and negative means counter-clockwise rotation. Locations marked with yellow and green stars are used to calculate intensity and center of the two gyres. Panels i-p compare snapshots of the horizontal concentration of passive tracers tr01 (background color-map) and tr02 (black and magenta contour lines corresponding to 0.01 and 0.03, respectively) at the grounding line level (255 m, cross-section *B* in Figure 2.1b) after 2 years from the initial release.

the grounding line is to a large extent curtailed. The inhibition is caused by the rift, that represents a second discontinuity in the water column thickness. In order to follow the contours of constant depth and conserve potential vorticity, the intrusive

water flow along the southern edge is deflected along the rift (Figure 2.7b-d and f-h). This is shown by the fact that regions with low values of `tr01` between 0 and 0.1 are confined seaward of the rift (Figure 2.7j-l and n-p) while, in the intact case, low `tr01` concentration is simulated as far as km 20 east. On the other hand, `tr02` - which tracks Rift Water formed from freezing processes in the rift - enters the cavity from the rift base and spreads along the ice-shelf base replacing off-shelf water. As a result, areas of the ice-shelf cavity eastward of the rift remains much cooler than in the intact case (Figure 2.13a-h), and melt rate here is therefore reduced.

Because the intrusion of off-shelf water is inhibited at the rift base, water transport westward of the rift is reduced as a consequence. The intensity of the cyclonic gyre progressively reduces by about 30 % in the case of a rifted shelf, with negligible difference between `SN` and `WE` experiments. Differently from the intact case, water transport from the open ocean along the southern boundary is separated from the cavity interior by the formation of the second gyre - anticyclonic and less intense - which is centered under the rift (green star, Figure 2.7b-d and f-h).

Rift width determines the strength of the individual gyres and to a lesser degree their dimension. While the cyclonic gyre decreases in strength as ocean transport in western-most region of the ice-shelf cavity is weaker, the model calculates a progressive growth in the anticyclonic gyre size with rift widening for both `SN` and `WE` sets of simulations, as the cavity remains colder (Figure 2.13b-d and f-h) and melt rate reduces.
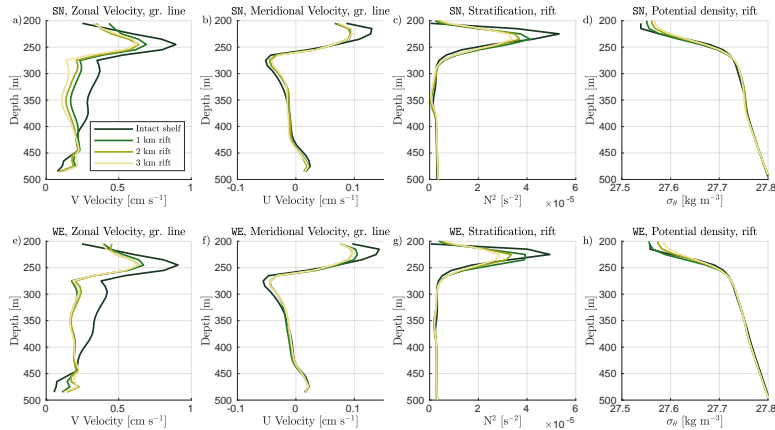

Figure 2.8: Comparison of vertical ocean profiles for experiments with different rift widths. Upper and lower panels correspond to `SN` and `WE` boundary currents of 5 cm s^{-1}, respectively. The cold temperature profile `T2` is used for all simulations. Vertical profiles of meridional and zonal velocities - as spatial average beneath the ice shelf slope (km 0 - 35 east, km 0 - 200 north) - are in panel a, b and e,f. Vertical profiles of buoyancy frequency squared N^2 and potential density anomaly ($\sigma_\theta = \rho_\theta - 1000$ kg m^{-3}, where ρ_θ is the local potential density) - as spatial average beneath the rift base (km 67.5 - 70.5 east, km 0 - 200 north) - are in panels c,d and g,h. Rift width is color-coded.

Overturning circulation

The calculated overturning streamfunction of intact experiments further shows that water transport under the ice base is to a large extent curtailed by the presence of the ice front (Figure 2.9). However, a fraction of off-shelf water enters the ice shelf cavity and the meridional on-shelf intrusion is strongest between 250 m and 300 m (Figure 2.8b,f). This intrusion drives the formation of a double overturning gyre system and delivers heat for melting the ice shelf in its deepest level, i.e. at the grounding line.

Simulations with the intact shelf shows a clockwise cell which is centered in the shallow portion of the ice cavity, just beneath the ice base (yellow stars). Underneath the clockwise cell, our simulations show a further overturning transport of less intensity through a counter-clockwise gyre cell (green stars), as water returns toward the ice front along the seabed (below 450 m, profiles in Figure 2.8b,f). Furthermore, the vertical ocean profile of intact experiments resembles a stably stratified ocean interior where fresh and light meltwater overlays denser water. The pycnocline - ocean layer where the density gradient is largest - is characterized by maximum stratification of $N^2 = 5 \times 10^{-5}\ s^{-2}$ calculated at a depth of 275 m (Figure 2.8c-g).

In shallow layers of the model domain, water flows eastward along at the ice base, while melting at the grounding line is responsible for the increase in the buoyancy of the ambient water. The formed meltwater rises along the ice-shelf slope (Figure 2.8b,f, 2.14) and is replaced by off-shelf water flowing toward the grounding line at depths, closing the shallow overturning circulation. Eventually, the upward flow of meltwater drops below the freezing point of seawater driving water freezing in the central region of the model domain (Figure 2.4).

In order to conserve potential vorticity, the intrusive water flow along the southern edge is deflected along the rift - which introduces an abrupt change in the isobath lines - and the off-shelf intrusion between 250 and 350 m is curtailed in response. As a consequence, our rifted simulations show that the clockwise gyre under the ice base in both SN and WE sets of experiments is 25% weaker than in the intact case while its connection with transport in the open ocean is interrupted at the rift base.

Our model simulates that low values of tr01 are confined to seaward of the rift when this is present while water layers immediately beneath the ice-shelf base are in contact with Rift Water (tr02). This water is formed after freezing in the ice rift and sinks due to decreased buoyancy. Sinking of Rift Water is also quantified by calculating the salt flux across the rift base (Figure 2.12). The downwelling of Rift Water leads to spreading of saltier and denser water in the shallower layers of the ice-shelf cavity (Figure 2.8d-h), weakening the sub-shelf stratification by up to 40 % (Figure 2.8c-g).

The impact of rift widening is particularly evident in the distribution of the two tracers. While larger rifts contain more tr02, the concentration of Rift Water along the ice base increases. In contrast, the on-shelf penetration of water from the open ocean, which has low values of tr01, is gradually reduced in the westernmost areas of the ice cavity as the rifts widens. While the density in the pycnocline increases, progressively stronger downwelling of Rift Water weakens the stratification under
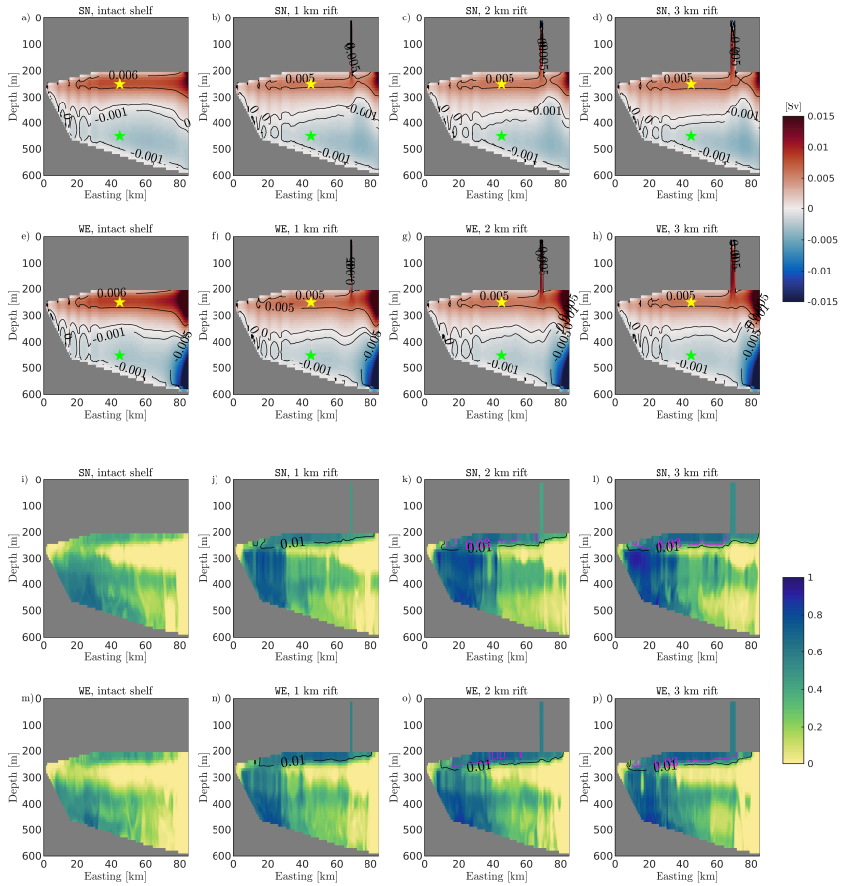
Figure 2.9: Comparison of overturning streamfunction and vertical concentration of passive tracers for experiments with different rift widths. First and third row (second and fourth row) correspond to SN (WE) boundary currents of 5 cm s^{-1}, respectively. The cold temperature profile T2 is used for all simulations. Panels a-h compare the vertical distribution of the overturning streamfunction (both color-map and contour lines). Positive means clockwise rotation and negative means counter-clockwise rotation. Locations marked with yellow and green stars are used to calculate intensity of the two overturning cells. Panels i-p compare snapshots of the vertical concentration of passive tracers tr01 (background color-map) and tr02 (black and magenta contour lines corresponding to 0.01 and 0.03, respectively) at the zonal cross-section along km 50 north (cross-section *A* in Figure 2.1a) after 2 years from the initial release.

the ice-shelf base, cools the ambient water near the ice base and curtails basal melt.

2.5   Summary and discussion

Ice rifts and their impact on the circulation below and around ice shelves are generally neglected in ocean models, as employed resolutions are often too coarse to resolve

km-wide fractures in the ice shelf. In this study, we use the MITgcm at high-resolution to show that the presence of a prominent rift near the ice-shelf front substantially alters the sub-shelf dynamics and the basal melt distribution. A schematic diagram of our findings is sketched in Figure 2.10.
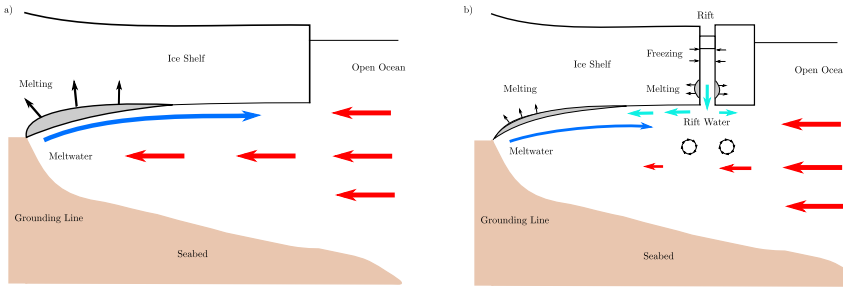

Figure 2.10: Schematic diagram of ocean dynamics underneath an intact ice shelf (a) and a rifted ice shelf (b), in our idealized model. The introduction of the rift interrupts the sub-shelf intrusion of inflowing water from the open ocean toward the grounding line, responsible for supplying heat for melting the ice base. As result, Rift Water floods the cavity from the rift base and basal melt is 20 % less than what is computed in the intact case, while the largest melt reduction occurs in the proximity of the grounding line.

Our idealized ocean model simulates that, under intact ice shelves, transport of off-cavity water is inhibited by the presence of the ice front. This acts as a discontinuity in the water column thickness and limits the amount of flow entrained into the ice cavity. Indeed the water tends to flow along isobaths (in this case parallel to the ice front by model design) in order to conserve potential vorticity. A fraction of open ocean water intrudes along the southern bound and provides the heat for melting the ice base. In turn, light meltwater formed from melting at the grounding line - i.e. the deepest layers of the idealized ice shelf - buoyantly rises along the ice draft toward the ice front, eventually dropping below the freezing point of seawater, as this decreases with depressurization. The sub-shelf circulation is closed as water returns toward the ice front along the northern edge (Figure 2.7a,e).

We find that the introduction of an ice rift affects sub-shelf dynamics and the distribution of basal melt by means of two processes. Firstly, the off-shelf water intrusion - which reaches and melts the grounding line - is further inhibited by the introduction of the rift. This acts as a second discontinuity in the water column thickness (Figure 2.9) after the ice front and leads off-shelf water to deviate along the rift (Figure 2.7). Secondly, in the case of a rifted ice shelf, off-shelf water intruding beneath the ice base is replaced by the outflow of dense Rift Water from inside the rift. This water is formed after seawater reaches the freezing temperature higher in the rift (Figure 2.6) causing it to salinify and sink. Modeled rift circulation is in good agreement with past numerical efforts (e.g. Khazendar and Jenkins, 2003) and the simulated overturning circulation resembles the "melt-driven" experiments of Jordan et al. (2014). Moreover, our simulations show that the downward flow of Rift Water

weakens the stratification of the water column by supplying denser water close to the ice base (Figure 2.8). As a consequence, the ambient water under rifted ice shelves is much cooler than in intact experiments (Figure 2.13a-h) and the basal melt rate and circulation strength are curtailed in response (Figure 2.4).

In perspective, the deflection of ocean currents along sharp discontinuities in the depth contour also occurs when the abrupt gradient is introduced at the bottom of the water column. For example, Menemenlis et al. (2007) showed that including a deep and narrow trench (the equivalent of a rift but extruded in the seabed) passing through the middle of Gibraltar Strait from the Atlantic Sea to the Mediterranean Sea substantially reduces the ocean current transport across the strait. In those experiments, ocean currents are deflected along the trench and in part dissipated by outflowing from inside the trench, similar to what happens in our simulations after the intrusive flow enters the ice shelf cavity and interacts with the rift.

Across the tested range of parameters, we quantify that - in rifted simulations - the heat transport toward the grounding line is 20 % weaker and the melt rate is 20 % lower than in the case of an intact ice shelf under the same dynamic and thermodynamic forcing scenario (Figure 2.2, 2.3). In particular, we estimate that melt rate in the proximity of the grounding line (i.e. the deepest layers of the ice shelf) represents the largest anomaly with a decrease of 30 % when the rift is present. This result showcases the potential of rifts formed near the ice front to impact the dynamics of the most vulnerable areas of ice shelves.

Our simulations indeed suggest that the impact of rifts in the sub-shelf circulation may have implications in the dynamics of the grounding line, whose migration is extremely sensitive to off-shelf water incursion (e.g. Seroussi et al., 2017). An accurate estimation of melt patterns at the grounding line is important as sustained melt in these vulnerable locations leads to further ungrounding of continental ice, which in turn accelerates ice discharge from outlet glaciers into the ocean (Rignot and Jacobs, 2002). Thanks to our high-resolution model, we have shown how off-shelf water intrusion may be modulated by the presence of an ice rift near the ice front and by the formation of Rift Water from freezing processes within the rift. Rift Water may mix with water masses flowing toward the grounding line possibly re-distributing heat under the ice base. Finally, our simulations also show that the rift presence tends to modulate heat intrusion regardless of whether currents in the open ocean are directed across or along the ice front. As a precise representation of the ice shelf cavity geometry is essential to correctly reproduce sub-shelf dynamics (Gold-berg et al., 2012; Schodlok et al., 2012), we posit that high-resolution ocean models should account for the presence of ice rifts in order to accurately reproduce heat intrusion under the ice shelf and the - yet largely unexplored - impact of rifts in the sub-shelf ocean dynamics.

It is worth noting that our idealized model setup has a limitation in that it does not account for sub-glacial discharge, the impact of which is only starting to be investigated under Antarctic ice shelves (Wei et al., 2020; Nakayama et al., 2021). Simulations that include freshwater flux at the grounding line have demonstrated an increase in basal melt in these critical areas, leading to an improvement in the mod-

eling of high melt rates observed under warm water ice shelves in the West Antarctic Ice Sheet. Further numerical efforts are required in order to evaluate the impact of sub-glacial discharge under cold water ice shelves as well as the interplay with the processes presented here.

Although our simulations introduce novel sub-shelf processes that have been neglected in past ice-ocean modeling efforts, our idealised model set-up cannot accurately quantify the effective importance of rifts in the sub-shelf dynamics of actual ice shelves. In particular, sea ice processes near the ice front are key components in mixing processes under and near the ice shelf. For example, dense High Salinity Shelf Water is formed by brine rejection during winter sea ice formation. Besides being an important contributor to the Meridional Overturning Circulation and the Antarctic Bottom Water (e.g. van Caspel et al., 2015), High Salinity Shelf Water convects down near the coast due to its buoyancy. These cold and dense water masses flow into deeper sections of the sub-ice cavity and alter the water at depth (e.g. Nicholls et al., 2009). These mixing processes are controlled by atmospheric forcing, with implications that go beyond the scope of our study. The inclusion of sea ice processes and their impact on water masses near the front of a rifted ice shelf in future numerical efforts is, therefore, necessary to accurately understand ocean dynamics and heat intrusion in the ice shelf cavity. This is particularly relevant where winter sea ice production is abundant (e.g. large ice shelves in the Weddell Sea). To this end, our work suggests that the downwelling of dense Rift Water may imply a further layer of complexity in the mixing processes near the ice front, and is therefore worthy of further investigation.

Furthermore, observations have shown frazil ice crystals which are suspended in buoyant plumes within the rift and adhere to the rift sidewalls and top in form of marine ice (Orheim et al., 1990; Lawrence et al., 2023). Meltwater that is adjacent to the ice base and the rift flanks can reach a supercooled state due to decompression, forming frazil ice crystals suspended in the water column. Jordan et al. (2014) estimates that the total freezing occurring inside a rift is mainly due to frazil ice accretion processes. Nevertheless, computational constraints and the vertical resolution employed here do not allow to resolve a) non-hydrostatic processes such as melt-driven plumes (Xu et al., 2012; Burchard et al., 2022) nor b) frazil ice crystals suspended within these plumes. These are caveats of our study as the entrainment into the plume determines the heat transferred to the ice and hence the melt rate (Vreugdenhil and Taylor, 2019). Similarly, frazil ice accretion impacts the stratification under the ice shelf and the buoyancy of such melt-driven plumes (Jenkins and Bombosh, 1995). For instance, suspended frazil ice crystals may enhance the buoyancy of the plume, leading to its acceleration and faster growth (Hewitt, 2020), but larger crystals precipitate more rapidly, reducing the buoyancy of melt-driven plumes. Future numerical efforts are required to constrain the role of non-hydrostatic processes within the rift and the impact of frazil ice formed in the rift on the stratification under the ice-shelf base.

Lastly, rifts growth is episodic, with events that last from minutes to hours, often followed by periods of inactivity that can range up to several months and years (Bassis

et al., 2005; Walker et al., 2015; Banwell et al., 2017). Rifts are often filled with ice mélange, whose rheological and mechanical properties are challenging to model (Vankova and Holland, 2017; Amundson et al., 2020). Although our simulations offer a highly simplified version of an ice rift - where atmospheric forcing and growth processes of encased ice mélange are neglected and rift width is fixed - they suggest that changes in rift size will cause a direct modulation of the amount of freezing between flanks (e.g. Figure 2.2,2.4). Hence, mechanically-induced rift propagation - altering rift size, e.g due to ice heterogeneity (Borstad et al., 2017) - may directly influence thinning/thickening of encased ice mélange thus the cohesiveness of rift flanks, besides being triggered by variation of rift infill due to environmental warming (Holland et al., 2009; Larour et al., 2021).

2.6   Conclusions

Our study shows that resolving km-wide rifts in the geometrical description of the ice-shelf cavity may imply a further layer of complexity in mixing processes below the ice base, with possible alteration of mass and heat intrusion. We estimate that these processes - so far largely unexplored - may alter ocean heat intrusion and melt rate by as much as 20 %. Notably, we calculate a significant 30 % decrease in melt at the grounding line in simulations with a rift. Given the crucial importance of basal ablation on the ice-shelf stability - in particular where the ice shelf becomes afloat - the processes presented here are worthy of further investigation. On a larger scale, a better understanding of heat pathways toward the grounding line remains a fundamental research avenue that would improve the estimation of ice-shelf ablation and, consequently, the evolution of the Antarctic Ice Sheet in a warming climate.

2.7   Open Research

MITgcm is an open-source numerical model, freely available on GitHub (Campin et al., 2020). All datasets and model outputs comprise 27 TB of data and are stored on the Lou mass storage system at the NASA Advanced Super-computing facility at Ames Research Center. Code and input data used to produce model output are freely available on GitHub and Zenodo (Poinelli, 2023).

2.8   Appendix A: Thermodynamic equations

2.8.1   Three-equations model

Ice-ocean processes are governed by the three-equation model (Hellmer and Olbers, 1989; Jenkins, 1991; Holland and Jenkins, 1999). Melting and freezing form an ice-ocean boundary layer which is implemented in MITgcm as a heat flux and a "virtual" salt flux (i.e. a freshwater flux q without volume change in the ocean) at the water cell immediately adjacent to the ice interface. In MITgcm, the ice-ocean interface can be horizontal (Losch, 2008) or vertical (Xu et al., 2012). Melting ($q < 0$) freshens the ambient water, while freezing ($q > 0$) leads to seawater salinification. The three-equation model can be written as heat (Equation 2.1) and salinity budgets (Equation 2.2) for the boundary layer, together with the linear dependency of the freezing point of seawater T_{fr} with pressure (Equation 2.3), in symbols:

$$c_p(\rho\gamma_T - q)(T_b - T) = -Lq - \rho c_{pI}\kappa\frac{T_I - T_b}{\Delta h} \tag{2.1}$$

$$(\rho\gamma_S - q)(S_b - S) = -S_b q \tag{2.2}$$

$$T_{\text{fr}} = (0.0901 - 0.0575 S_b) - 7.61 \times 10^{-4} p = T_b \tag{2.3}$$

where $c_p = 4000$ J kg^{-1} K^{-1} and $c_{p,I} = 2000$ J kg^{-1} K^{-1} are the specific heat capacity of seawater and ice, L=334000 J kg^{-1} is the latent heat of fusion, $\kappa = 1.54 \times 10^{-6}$ m^2 s^{-1} is the heat diffusivity through the ice, Δh is the ice shelf draft, ρ is the density of seawater, T_b, S_b are temperature and salinity at the boundary layer (water cell adjacent to the ice interface), T and S are local temperature and salinity, T_I=-20°C is the core temperature of the ice shelf and p is the local pressure.

The freshwater flux q can be translated into melt rate $\dot{m}$ using the density of ice ρ_I through $\dot{m} = -q/\rho_I$. As we arbitrarily set that $\dot{m} > 0, q < 0$ means melting and $\dot{m} < 0, q > 0$ means freezing, larger absolute values of $\dot{m}$ imply stronger melt or freeze rate, depending on the sign. In this study, the heat transfer coefficient γ_T is held constant at 10^{-4}, and the salinity transfer coefficient γ_S is a function of γ_T after the ISOMIP experiments of Losch (2008). By assuming that the temperature at the boundary layer T_b is equal to the freezing point of seawater (T_{fr}), equations A1-3 are numerically solved in MITgcm to obtain the triplet T_b, S_b, q which represents the boundary condition applied at the ice-ocean interface.

2.8.2   Heat transport toward the ice cavity interior

The heat transport HT across a meridional cross-section $x = x_1$ can be written as:

$$HT = c_p \iint \rho_\theta(x_1, y, z) u(x_1, y, z)[\theta(x_1, y, z) - T_{\text{fr}}]\mathrm{d}y\,\mathrm{d}z \tag{2.4}$$

where $\rho_\theta(x, y, z)$ is the local potential density, $u(x, y, z)$ is the local zonal velocity, $\theta(x, y, z)$ is the local potential temperature and T_{fr} is in-situ freezing point of sea-
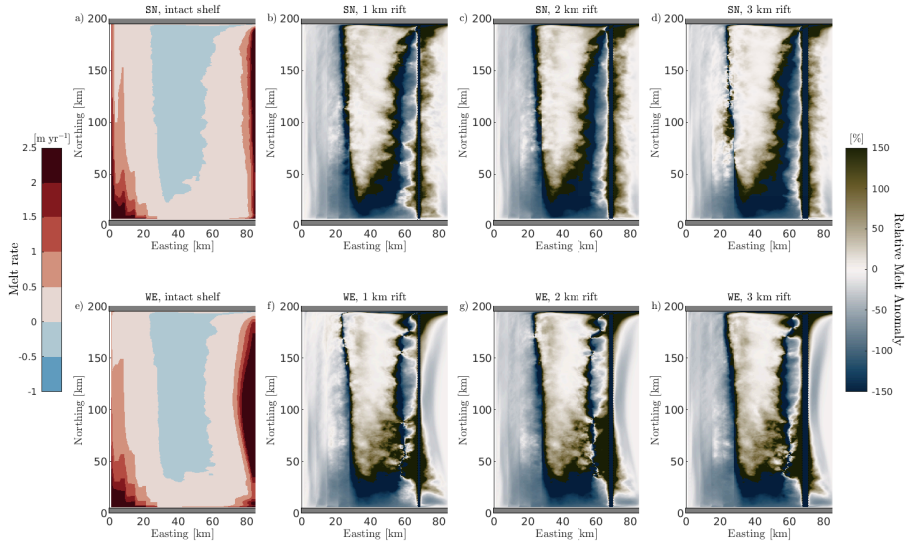
Figure 2.11: Comparison of horizontal distribution of ice-shelf basal melt rates for different rift widths. Upper and lower panels correspond to SN and WE boundary currents of 5 cm s^{-1}, respectively. The cold temperature profile T2 is used for all simulations. The first column shows the horizontal distribution of melt rate of intact experiments (a,e). Panels b-d and f-h show the horizontal distribution of relative melt anomaly, which is calculated as the difference between melt rate in the rifted shelf simulations with respect to intact cases under the same forcing conditions, which is then referenced to the results in the intact case. Left colorbar refers to melt rate, while right colorbar refers to relative melt anomaly. It is important to note that there are some areas of the ice shelf that experience a switch from melting to freezing, which in terms of relative value is quantified as more than 100 % alteration, even if the absolute change is fairly small.

water. Heat-maps of HT integrated across the ice front cross-section $x = 85$ km east for the 120 experiments are shown in Figure 2.3. Sensitivity of HT with respect to rift width, boundary current and thermal forcing matches the pattern shown in heat-maps of melt rate in Figure 2.2 and is discussed in Section 2.4.1.

2.9   Appendix B: Salt flux across the rift base

The salt flux Φ_S across the rift base at depth $z = z_r = 200$ m can be written as:

$$\Phi_S = \frac{1}{A_r} \iint w(x, y, z_r) S(x, y, z_r) \mathrm{d}x \mathrm{d}y \tag{2.5}$$

where A_r is the rift base area, $w(x, y, z)$ is the vertical velocity and $S(x,y,z)$ is the in-situ salinity. Heat-maps of Φ_S integrated across the rift base for the 120 experiments are shown in Figure 2.12.
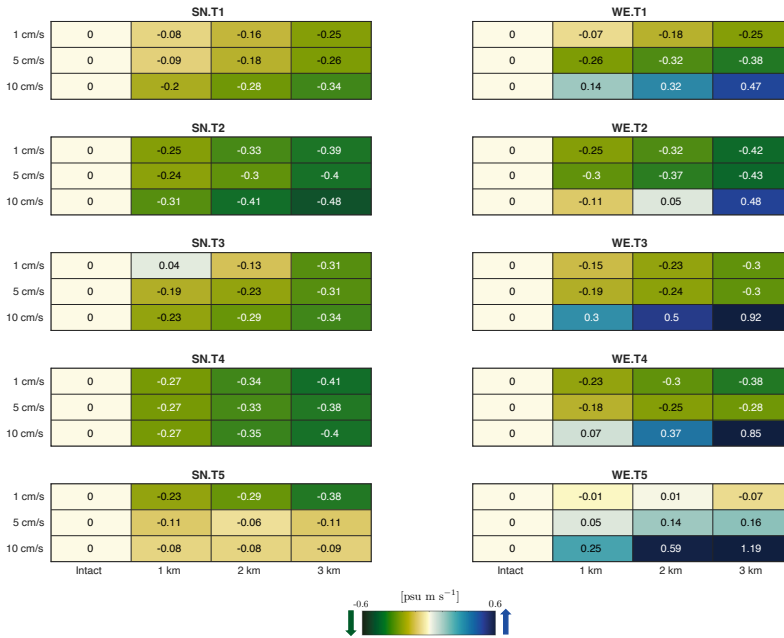
Figure 2.12: Heat-maps of total salt flux Φ_S across the rift base (200 m) for the 120 sensitivity experiments. Positive and negative values means upward and downward transport, respectively. Values are calculated with respect to temperature profile (panel), flow velocity (row) and rift width (column).

2.10   Appendix C: Ocean stratification

Ocean stratification can be calculated with the square of the Brunt-Väisäilä (buoyancy) frequency, which can be computed as the vertical buoyancy gradient:

$$N^2 = -\frac{g}{\rho_\theta}\left(\frac{\partial \rho_\theta}{\partial z}\right) \tag{2.6}$$

where ρ_θ is the local potential density and g is the gravitational acceleration. N^2 is a measure of the stability of a water column to convection/overturning. Positive values of N^2 indicate a stably stratified fluid where lighter water overlays denser water. A negative value of N^2 indicates an unstable water column where denser water is found above lighter water and convection/overturning processes increase.

2.11   Appendix D: Caption for Animation 1

The supporting animation shows the 2-year evolution of passive tracer tr01 distribution at the grounding line depth, 255 m, in cross section B in Fig. 1b. The supplement related to this article is available online at: https://doi.org/10.5194/tc-17-2261-2023-supplement.
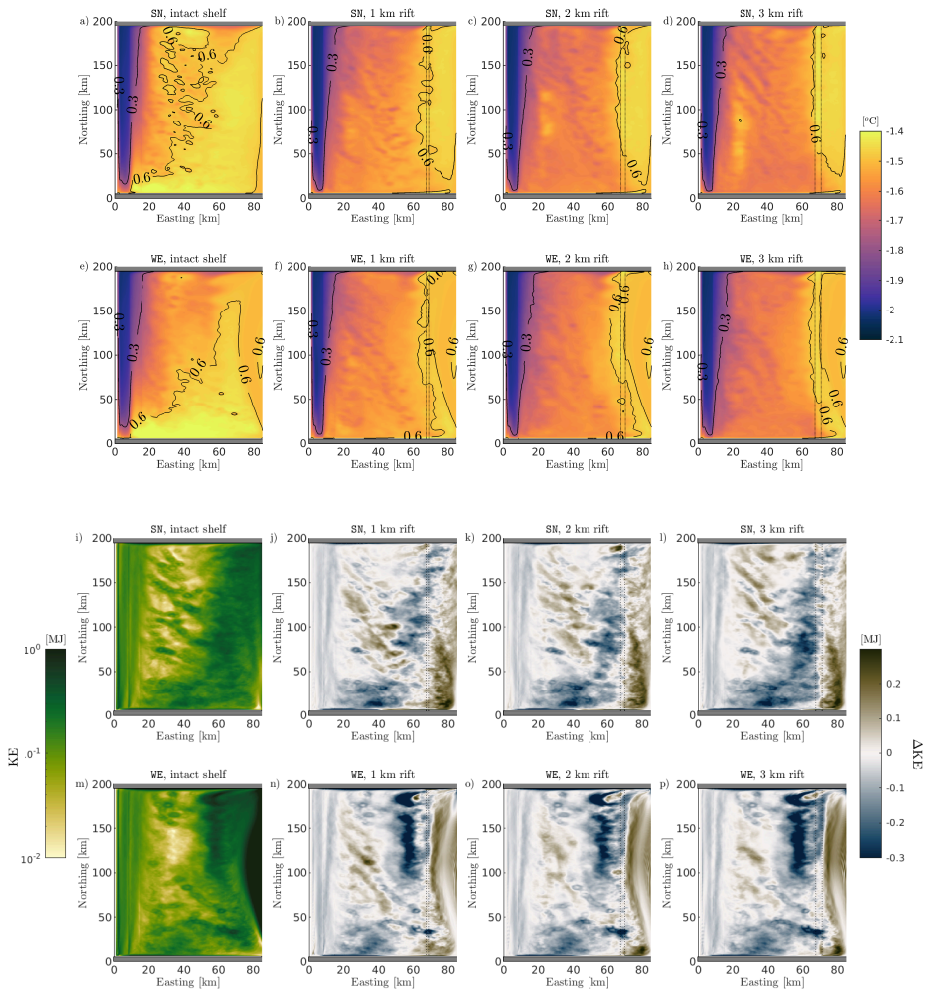
Figure 2.13: Comparison of horizontal distribution of potential temperature and kinetic energy (KE) for different rift widths at the grounding line level (255 m, cross-section *B* in Figure 2.1b). First and third row (second and fourth row) correspond to SN (WE) boundary currents of 5 cm s^{-1}, respectively. The cold temperature profile T2 is used for all simulations. Dashed line is the rift location. Panels a-h compare the horizontal distribution of potential temperature (color-map) and the difference between in-situ potential temperature and the freezing point of seawater (black contour lines). Panels i-p compare the kinetic energy. The first column shows the horizontal distribution of kinetic of intact experiments (i,m). Panels j-l and n-p show the horizontal distribution of kinetic energy anomaly, which is calculated as the difference between kinetic energy at 255 m in the rifted shelf simulations with respect to intact cases under the same forcing conditions. Left colorbar refers to kinetic energy, while right colorbar refers to kinetic energy anomaly.
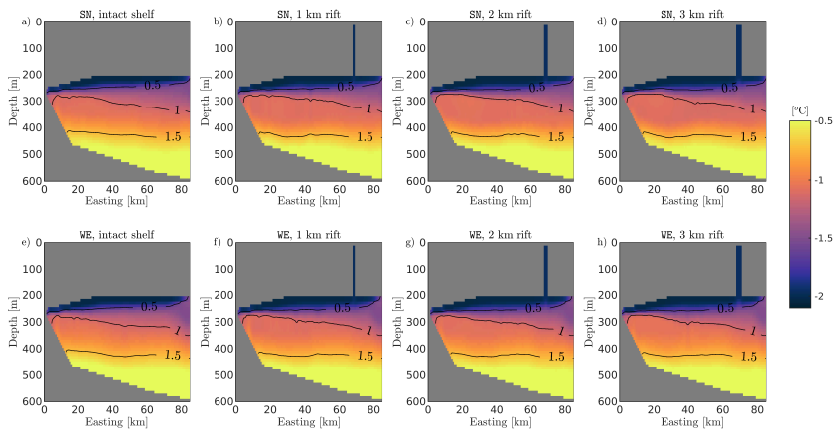
Figure 2.14: Comparison of vertical distribution of potential temperature (color-map) and the difference between in-situ potential temperature and the freezing point of seawater (black contour lines) for experiments with different rift widths at the zonal cross-section along km 50 north. Note that the values in the colorbar values is different than Figure 2.13a-h. First and third row correspond to SN (WE) boundary currents of 5 cm s^{-1}, respectively. The cold temperature profile T2 is used for all simulations

Chapter 3

Ocean dynamics under the Larsen C Ice Shelf

> Difficulties are just things to overcome, after all.
>
> — Ernest Shackleton

3.1 Summary

Iceberg A-68 separated from the Larsen C Ice Shelf in July 2017 and the impact of this event on ocean heat delivery beneath the ice has yet to be assessed. To understand this process, we conduct numerical simulations of ocean dynamics near and below the ice shelf pre- and post-calving. Our results agree with available observations and indicate that basal melt is primarily driven by the incursion along the seabed of High Salinity Shelf Water, formed during wintertime sea-ice production. After the calving event, our simulations show enhanced ocean heat delivery and doubling of the melt rate under Gipps Ice Rise. Ice thinning in this region - critical for ice dynamics - suggests a positive feedback that could destabilize the ice shelf. Further investigation of the impact of ice-front retreat on the heat delivery under the ice is crucial to better understand ice-shelf dynamics in a warming environment.

3.1   Introduction

Most ice shelves in the eastern Antarctic peninsula have either retreated significantly or disintegrated over the past few decades (Cook and Vaughan, 2010). The consequent loss of buttressing force led to up to an eight-fold increase in freshwater discharge from glaciers north of the Larsen C Ice Shelf (Rignot et al., 2004; Scambos et al., 2004), with an estimated sea level rise equivalent of approximately 0.6 mm since 1979 (Rignot et al., 2019). In July 2017, Larsen C calved one of the largest icebergs ever recorded: A-68. This event did not completely destabilize the ice shelf (Fürst et al., 2016) but it brought the ice front into its inland-most position observed so far. With further calving, the ice front may recede beyond the compressive arch, a mechanical threshold that could lead to irreversible retreat (Doake et al., 1998). Processes driving ice-front retreat require further understanding as the consequences of climate warming become more evident.

After ice-shelf retreat events, the temporary front location is often pinned by ice rises, rumples, islands, and shallow bathymetric features that buttress the ice flow (Thomas, 1979). Past studies suggest that ocean-induced ablation of thin ice around such critical pinning points is important for the ice-shelf stability. For the Larsen C Ice Shelf, basal melting nearby pinning points such as the Gipps and the Bawden Ice Rises (GIR, BIR, Figure 3.1) is thought to reactivate local rifts (Holland et al., 2009; Borstad et al., 2013; Kulessa et al., 2014; Larour et al., 2021), potentially leading to calving events such as the one in 2017. However, pathways of ocean heat intrusion under Larsen C during and after the calving of iceberg A-68, along with the impact on basal melting around local pinning points, remain poorly constrained. Long-term *in-situ* data are indeed sparse as persistent sea-ice makes these locations particularly inaccessible.

The current understanding of ocean circulation beneath and in front of Larsen C and the delivery of heat under the ice base revolves around the few available *in-situ* observations. Two expeditions in February 2002 and March 2019 (Nicholls et al., 2004; Hutchinson et al., 2020) detected warm (-1.5^{o}C) modified Warm Deep Water (mWDW) near BIR. This is a derivative of Circumpolar Deep Water, the warmest water mass circulating around Antarctica. During the summer, mWDW reaches the area and mixes with High Salinity Shelf Water (HSSW), which forms at the ocean surface during strong winter sea-ice production. The resulting water mass§ after heat from mWDW is redistributed via local mixing with cooler shelf waters (Hutchinson et al., 2020) - intrudes into the Larsen C ice cavity and flows toward the grounding line along the Kenyon peninsula (Holland et al., 2009; Mueller et al., 2012; Harrison et al., 2022). Data from holes drilled near the grounding line (yellow stars, Figure 3.1) in December 2011 showed that sampled water was at the local freezing point (-1.9^{o}C), which excludes direct below intrusion of a "pure" (hence warmer) version of mWDW (Nicholls et al., 2012). As a consequence, the average basal melt near the grounding line is relatively low, i.e. approximately 0.7 m yr^{-1} (Davis and Nicholls, 2019).

It is unknown if and how the calving of iceberg A-68 affected these sub-shelf
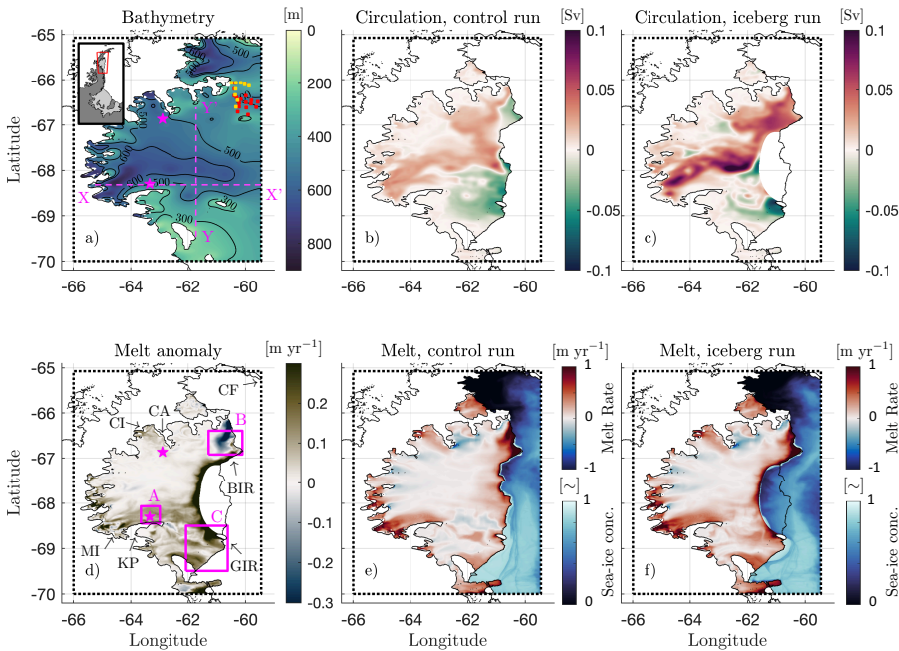
Figure 3.1: Model domain (dotted black box), integrated barotropic streamfunction, melt rate and sea-ice concentration. Magenta stars are the locations of drill sites after Nicholls et al. (2012). Yellow and red squares are locations of CTD observations after Nicholls et al. (2004) and Hutchinson et al. (2020), respectively. a) Bathymetry, both background colormap and contour lines. Magenta dashed lines are vertical cross-sections X-X' and Y-Y'. b) Barotropic streamfunction in Sverdrup (Sv), control run. c) Barotropic streamfunction, iceberg run. d) Integrated melt anomaly as difference between integrated melt rate for iceberg (f) and control (e) runs. Melt patterns are calculated as temporal average between January 1st, 2015 and January 1st, 2017. Magenta boxes A, B and C are key locations investigated in this paper, covering the survey area of Nicholls et al. (2012), and the shallow areas that coincide with the Bawden and Gipps Rises, respectively. f) and e) also include monthly average of sea-ice concentration at the end of summer (March 2016), i.e. when its concentration is the lowest. BIR: Bawden Ice Rise, GIR: Gipps Ice Rise, CA: Cape Alexander, CF: Cape Fairweather, CI: Cabinet inlet, KP: Kenyon peninsula, MI: Mobiloil inlet.

circulation patterns. The impact of ice-front retreat and ice rifts on the dynamics of Antarctic ice shelves is only beginning to be explored (Bradley et al., 2022; Yoon et al., 2022; Poinelli et al., 2023b). In this work, we use a regional ocean simulation of the Larsen C ice cavity to study sub-shelf ocean circulation and its effects on basal melt rates. We then investigate the impact of ice-front retreat on pathways of heat intrusions under the ice.

3.2   Methodology

3.2.1   Ocean model

We use the Massachusetts Institute of Technology General Circulation Model (MIT-gcm) with thermodynamic ice shelf and dynamic/thermodynamic sea-ice (Losch, 2008; Losch et al., 2010). Basal ice-shelf melt is computed using the three-equation model (Hellmer and Olbers, 1989; Jenkins, 1991; Holland and Jenkins, 1999). Ocean, sea-ice, and ice-shelf parameters are nearly identical to those used by Nakayama et al. (2019). Differently, we calculate here coefficients of heat and salt transfer using drag laws and friction velocities based on a momentum-flux-derived drag coefficient $C_d = 0.0022$, which was obtained from *in-situ* observations (Davis and Nicholls, 2019). Bed topography (Figure 3.1a) and ice-shelf geometry (Figure 3.1b,c) are interpolated from the state-of-the-art compilation BedMachine-V3 (Morlighem et al., 2020). Nominal horizontal and vertical grid spacing are set to 500 m and 10 m, respectively, which constrain the step size of integration time to 30 s.

Boundary conditions are applied at the eastern and southern domain boundaries. Summertime (December-March) boundary conditions of potential temperature and salinity (θ-S) are derived from available conductivity-temperature-depth (CTD) observations from the expedition of 2019 (Figure 3.5)(Hutchinson et al., 2020). Wintertime (April-November) temperatures at the domain boundaries are held constant at -1.9^{o}C. We also apply tidal forcing as Dirichlet boundary conditions. Tidal amplitudes and phases are obtained from the data-assimilative barotropic tidal model of Padman et al. (2002). Realistic monthly-averaged surface forcing is interpolated on the model domain from numerically-analysed atmospheric data from the ERA5 land reanalysis (Hersbach et al., 2020). Sea-ice concentration and thickness along eastern and southern boundaries are interpolated from the coarse resolution global state estimate ECCO-LLC270 optimization (Zhang et al., 2018). Due to computational constraints, sea-ice velocities at the boundaries are directly calculated by surface fluxes forcing in the interior.

3.2.2   Experiments

We conduct two experiments, both starting on January 1st, 2015. Firstly, we simulate ocean dynamics using the ice-shelf coastline prior to the calving of iceberg A-68 in 2017 (control run, Figure 3.1b). Secondly, we run an experiment in which iceberg A-68 is removed from the ice-shelf geometry (iceberg run, Figure 3.1c). Both simulations spin up for a period of 5 years under identical atmospheric and boundary forcing. The following analysis refers to model output between January 1st, 2015 and January 1st, 2017.

To investigate differences in sub-shelf circulation in the two experiments, we release two passive tracers on January 1st, 2015, following the approach of Nakayama et al. (2017). Tracer `tr01` is restored to a unity value at the ocean surface as a proxy for HSSW concentration, with restoring time scale of one hour. A second tracer is

released at the ice-shelf base at the same rate as melting occurs in order to track meltwater fraction (MWF).

3.3   Results

Model results of the control run are discussed in section 3.1 and a comparison with available observations is in section 3.2. Results of the iceberg experiment are in section 3.3.

3.3.1   Ocean circulation prior to the calving of iceberg A-68

The control run simulates ocean conditions before the calving of iceberg A-68 (Figures 3.1e, 3.2a-c, 3.3a-d). High sea-ice production is simulated near the ice front (Figures S2), with peaks during the austral winter season between March and October. As a result of loss of buoyancy in response to brine rejection from sea-ice formation, tracer `tr01` (as proxy for HSSW) convects to deeper layers and follows bathymetric contours into the ice cavity. The tracer is transported toward the grounding line and reaches the western-most extensions of the ice-shelf cavity at the end of the second winter season.

Tracer `tr01` flows westward through three distinct pathways (red arrows in Figure 3.2a). The most intense intrusion occurs around latitude 68^oS and along the "southern trough" (a bathymetric feature documented in Brisbourne et al., 2020). Along this pathway, `tr01` sinks to the seabed in the open ocean and drains into the deep trough toward the Mobiloil inlet. At these latitudes, the relatively thick water column facilitates the below intrusion along and below isopycnal level 27.90. Second and third pathways occur around the two pinning points. Near GIR, ocean currents interact with thin ice, and the relatively flat and shallow seabed favors intrusion of `tr01`. Water that eventually enters the cavity wraps around the Kenyon Peninsula and drains deeper into the Mobiloil inlet. Similarly, `tr01` enters the cavity following the shallow and relatively flat seabed near BIR. This water wraps around Cape Alexander and sinks toward the Cabinet inlet.

The seasonal variability of sea-ice (Figure 3.4a-b) and the consequent formation of HSSW determine a different circulation between summertime and wintertime, as it can be seen from `tr01` and heat intrusions (formulas are included in the Supporting Information). The intrusion of `tr01` into the cavity occurs in pulses (Figure 3.4c). During the first summer months, the model simulates sea-ice melting with the consequent freshening of surface water and `tr01` being confined in the mixed layer above 100 m. With the beginning of the first winter (March 2015), sea-ice production increases. Cumulative below-shelf intrusion of `tr01` accelerates in June 2015, stabilizes at the end of the first winter season, and remains constant throughout the summer. With the beginning of the second winter (March 2016), `tr01` intrusion accelerates again and at the end of 2016 the cumulative below-shelf `tr01` volume is twice as much as at the end of 2015. Our model estimates that each year, the total heat intrusion toward the grounding line is ∼550 TW (Figure 3.4d).
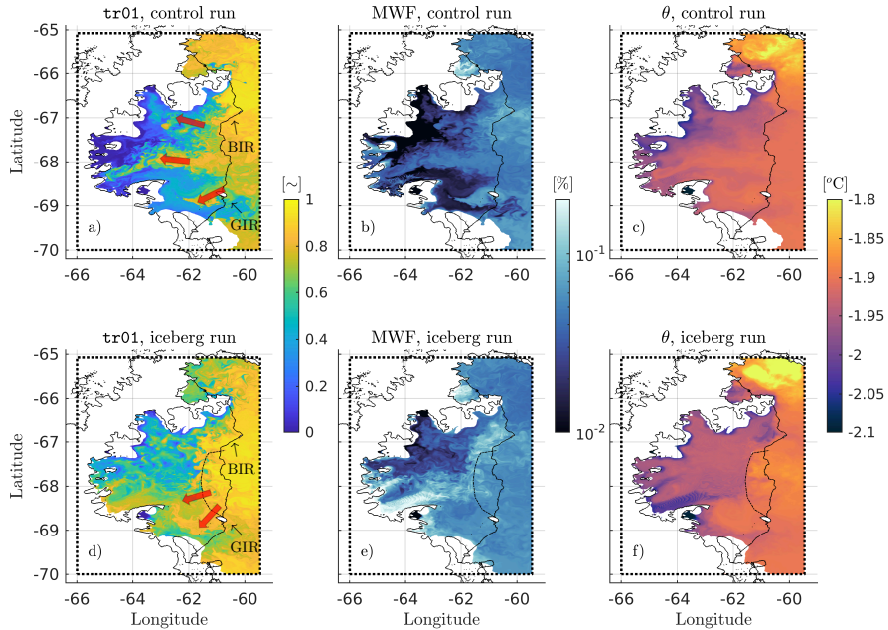
Figure 3.2: Simulated ocean conditions along the horizontal cross-section corresponding to isopycnal surface 27.90. a) Concentration of passive tracer `tr01` as a snapshot of January 1st, 2017. Red arrows show direction of the pathways of `tr01` intrusion. b) Distribution of meltwater fraction (MWF) calculated on the same day. c) Distribution of potential temperature as an average for December 2016. d-f) are same as a-c) but for the iceberg run.

The intrusion of HSSW drives melting when this saline water interacts with the base of the ice shelf (Figure 3.1e, 3.2a). HSSW carries sufficient heat to melt ice as the freezing point decreases with increasing pressure. We find that the thermal driving pattern matches well the spatial distribution of melt rate, while changes in ocean speed alone cannot explain the simulated melt pattern at the grounding line (Figure 3.10). The model simulates three peaks of meltwater (Figure 3.2b) that correspond to the three intrusive pathways. The most significant peak, with MWF around ∼0.1%, is found north of the Kenyon Peninsula (box A). Meltwater then flows north-northeast along the ice draft toward shallower layers and exits the cavity between latitude 68°S and 67°S. Other sources of meltwater are the GIR and BIR (boxes B and C), where the MWF is twice as high as in box A. Seasonal variability of melt rates in box A (Figure 3.4e-f) further shows a large correlation (R=0.84) with thermal driving (similar trends found under BIR and GIR, Figure 3.11), suggesting a stronger control of ocean temperature on ice-shelf melting rather than ocean flow speed (R=0.42).
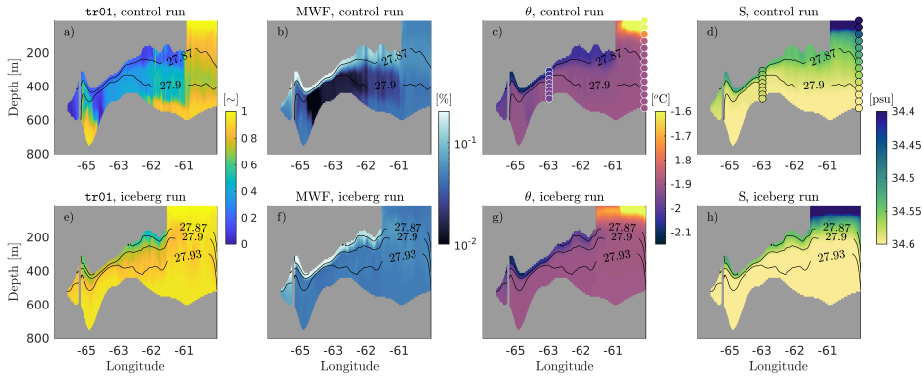
Figure 3.3: Simulated ocean conditions along vertical cross-sections XX', that is aligned with the latitude of the south drill site. Black contour lines are isopycnal levels. a, b) Concentration of passive tracer `tr01` and meltwater fraction (MWF), respectively, as a snapshot for January 1st 2017 in the control run. c, d) Distribution of potential temperature and salinity in the control run as a monthly average for December 2016. Dotted markers are observation profiles of potential temperature (c) and salinity (d) after CTD data of (Nicholls et al., 2012) (under the ice base) and (Hutchinson et al., 2020) (open ocean). e-h) are same as a-d) but for the iceberg run.

3.3.2 Model-data comparison

Simulated vertical profiles of potential temperature and salinity under the ice of the control run match well CTD observations (Figures 3.3c-d, 3.5,3.10) accessed through the two drill sites in December 2011 (Nicholls et al., 2012). The model reproduces a layer of cold and fresh meltwater beneath the ice base around the local freezing temperature and salinity around 34.5 psu. Meltwater sits above denser and relatively warmer HSSW characterized by potential temperature around -1.9^{o}C and salinity reaching 34.65 psu. The modeled thermocline at the south drill site is slightly shallower and steeper than *in-situ* data. The halocline is also slightly steeper than observations, with simulated salinity beneath 400 m being lower than observations. At the north drill site, the simulated ocean temperature at the bedrock is slightly colder and the salinity profile is fresher than available data.

To compare modeled and observed current speed at the base of the ice shelf we use a frequency decomposition (Figure 3.13). The modeled spectrum shows good agreement with *in-situ* data acquired by a Nobska Modular Acoustic Velocity Sensor at the southern drill site during the field campaign of 2011 (Davis and Nicholls, 2019). Our model reproduces well diurnal and semi-diurnal components, which dominate the sub-shelf dynamics, despite underestimating the observation-derived power spectra between 1 and 0.1 cycles per day by up to 40%.

Temporal evolution of sea-ice concentration in front of Larsen C shows a strong seasonal signal, with peak concentration of 96% between August and November 2015 (Figure 3.4a). Overall, the model results for 2015 are in fairly good agree-

ment (R=0.82) with average sea-ice concentration in the Weddell Sea obtained via DMSP SSM/I-SSMIS passive microwave data (DiGirolamo et al., 2022). We underestimate sea-ice concentration by 20% in April and March 2015. Similarly, sea-ice concentration in 2016 is underestimated by 30%. The mismatch between satellite observations and modeled output can be due to multiple factors. For example, simulated sea-ice velocities at the boundaries are directly computed by forcing in the interior. As so, transport of sea-ice from southern latitudes onto the continental shelf near Larsen C are here neglected.

Simulated melt rate of the entire Larsen C Ice Shelf as an average between the two years of simulations is 0.11 m yr^{-1}. Average melt rate at the southern drill site (box A) is 0.18 m yr^{-1} and, in the proximity of BIR and GIR (box B and C), it reaches 0.46 and 0.11 m yr^{-1}, respectively. The total ice-shelf melt rate average is in good agreement with 0.17 m yr^{-1}, estimated with altimetry observations spanning the same period (Adusumilli et al., 2018). At box A, *in-situ* data (0.70 m yr^{-1}, Davis and Nicholls, 2019) and altimetry-derived measurements (0.36 m yr^{-1}, Adusumilli et al., 2018) are underestimated by the model. At boxes B and C, calculated melt is in reasonable alignment with altimetry-derived estimates near the two pinning points (1.11 and 0.36 m yr^{-1}, respectively).

3.3.3   Ocean circulation after the calving of iceberg A-68

The iceberg run simulates ocean conditions after the calving of iceberg A-68 (Figures 3.1, 3.2d-f, 3.3e-h). The removal of iceberg A-68 from the ice-shelf geometry substantially alters the pathways through which ocean water intrudes and distributes heat beneath the ice by means of two processes. Firstly, the retreat event results in the ice front migrating westward. This leads to polynya near the ice shelf also in the southern section of the model domain, while, in the control run, sea-ice presence in this area was more stable. Secondly, the removal of a substantial portion of ice, combined with the deeper bathymetry, increases the thickness of the water column along the new ice front with respect to the pre-calving conditions.

The aforementioned processes result in a two-fold effect. (a) An enhanced HSSW production along the new margin, which is a direct results of an increase in the number of polynya days during the two years of simulations. (b) A thicker water column along the ice front, which weakens the potential vorticity barrier caused by the ice shelf. As a consequence, these processes favor a widespread and more intense below intrusion of `tr01` with respect to the control run.

In the iceberg run, there are notable changes in the sinking behavior of `tr01` and the intrusion pattern along the southern trough compared to the control run. Instead of sinking primarily along the southern trough as observed in the latter, `tr01` sinks along the entire western edge of iceberg A-68 in the former. This sinking and intrusion are most pronounced south of latitude 67°S (Figure 3.2d), aligning with the new peaks of sea-ice production in the southern section of the model domain as well as the thicker water column along the ice front in the south. As a consequence, the overall intrusion of `tr01` below GIR is much stronger in the iceberg run, and the tracer
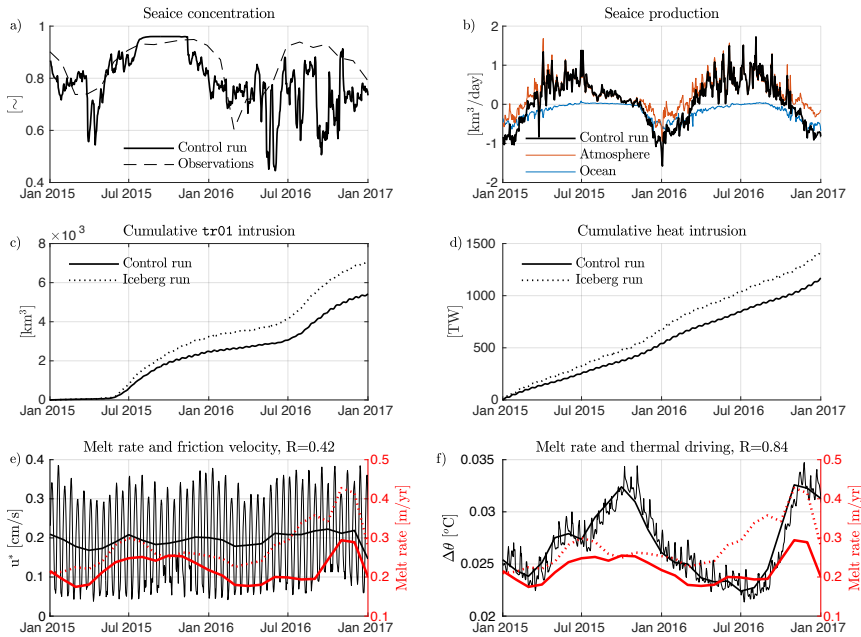
Figure 3.4: Time series of simulated results and observation-based reconstructions. a, b) Temporal evolution of sea-ice concentration and sea-ice production in the control run; the latter with decomposition of the production source: ocean-induced ablation and atmosphere-induced accretion. Dashed line in a) is the average concentration of sea-ice in the Weddell Sea derived via DMSP SSM/I-SSMIS passive microwave data. c, d) Temporal evolution of tracer `tr01` and heat cumulative intrusion for control and iceberg run. e, f) Temporal evolution of ocean speed and thermal driving at the ice base in box A. These values are calculated with daily (thin black line) and monthly (thick black line) model outputs. Red lines are modeled melt rate for control (solid line) and iceberg (dotted line) runs as average below box A.

reaches the western-most extensions of the ice-shelf cavity near the Mobiloil inlet after only a single winter season since the initial release (Supporting Animation).

Similar to the control run, the intrusion of HSSW occurs in pulses. `tr01` intrusion accelerates at the beginning of each winter season and stabilizes during the summer months when the model simulate sea-ice melting. However, in comparison to the control run, the iceberg run shows that the total below intrusion of `tr01` increases by 50% while heat transport toward the grounding line increases by 30% (Figure 3.4c,d), due to the processes explained above. Consequently, the total integrated melt rate is 73% higher in the iceberg run, while the largest increase is concentrated south of latitude 68^oS (Figure 3.11, 3.12). In particular, basal melt below GIR (calculated over box C) increases by 113% and the area north of Kenyon Peninsula, in the proximity of the south drill site (calculated over box A) experiences a 54% increase. In contrast, basal melt around BIR (calculated over box B) decreases by 12%. While the basal melt increase south of latitude 68^oS is a direct result of a stronger HSSW intrusion after ice-front retreat, the decrease of melt under BIR is a consequence of an

enhanced northward flow of meltwater from the Mobiloil inlet. In comparison to the control run, meltwater flows more northward and along the new ice front and cools the ambient water under the ice in the proximity of BIR (Figure 3.2e,f), curtailing local melt.

3.4   Discussion

Past studies delineated two future scenarios that would destabilize the Larsen C Ice Shelf and precondition its collapse (e.g. Doake et al., 1998; Jansen et al., 2013; Holland et al., 2015): a) ungrounding of ice near BIR and GIR pinning points and b) ice-front retreat beyond the compressive arch. Our simulations suggest that the calving event of 2017 may have redistributed ocean heat delivery under the ice base with an estimated doubling of basal melt around GIR. This is particularly important as sustained thinning in this area has a two-fold effect. Firstly, it may lead to ungrounding the ice shelf from the shallow bathymetry (a), with the consequence of acceleration of the ice flow (Borstad et al., 2013). Secondly, it may re-activate dormant rifts (Holland et al., 2009; Larour et al., 2021), which could then lead to further ice-front retreat (b), such as the one of 2017. This positive feedback for ice-shelf destabilization after the calving of A-68 is worthy of further investigation.

Our results build understanding on the need to consider updated ice-shelf margin geometry to accurately project ocean circulation below the ice. Recent studies have demonstrated that ice-front retreat can have significant implications for the intrusion of warm Circumpolar Deep Water into the Pine Island Glacier cavity in the Amundsen Sea (Bradley et al., 2022; Yoon et al., 2022). In this study, we show that calving events can also impact the mechanisms of HSSW intrusion under cold water ice-shelves, which is the dominant driver of their basal ablation (Nicholls et al., 2009). It is important to note that, rather than the physical retreat of the ice front, it is the overall hydrography of the post-calving condition that plays a crucial role in delivering heat towards the grounding line. For instance, the presence of bathymetric ridges and the ice-front retreat beyond their location determine the actual extent of below-shelf water intrusion.

A limitation of our simulations is the lack of large-scale ocean circulation in the Weddell Sea, as our lateral ocean boundary conditions are only based on barotropic tidal forcing. For example, our model is unable to account for the presence of relatively warm mWDW documented near BIR (Nicholls et al., 2004; Hutchinson et al., 2020), which could substantially increase basal melt. Furthermore, we do not consider the impact of frazil ice crystals, which accumulate under under Antarctic ice shelves and form marine ice bodies. Under Larsen C, the thickness of marine ice is estimated to be up to a third to half of the ice-shelf depth (Holland et al., 2009; McGrath et al., 2014), in agreement with numerical models (Harrison et al., 2022). The role of frazil accretion in the formation of such thick layers of marine ice is well documented for the ice flow (Jansen et al., 2013; Kulessa et al., 2014), but the impact of accreted ice on the below heat intrusion is not fully understood. Further numerical simulations need to take into account realistic ocean forcing and to investigate its

impact on frazil ice accretion under cold-water ice-shelves such as Larsen C, where marine ice is thought to be abundant.

Finally, in our simulations we find that ocean temperature has a stronger impact on ice-shelf melting compared to ocean speed. As a response to ongoing and future climate change, warm water could be transported progressively closer to cold water ice shelves in the Weddell Sea (Hellmer et al., 2012; Darelius et al., 2016), most likely in the form of mWDW, which could intrude under the ice and increase their basal melt. Despite the fact that there is no evidence of direct intrusion of mWDW under the Larsen C Ice Shelf as of December 2011, our simulations highlight the need for further observations and modeling efforts to monitor arrival and impact of warm coastal currents underneath this ice shelf.

3.5   Conclusions

We present a high-resolution ocean simulation nearby and below the Larsen C Ice Shelf before and after the calving of iceberg A-68. The pre-calving run is in agreement with *in-situ* and remote observations and simulates realistic pathways of ocean heat intrusion towards the grounding line. Basal melt is primarily driven by the topographically-driven incursion of High Salinity Shelf Water formed at the surface during wintertime sea-ice growth. Results from the post-calving run suggest that the removal of iceberg A-68 yields enhanced ocean heat intrusion and melting in the southern section of the domain. In particular, the calving event causes basal melt below the Gipps Ice Rise to double. As enhanced thinning of this pinning point can lead to further calving - which then can compromise the ice-shelf mechanical stability - our results highlight a positive feedback for ice-shelf destabilization.

3.6   Open Research

MITgcm is an open-source numerical model, freely available on GitHub (Campin et al., 2020). All datasets and model outputs comprise 8 TB of data and are stored on the Lou mass storage system at the NASA Advanced Super-computing facility at Ames Research Center.

3.7   Appendix A: Heat and `tr01` intrusion

The intrusion I of passive tracer `tr01` into the ice cavity is quantified with the following equation:

$$I_{\texttt{tr01}} = \int\int\int \mu(x,y,z)\mathrm{d}x\mathrm{d}y\mathrm{d}z \tag{3.1}$$

where $\mu(x,y,z)$ is the concentration of `tr01` under the ice base, x is longitude, y is latitude and z is depth. On the other hand, the heat transport HT across the meridional cross-section YY' (longitude fixed at $x = x_1$) can be written as:

$$HT = c_p \int\int \rho_\theta(x_1,y,z)u(x_1,y,z)[\theta(x_1,y,z) - T_f]\mathrm{d}y\mathrm{d}z \tag{3.2}$$

where c_p=4000 J kg^{-1} K^{-1} is the specific heat capacity of seawater,$\rho_\theta(x,y,z)$ is the local potential density, $u(x,y,z)$ is the local zonal velocity, $\theta(x,y,z)$ is the local potential temperature and $T_f = -2.1^o$C is the *in-situ* freezing point of seawater at the ice base (roughly at 300 m depth).

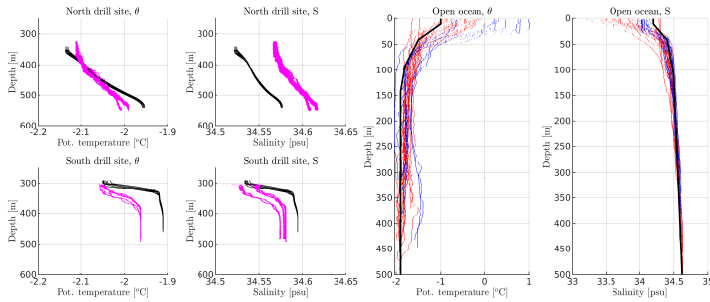Figure 3.5: Simulated and observed vertical profiles of temperature (θ) and salinity (S) under the two hot-water drill sites and in the open ocean. Black solid lines are simulated ocean profiles. Magenta dots are CTD observations from Nicholls et al. (2012). Red dots are CTD observations from Hutchinson et al. (2020) and blue dots are observations from Nicholls et al. (2004). It is important to note that black lines in the open ocean are used as boundary conditions at the eastern and southern bounds for the summer season (October-March). Potential temperature as boundary condition for the winter season is fixed to -1.9^{o}C, while salinity is the same as in the summer.
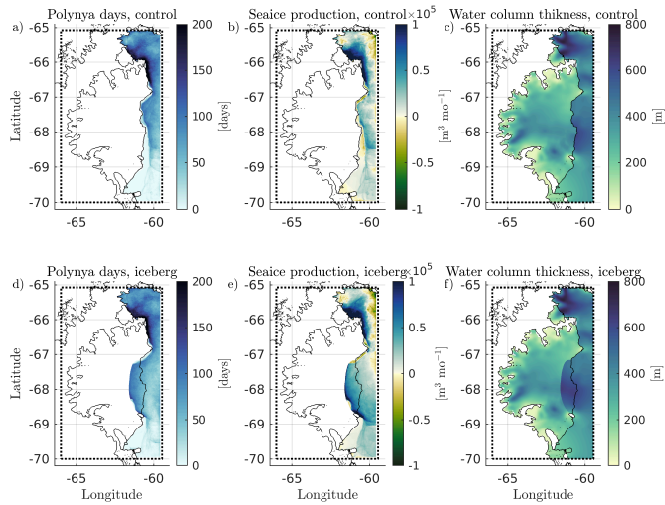
Figure 3.6: Simulated polynya days, seaice production and water column thickness for control (a-c) and iceberg run (d-f). a) Days of polynya, calculated when daily-average seaice thickness between January, 1st 2015 and January, 1st 2017 is less than 2 cm. b) Seaice production rate in control run as a temporal average between January, 1st 2015 and January, 1st 2017. c) Water column thickness (isobaths). d-f) are same as a-c) but for the iceberg experiment.

Figure 3.7: Simulated ocean conditions along the horizontal cross-section corresponding to isopycnal level 27.87. a) Concentration of passive tracer `tr01` as a snapshot of January 1st, 2017. b) Distribution of meltwater fraction (MWF) calculated on the same day. c) Distribution of potential temperature as an average for December 2016. d-f) are same as a-c) but for the iceberg run.
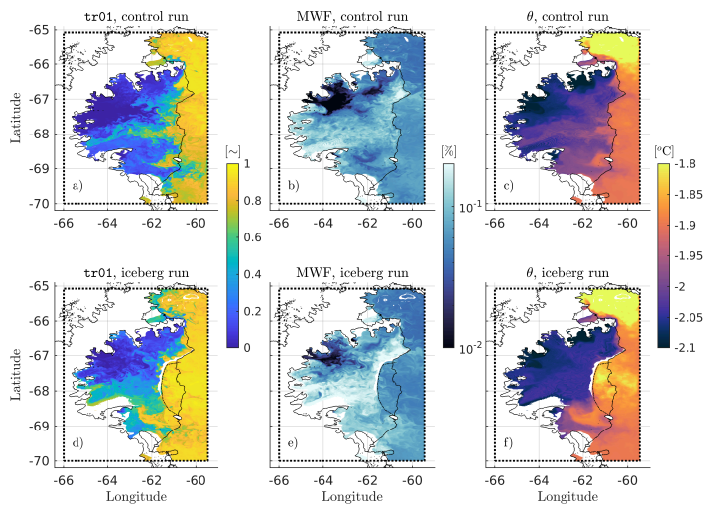
Figure 3.8: Simulated ocean conditions along the horizontal cross-section corresponding to isopycnal level 27.93. a) Concentration of passive tracer `tr01` as a snapshot of January 1st, 2017. b) Distribution of meltwater fraction (MWF) calculated on the same day. c) Distribution of potential temperature as an average for December 2016. d-f) are same as a-c) but for the iceberg run.
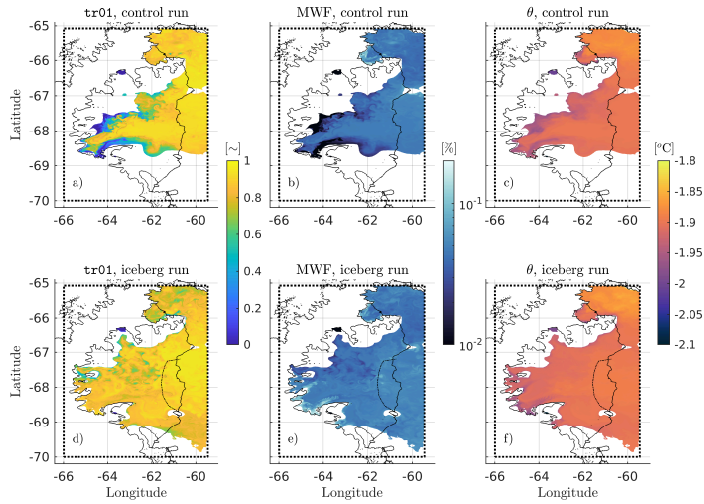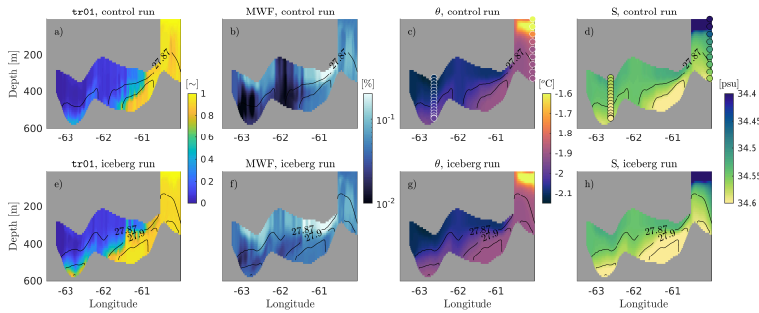

Figure 3.9: Simulated ocean conditions along the vertical cross-section on latitude 66.87°S, aligned with the north drill site. Black contour lines are isopycnal levels. a, b) Concentration of passive tracer `tr01` and meltwater fraction (MWF), respectively, as a snapshot for January 1st 2017 in the control run. c, d) Distribution of potential temperature and salinity in the control run as a monthly average for December 2016. Dotted markers are observation profiles of potential temperature (c) and salinity (d) after CTD data of Nicholls et al. (2012) (under the ice base) and Hutchinson et al. (2020) (open ocean). e-h) are same as a-d) but for the iceberg run.
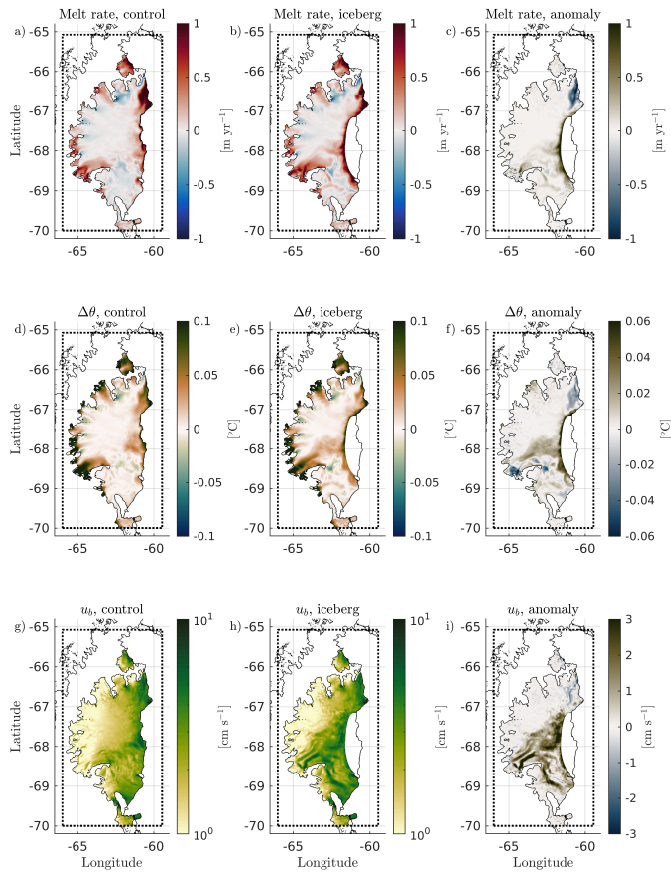
Figure 3.10: Integrated melt rate and melt rate decomposition in terms of thermal driving and friction velocity at the first grid below the ice for control (first column) and iceberg runs (second column) as an average for the month of August 2016. Third column shows the anomaly, calculated as difference between modeled results in iceberg and control run. a-c) is integrated melt rate, d-f) is thermal driving ($\Delta\theta$) and g-h) is friction velocity (u_b).
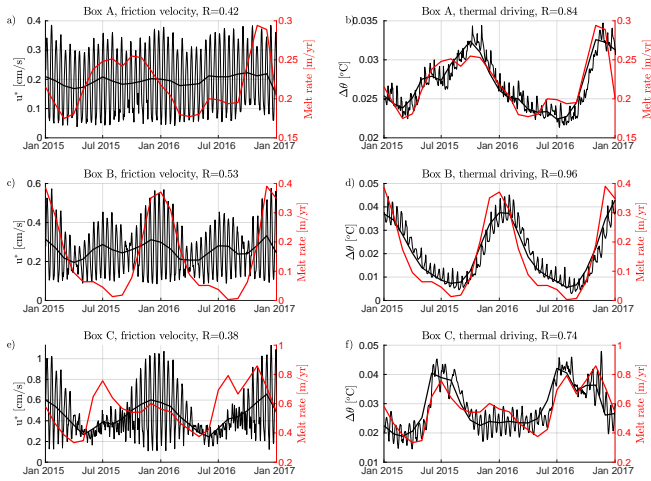
Figure 3.11: Time series of modeled melt rate (red lines) and melt rate decomposition in friction velocity and thermal driving (black lines) for control run. a) and b) are the temporal evolution of friction velocity and thermal driving under box A (south drill site) calculated with daily (thin black line) and monthly (thick black line) model outputs. c-d) are the same as a-b) but under box B (Gipps Ice Rise, GIR), e-f) is same as a-b) but under box C (Bawden Ice Rise, BIR).
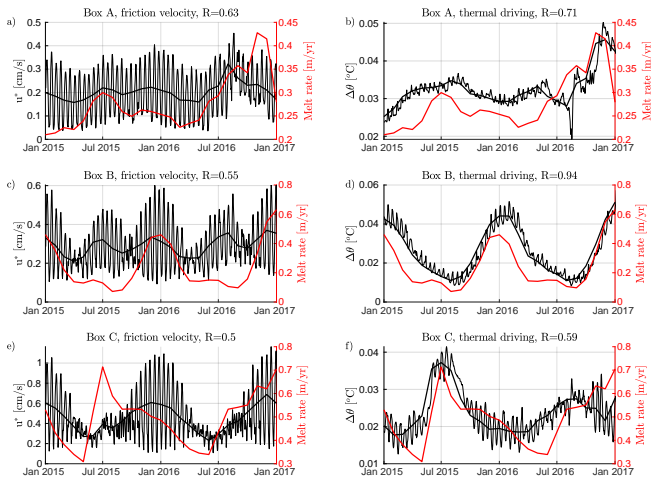
Figure 3.12: Time series of modeled melt rate (red lines) and melt rate decomposition in friction velocity and thermal driving (black lines) for iceberg run. a) and b) are the temporal evolution of friction velocity and thermal driving under box A (south drill site) calculated with daily (thin black line) and monthly (thick black line) model outputs. c-d) are the same as a-b) but under box B (Gipps Ice Rise, GIR), e-f) is same as a-b) but under box C (Bawden Ice Rise, BIR).
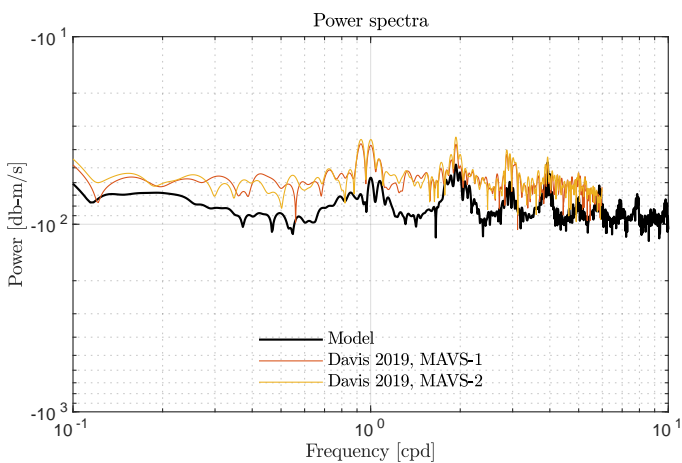
Figure 3.13: Comparison between simulated and observed ocean speed in proximity of the ice base in form of power spectrum. Observation data were obtained via deploying a turbulence instrument clusters (TICs) under the ice base at the south drill site with each Nobska Modular Acoustic Velocity Sensor (MAVS) providing a 392?day record of the turbulent velocity fluctuations starting in December 2011 (Davis and Nicholls, 2019). Modeled velocities (for the control run) are calculated at the first grid below the ice as a spatial average of ocean condition under box A during the two years of nominal simulation.

Chapter 4

Fracture propagation on the Jovian moon Europa

> ... È l'aver noi [...] scoperto quattro Stelle
> erranti, da nessun altro prima di noi
> conosciute ne' osservate, le quali, a
> somiglianza di Venere e Mercurio intorno al
> Sole, hanno lor propri periodi intorno a una
> certa Stella principale.
>
> ———————————————
>
> Galileo Galilei, *Sidereus Nuncius*, 1610

4.1   Summary

Existing lineaments on the surface of the Jovian moon Europa are thought to be the result of ongoing brittle crack formation in the elastic regime. Some of the lineaments are characterized by arcuate and cuspate segments of around 100 km in length. Such arcuate features are called cycloids and can be modeled using linear elastic fracture mechanics, although the dynamics of these fractures is still unknown. Here, we build on existing terrestrial models of rift propagation and extend them to cycloids on the moon. We propose that these cracks tend to grow as a series of nearly instantaneous events, spaced by periods of inactivity. The behavior is similar to what is observed on Antarctic ice shelves, where rifts can remain dormant for years. We argue that dormant periods between growth events could explain the presence of cycloids on Europa even without invoking secular motion of the crust. Furthermore, being able to model propagation events and their timing should help future missions exploring the moon.

4.1   Introduction

Observations coming from past planetary missions, in particular the Galileo space-craft, revealed lineaments and fractures across Europa's surface. Various fracture models and formation scenarios have been proposed, although available data are not sufficient to fully understand how the surface of the moon deforms (e.g. Rhoden et al., 2010a). However, one of the main requirements for the formation of these types of cracks is the existence of liquid water underneath the icy crust (Carr et al., 1998; Pappalardo et al., 1999). Radio doppler tracking and magnetic measurements performed by Galileo revealed a water ocean below the global shell (Anderson et al., 1998; Khurana et al., 1998; Kivelson et al., 2000). Although stratification scales are still poorly constrained, the ocean should be around 100 km deep (e.g. Sohl et al., 2002), while the thickness of the frozen ice shell ranges from a few to more than 30 kilometers (e.g. Billings and Kattenhorn, 2005). Tidal stress produced by gravitational interaction with Jupiter is the main force driving cold ice on Europa to fracture and form these crevasses (e.g. Greenberg et al., 1998; Hoppa et al., 1999, 2001a).

Some of the lineaments are characterized by arcuate and cuspate segments of around 100 km in length. These features are called cycloids and their orientation can be explained by formation due to tensile cracking (Hoppa et al., 2001a,b). In the model of Hoppa et al. (2001a), cycloidal arcs are formed in response to the constantly changing tidal stress magnitude and orientation along Europa's orbit. The stress eventually reaches the ice strength and allows the crack to evolve and follow curved patterns. The rate of change of the tidal stress can be used to derive an apparent growth rate of cycloids of roughly 3 km/hr. By constraining the growth rate, Hoppa et al (2001a) assumed that a cycloidal arc is formed during a single orbit of the moon around Jupiter. However, low temperatures at the surface of Europa (about 100 K (Spencer et al., 1999)) and high strain rates (due to the constantly rotating tidal stress) also imply that ice deforms elastically (Rist and Murrel, 1994). Therefore, cracks on brittle ice should propagate at the high fractions of the speed of sound (Lee et al., 2003). The difference in magnitude between the two speeds can be explained by the fact that cracks on ice are generally evolving at nearly instantaneous rates through several events, similarly to what happens on terrestrial ice shelves. Indeed, on Earth, rifts on ice shelves are formed through episodic cracking events that follows periods of inactivity, when the crack is dormant (Banwell et al., 2017; Bassis et al., 2005; Walker et al., 2013). As a consequence, the apparent growth rate, for example measured by remote sensing, is substantially slower than the actual propagation rate.

Marshall and Kattenhorn (2005) improved on the cycloid growth model of Hoppa et al. (2001a) by describing the cusp formation in response to resolved shear stress at the cusp itself, which results from tailcracking processes. Hurford et al. (2007) further updated the cycloid model with the introduction of secular stress contribution and the variation of material parameters along the cycloid. This allowed improved fits of existing cycloids by introducing a shift in longitude due to secular rotation of the shell (for example due to non-synchronous rotation). Furthermore, Rhoden et al. (2010b) implemented a parameter-searching algorithm that is able of quanti-

tatively inferring rotational parameters of Europa by matching cycloids' shape with observations of the Galileo mission. The latter model suggests that diurnal stress due to non-zero eccentricity, obliquity and physical libration represents the tidal model that better reproduces the shape of observed cycloids. In summary, cycloids have been extensively studied although their propagation rate has not been sufficiently described in the past models. We contribute to this question by introducing a fracture mechanics approach that is able to model episodic and instantaneous cracking events.

On Earth, large availability of in-situ data and observations from remote sensing can be used as a reference to better understand how ice sheets and crevasses evolve. Among numerical models of ice fractures, one of the most straightforward approaches is linear elastic fracture mechanics (LEFM) (Tada et al., 2000). This type of model approximates ice as an elastic medium, allowing for discontinuities in the structure. For example, Van der Veen (1998b) and Van der Veen (1998a) adopt LEFM to calculate equilibrium lengths of surface and bottom crevasses on terrestrial glaciers. Other models that compute horizontal propagation of ice rifts in Antarctica used techniques that can be derived from LEFM theory (Hulbe et al., 2010; Larour et al., 2004a). In addition, LEFM models of crevasse propagation have been tested and validated against a series of observational campaigns in Iceland (Mottram and Benn, 2005). The LEFM approach has been previously applied to Europa with focus on the potential of cracks to penetrate through the entire ice crust, offering a direct connection between the surface and deep ocean (Crawford and Stevenson, 1988; Lee et al., 2005; Qin et al., 2007; Rudol and Manga, 2009). The LEFM methodology could also provide insights into directions and angles of tailcrack formation on the surface (Marshall and Kattenhorn, 2005). However, no previous study has dealt with the horizontal propagation of cycloids on Europa with terrestrial-based models of ice rifts. Although knowledge of surface deformation on Europa is limited, fracture-mechanics tools and terrestrial analogues provide first order estimations, which could be validated by future missions.

In the current work, we follow the LEFM approach of Larour et al. (2004a) to compute crevasse propagation rates of cracks on brittle ice. As a starting point, we fix orbital and rheological parameters and we use elastic fracture mechanics to model the episodic propagation events. Unlike past studies, which assumed that a cycloidal arc is formed continuously, our model is able to calculate the growth rate of cycloids by including dormant periods between propagation events. Periods of inactivity between single events depend on the local stress-strain rate state and the length of the existing crack. After presenting the LEFM methodology and the results of our model, we discuss the implications that these new findings bring to our knowledge of Europa and to its future exploration.

4.2 Methods

Surface stresses on Europa can be calculated through the computation of the tidal potential for internally differentiated spherical bodies (Harada and Kurita, 2006; Jara-

Orué and Vermeersen, 2011; Wahr et al., 2009). Tidal stresses on the ice layer change in magnitude and orientation as a function of Europa's orbital position around Jupiter (Greenberg et al., 1998). These stress fluctuations are thought to drive crevasse propagation on the moon, which can be modeled through LEFM. On Europa, diurnal components of the tidal potential (scaled over one orbital period of the moon, 3.55 days) are due to non-zero eccentricity and non-zero obliquity. Among other models, Jara-Orué and Vermeersen (2011) compute global deformation tensors from the application of Laplace transform-based normal mode theory to tidal responses. We use the analytical formulas of the time-dependent tensor representing surface stresses provided by Jara-Orué and Vermeersen (2011) and due to non-zero eccentricity of 0.0094 (Wahr et al., 2009) and non-zero obliquity of 0.1° (Bills, 2005). We neglect the contribution of relaxation modes, because the time scale of the simulation in the elastic regime is significantly smaller than the Maxwell time we adopt, 9000 years. Further details of how the tidal stress is computed and of the interior model are provided in the supporting information. In terms of rheology, the elastic crust is sufficiently represented by Young's modulus and Poisson's ratio. We use values of 9.29 GPa and 0.33 respectively, appropriate for water ice and consistent with previous studies (e.g. Hoppa et al., 1999; Rhoden et al., 2010b).

In fracture mechanics, three different cracking modes are possible, depending on the local mechanisms of deformation (Tada et al., 2000). In this study, we limit ourselves to Mode-I fracturing. This type of propagation assumes that crack flanks are moving apart from one another under stresses normal to the fracture plane. The current model is based on the calculation of the Mode-I stress intensity factor (also known as K_I) at the tip of an opening ice crevasse. Crack length, geometry and external loads contribute to the stress intensity factor build-up. Eventually, extreme variations of these parameters lead the material to reach failure strength, called material toughness, that allows crack propagation. LEFM is usually adopted to calculate equilibrium length of cracks when this threshold is reached. Examples of LEFM application to glaciers on Earth are Hulbe et al. (2010) and Van der Veen (1998b,a). These works use this technique to compute propagation of (surface and bottom) crevasses on terrestrial ice sheets, when these are loaded with: longitudinal stress, overburden ice pressure and hydrostatic pressure of water-filled crevasses.

On Europa, stress intensity factors of water-free crevasses consist of two main components: the first caused by tensile stress due to tides and the second by overburden ice pressure. If we restrict the simulation to cycloids at the surface, we can neglect the contribution of overburden pressure. Therefore, the stress intensity factor at the tip of a crevasse can be written as (Tada et al., 2000):

$$K_I = F(l)\sigma\sqrt{\pi l} \qquad\qquad (4.1)$$

where σ is the tensile stress at the tip of the crack and l the crack length. F is an analytical function which is related to a centered crack test specimen and based on interpolation of stress intensity factor curves derived in laboratories and based on a single edge notch test specimen (e.g. Tada et al., 2000). Introducing the non-dimensional parameters $\lambda = l/L$ and the total specimen length L, the function F can

be written as:

$$F(\lambda) \quad = \quad 1.12 - 0.23\lambda = 10.55\lambda^2 - 21.75\lambda^3 + 30.39\lambda^4 \qquad (4.2)$$

The tensile stress at the tip together with the length of the already existing crack determines whether K_I reaches the material toughness of the ice leading to crack propagation. If the toughness is hit and the crevasse grows in time, the increment in length l influences the stress intensity factor at the new tip. If the background stress is time-dependent, at the new tip the stress state will also be different from the previous. In the current model, we fix material toughness at 10 KPa m$^{1/2}$, appropriate for water ice (Rist et al., 2002; Van der Veen, 1998b), and we calculate K_I for advancing tips along existing cycloids.

Following Larour et al. (2004a), we adopt the displacement formulation of K_I factor to compute jump-arrest propagation rates. Beside stress intensity factors, LEFM provides tools that calculate opening widths of cracks. For example, in the centered crack test specimen under stress control, the opening width δ at the center of the crack can be written as (Tada et al., 2000):

$$\delta = \frac{4l\sigma}{E} V(l) \qquad (4.3)$$

where E is the Young's modulus of the material (here, ice). $V(l)$ is a geometrical function similar to F in equation (4.1) but is related to a centered crack test specimen and can be read as (Tada et al., 2000):

$$V(l) \quad = \quad -0.071 - 0.0535\frac{l}{L} + 0.169\left(\frac{l}{L}\right)^2 - 0.09\left(\frac{l}{L}\right)^3$$
$$+0.02\left(\frac{l}{L}\right)^4 - 1.071\frac{l}{L}\log\left(1 - \frac{l}{L}\right) \qquad (4.4)$$

Equation 4.4 has an accuracy of 0.6% for any value of l/L [*Tada*, 2000].

We then derive equation (4.3) in time, in order to relate crevasse propagation rate to strain rate and width derivative $\partial\delta/\partial t$, which represents the opening rate. In symbols:

$$\frac{\partial\delta}{\partial t} = \frac{\partial}{\partial t}\left[\frac{4l\sigma}{E}V(l)\right] \qquad (4.5)$$

which can be rearranged in the following form:

$$\frac{\partial l}{\partial t} = f(\sigma, \dot{\epsilon}, l, \frac{\partial\delta}{\partial t}) \qquad (4.6)$$

where $\partial l/\partial t$ is the crevasse propagation rate and $\dot{\epsilon}$ the strain rate. Equation (4.6) implies that the propagation rate at the tip of a crack is a function of stress, strain rate, crack length and opening rate. The knowledge of these 4 factors at the tip of the crevasse allows the estimation of the crack propagation rate. This type of

fracture growth is referred as stick-slip propagation with jump-arrest increment of the crack (Larour et al., 2004a). This fracturation process is characterized by extremely rapid propagation events that follow phases of inactivity due to conditions that are unfavorable to allow further growth. This approach was able to estimate both the nearly instantaneous cracking events that characterize propagation of rifts on the Ronne Ice Shelf in Antarctica and the apparent slower growth rate that is actually measured by remote sensing (Larour et al., 2004b,a).

There are different ways to measure the opening of a crack on ice. For example, Larour et al. (2004b,a) measure opening widths and opening rates of Antarctic rifts with InSAR data. Since observational constraints on surface deformation of Europa are lacking, we approximate opening width of cycloids with the displacement δ at the center of the crack derived from LEFM theory, i.e. equation (4.3). Furthermore, we approximate the opening rate as follows:

$$\frac{\partial \delta}{\partial t} = \delta \dot{\epsilon} \tag{4.7}$$

where $\dot{\epsilon}$ is the local strain rate. For the deformation being elastic, strain and stress solved on a plane are proportionally related by the compliance matrix, function of the Young's modulus and Poisson's ratio (Timoshenko and Goodier, 1970):

$$\begin{bmatrix} \epsilon_x \\ \epsilon_y \\ \gamma_{xy} \end{bmatrix} = \frac{1}{E} \begin{bmatrix} 1 & -\nu & 0 \\ -\nu & 1 & 0 \\ 0 & 0 & 2(1+\nu) \end{bmatrix} \begin{bmatrix} \sigma_x \\ \sigma_y \\ \sigma_{xy} \end{bmatrix} \tag{4.8}$$

where the coordinates x and y refer to zonal and meridional directions while E and ν are Young's modulus and Poisson's ratio. Since the elastic compliance matrix is not time-dependent, stress rate and strain rate are related by the same proportion of stress and strain. Thus, time derivation of the stress tensor of Jara-Orué and Vermeersen (2011) is sufficient to compute strain rate for any location at any orbital position of Europa. However, equations (4.3) and (4.7) are first order approximations of crack width and opening rate. In the current model, opening rates reach a magnitude of mm/yr. On the other hand, the opening width is calculated as a few meters, which is lower than the geological measurements of Galileo (Coulter et al., 2009; Kattenhorn and Hurford, 2009).

We develop a local approach that computes a series of stress intensity factors along an existing lineament, in order to calculate the growth rate of cycloids and the dormant period between propagation events. To achieve this, we map cycloidal arcs and cusps at their exact location in the QGIS Geographic Information System (GIS) software as a series of nodes separated by equidistant segments within each arc. The nodes that discretize the cycloids are obtained by using the equidistant cylindrical sphere projection of the USGS global mosaic of Europa obtained from Voyager and Galileo data. After we obtain latitude and longitude of each node through the shaping process, orientation and length of each segment are calculated with standard spherical geometry formulas (Wertz, 2001). We then compute deformation for each node of the mapped features by rotating stress tensors from the global geographic co-

ordinate system (Jara-Orué and Vermeersen, 2011) to local referential components, using Mohr's circle (Timoshenko and Goodier, 1970):

$$\sigma^n = \frac{1}{2}(\sigma_x + \sigma_y) - \frac{1}{2}(\sigma_x - \sigma_y)\cos 2\alpha + \sigma_x \sin 2\alpha \qquad (4.9)$$

$$\sigma^t = \frac{1}{2}(\sigma_x - \sigma_y)\sin 2\alpha + \sigma_{xy}\cos 2\alpha \qquad (4.10)$$

where σ^n and σ^t are tensile and tangential stress whereas σ_x, σ_y and σ_{xy} are zonal and meridional stress components, obtained from Jara-Orué and Vermeersen (2011). The angle α represents the orientation of each segment, which can be computed by spherical geometry routines from the coordinates of the nodes (Wertz, 2001). Figure 4.1a) shows one of the observed equatorial cycloids where the rotation of the stress tensor from geographical to local direction of a single node is sketched in the inset. In the figure, the rotation angle α characterizes the orientation of the different segments, thus the same angle is used in equations (4.9) and (4.10).

By fixing the direction of propagation and the initial coordinates of the first node, the model computes stress intensity factors of advancing nodes along observed crevasses. Stick-slip propagation rates with jump-arrest increment of the crack are computed if the ice toughness is reached at the advancing node. If this is the case, the crack grows in length along the prescribed segment. Figure 1b) shows a sketch of the model set-up. The model calculates intensity factor, opening width and propagation rate at N-1 advancing nodes, which are related to equidistant segments. While the background stress is constant along a single segment, different segments (at different locations) are subjected to differing stress states. In order to determine whether the segments adjacent to the tip are contributing to the length of the open crack, our model calculates whether these are forced with tensile stress. If this is the case, we assume that the segments behind the advancing node do influence the length of the crevasse. This process conserves the variation of stress at different locations of Europa and the different orientation of the segments. Thus, the model repeats the analysis until the entire shape of the observed cycloid is reproduced or one of the node is not experiencing conditions that are allowing further propagation.

4.3 Results and Discussion

The cycloids observed on Europa represent an ideal case for the application of our fracture model to brittle ice. The extreme cold temperature at the surface and the consistency of the cycloid orientations with tensile stress justify our assumptions of elasticity and opening fractures. The new model is able to reproduce the prescribed shape of 4 cycloids observed on the surface of the moon. We model 2 features at low latitudes and Delphi and Cilicia flexi at the south pole. We name the equatorial cycloids as EQ1 and EQ2. EQ2, Delphi and Cilicia are also reproduced in Rhoden et al. (2010b). We discretize the 4 cycloids with 10000 nodes and equidistant segments on the order of meters.
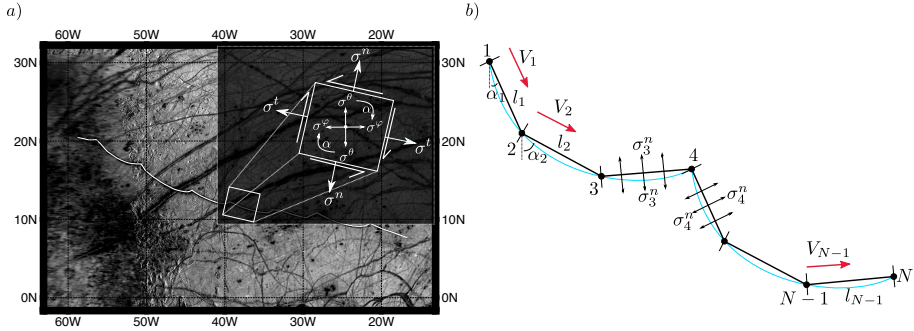
Figure 4.1: Panels describing the geometry of the propagation model. Figure 1a) shows one of the discretized cycloids with a sketch of the rotation of the stress tensor in the black inlet. Figure 1b) shows the geometry of the discretized cycloid (black line) in nodes and segments. The observed shape of the cycloid is the blue line. Each node (except the last one) is associated with segment length l, orientation angle α, tensile load σ^n and propagation rate V.

Table 4.1 summarizes the results of our LEFM computations in terms of maximum propagation properties of the 4 features. As already mentioned, our model reproduces a single cycloid by bursts of propagation events, happening at each node. In the table, V indicates the maximum propagation rate at which the cycloid evolves, according to the model. This speed represents the maximum rate of a single propagation event. $\partial \delta / \partial t$ is the maximum opening rate and δ the maximum crack width. The table includes the time required to the complete evolution of the observed cycloid and the time of inactivity. Finally, the growth rate is calculated by dividing the total length of the cycloid by the time required to complete the feature.

The growth rate is orders of magnitude smaller than the propagation rate that characterizes the bursts of activity. Propagation rates reach values of hundred of meters per second while the apparent growth rate is of tens of meters per day. This is due to the fact that certain nodes require time for the stress field to rotate in order to reach the material toughness and to allow propagation. For example, figure 4.2 shows a detail of the model acting on the cusp. Extreme variations in the orientation of the segments across the cusp affect the length of the open crack and the orientation of the normal stress. This means that at the cusp, the crack remains dormant. The propagation is initiated again if the stress intensity factor reaches the material

Table 4.1: Estimation of propagation parameters with our LEFM-based model.

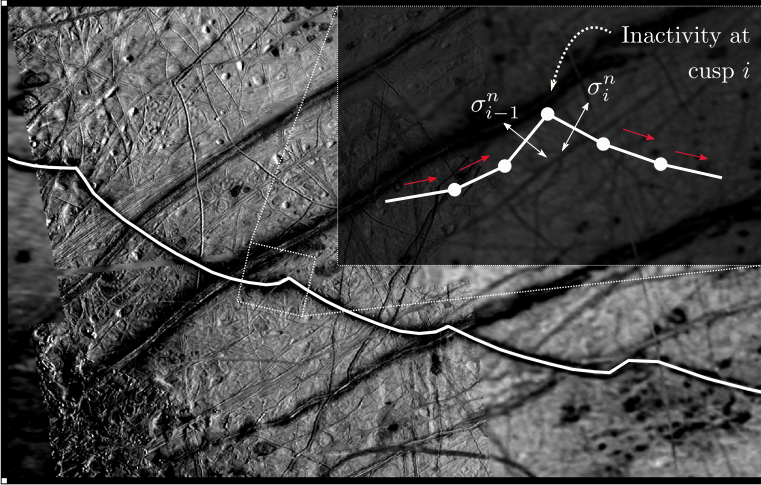| Cycloid	V [m/s]	$\partial \delta / \partial t$ [mm/yr]	δ [m]	Time of inactivity [days]	Time to completion [days]	Growth rate [m/day]
EQ1	135.93	1.37	0.67	606	858	8.72
EQ2	69.31	5.97	4.06	39	64	198.26
Delphi flexus	535.54	10.93	4.95	82	573	25.54
Cilicia flexus	572.99	2.36	3.71	64	250	28.95

Figure 4.2: Detail of Figure 4.1. The black inlet shows the discretization of the cusp. The $i-1$ node experiences stress state that measures σ_{i-1}^n. The abrupt change in the orientation angle of the node i with respect to the previous node implies that the stress field needs to reorient in order to reach σ_i^n. During this period of time the cycloid is dormant.

toughness. Given the observed paths, we are able to reproduce the entire geometry of EQ2, Delphi and Cilicia. The propagation of EQ1 arrests at node 4759 and the stress field prescribed by the current tidal set up does not permit further propagation. Our model predicts that the cycloids in the southern hemisphere have a similar behavior. Here the bursts of activity reach very high propagation rates with relative slow growth rate. On the other hand, EQ2 grows faster but with relatively slower propagation events. This discrepancy is mainly due to the difference in the strain rate at the two locations on the surface. This is strictly prescribed by the stress forcing adopted in the model.

As already mentioned, the same behavior that our model predicts for cycloids on Europa is observed on rifts in Antarctica. Here cracks grow at an apparent rate that is slower than episodic propagation events (e.g. Banwell et al., 2017; Bassis et al., 2005). On Earth, rifts can remain dormant for years and generally grow at rates on the order of meters per day (Fricker et al., 2005; Walker et al., 2013; Walker and Gardner, 2019). Observation from remote sensing suggests that rifts on terrestrial ice shelves experience variations in the propagation rate that often have a strong seasonal dependance (Fricker et al., 2005; Walker et al., 2015). Furthermore, several
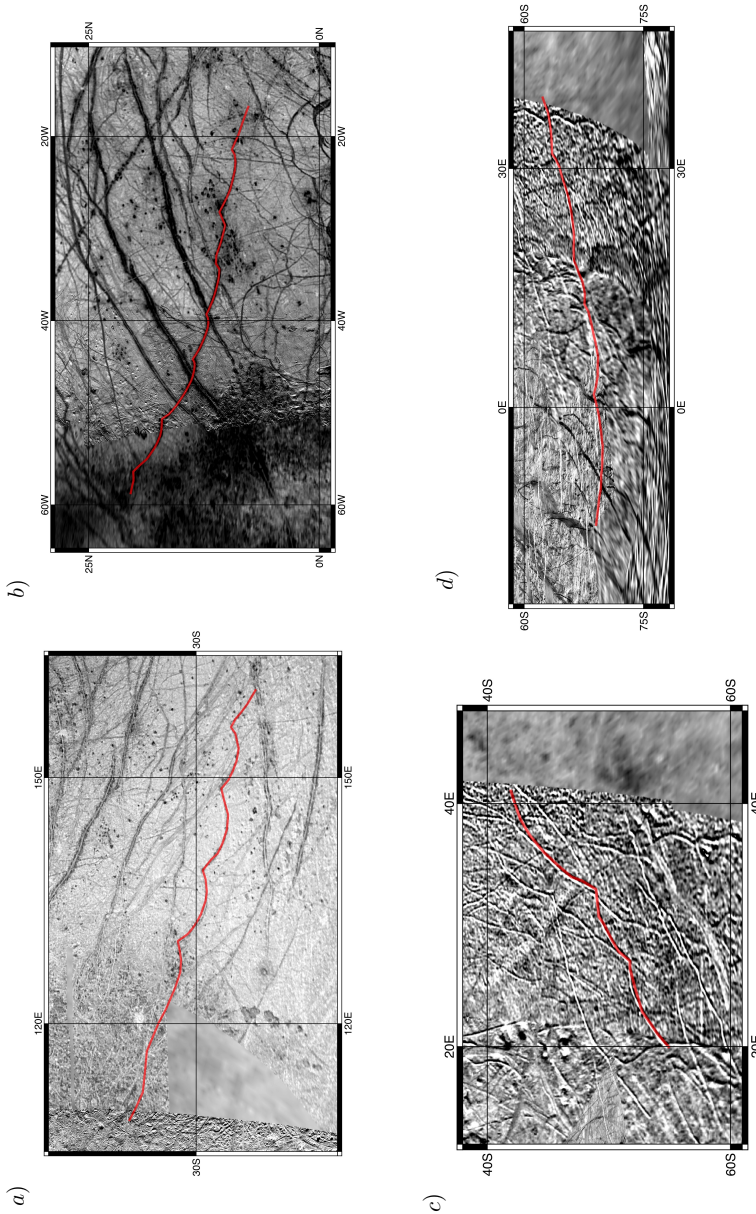
Figure 4.3: a-c are images of the 4 cycloids using the global mosaic of Europa. Courtesy of Astrogeology Science Center. a and b show cyclods EQ1 and EQ2 while c and d show Delphi and Cilicia

works propose that the mixture of iceberg fragments, sea ice and snow (often called as ice melange) that fill the crack can have a substantial influence in the propagation of rifts (Fricker et al., 2005; Khazendar et al., 2009; Larour et al., 2014). The filling

of crevasses on Europa should also play a substantial role in the determination of how the cracks grow. Unlike what happens on Earth, Europa lacks key observations of crack behavior and physical characteristics of rifts and their filling.

However, future explorations missions will observe the moon in order to address prominent questions about the nature of the surface and interior and the prospect for material exchange between the two. For example, NASA's Europa Clipper is designed to perform about 45 flybys over the nominal mission lifetime of 3.5 years. This means roughly one flyby every month, with only a few opportunities for overlapping observations. The first science campaign of Europa Clipper will cover the anti-jovian hemisphere with clusters of data overlaps during two sub-phases of about 6 months each (Lam et al., 2018). Therefore, overlapping observations of the same areas should be less than 6 months apart. We estimate that crevasses evolve on an average timeframe of around hundreds of days. This period is roughly similar to the total observation period of a single hemisphere of the moon, designed to last less than one year. Average opening width would be of a few meters (value δ in table 4.1). Therefore, we conclude that Europa Clipper should be able to detect partial development of crevasses provided that the imaging resolution of the spacecraft is of m/pixel.

Unlike previous studies on cycloids, we model dormant periods between growth events. As a consequence, our model estimates that cycloids on Europa grow at rates that are 1 to 2 orders of magnitude lower than past studies (e.g. Hurford et al., 2007; Rhoden et al., 2010b). By introducing periods of inactivity, the model is able to calculate the propagation rate at the exact location. This is a substantial difference with past models, which require longitudinal shift in order to fit some cycloids, including Delphi and Cilicia (Hurford et al., 2007; Rhoden et al., 2010b). This shift was explained by secular rotation of the crust such as non-synchronous rotation. Our model suggests that dormant periods between growth events could improve fits of lineaments at their exact locations on the moon. Finally, it could also alleviate the necessity of secular motion of the crust to explain the presence of cycloids.

4.4   Conclusions

Our model extends LEFM techniques to estimate horizontal propagation scenarios by using the observed shape of cycloids on Europa. We find that crevasses evolve in a relatively short amount of time by a series of nearly instantaneous fracturing events (order of hundreds of m/s), similarly to what is observed on rifts in Antarctica. We introduce the simulation of periods of inactivity of these cracks. This capability was not considered by previous fracture models which calculate much faster growth rates, as a consequence. Beside improving fits of existing cycloids, the introduction of this critical feature could have important implication for our understanding of the rotation state of Europa. We argue that it might also explain the presence of cycloids even without considering secular motion of the crust.

Furthermore, we suggest that the Europa Clipper spacecraft should be able to detect propagation events provided that the flyby repetition time over the same area

is few months apart. Our findings estimate that cracks should evolve over hundreds of days which is a roughly similar timescale compared to the coverage of the same area by the most recent trajectory baseline of the spacecraft (less than one year). In addition, we estimate that the opening width of crevasses measures a few meters. Hence, we suggest that an imaging resolution of m/pixel would be required to capture the scale of these events.

Chapter 5

Conclusions and perspectives

> All that ocean of blue
> soon as those clouds
> Pass away.

<div align="right">Jack Kerouac</div>

In Chapter 1, I formulate a set of research questions which have been addressed in Chapters 2-4. Here, I summarize the key findings and the extent to which these research objectives have been achieved. Furthermore, I conclude this dissertation with perspectives of this work and a list of recommendations.

5.1 Conclusions

1. **To what extent is ocean dynamics underneath an ice shelf affected by the presence of a prominent kilometer-wide rift?**

   This question is addressed in Chapter 2.

   Ice rifts and their impact on the circulation below and around ice shelves are often neglected in ocean models due to the coarse resolutions used, which are unable to resolve fractures in the ice shelf that can be several kilometers wide.

   To address this knowledge gap, in this chapter I use the Massachussetts Institute of Technology general circulation model at high resolution. I simulate an idealized ice shelf and show that a significant rift near the ice shelf front substantially affects the sub-shelf dynamics and the distribution of basal melt. This impact is mainly related to two processes. Firstly, off-shelf water intrusion, which reaches and melts ice in the proximity of the grounding line, is inhibited by the presence of the rift. The rift indeed acts as a second discontinuity in the water column thickness after the ice front, causing off-shelf water to deviate along the rift base. Secondly, in the case of a rifted ice shelf, off-shelf water intruding along the ice base is replaced by the outflow of dense Rift Water from inside the rift. This water is formed when seawater reaches the higher freezing

temperature in the rift, causing it to salinify and sink. The simulations also show that the downward flow of Rift Water weakens the water stratification by supplying denser water close to the ice base. As a result, the ambient water under rifted ice shelves is cooler than in intact experiments, leading to a reduction in the basal melt rate, which is quantified to be20% less than in the case of a fully intact ice shelf.

These simulations indicate that ice-shelf rifts affect the sub-shelf circulation and melt in the vicinity of the grounding line, which is sensitive to off-shelf water incursion. Robust estimations of melt patterns at the grounding line are indeed crucial because sustained melting can cause further ungrounding of continental ice and accelerate ice discharge from outlet glaciers into the ocean. These simulations show how ice rifts near the ice front and Rift Water formation from freezing processes within the rift modulate off-shelf water intrusion and heat redistribution under the ice base. Accurately representing ice shelf cavity geometry is critical to reproduce sub-shelf dynamics, and these results showcase the importance for ocean models to account for ice rifts to accurately simulate heat intrusion.

2. **What is the impact of the separation of iceberg A-68 from the Larsen C Ice Shelf on the sub-shelf dynamics?**

This question is addressed in Chapter 3.

Recent studies have shown that ice front retreat substantially alters the ocean dynamics in the proximity of Antarctic ice shelves. It is, however, unknown how the calving of iceberg A-68 affected these sub-shelf circulation patterns and the heat delivery under the Larsen C ice shelf.

To address this knowledge gap, in this chapter I use the Massachussetts Institute of Technology general circulation model at high resolution to simulate ocean dynamics in close proximity to and below the Larsen C Ice Shelf both before and after the calving of iceberg A-68. The pre-calving run is in excellent agreement with *in-situ* and remote observations and simulates realistic pathways of ocean heat intrusion towards the grounding line. The results indicate that basal melt is primarily driven by the topographically-driven intrusion of water formed at the surface during wintertime sea-ice growth. The removal of iceberg A-68 drives redistribution of heat under the ice, resulting in enhanced melting in the southern section of the domain. In particular, the calving event causes enhanced ocean heat intrusion and, in turn, basal melt in the vicinity of the Gipps Ice Rise to double. As ablation close to this pinning point is critical for the ice-shelf dynamics, this result highlights a positive feedback for further destabilization. These ocean simulations build understanding on the need to consider updated ice-shelf coastlines to accurately project ocean circulation below the ice base and the consequent implications for the stability of the ice shelf.

3. **Can we successfully apply terrestrial ice fracturing models to investigate how cracks propagate on the surface of Europa?**

This question is addressed in Chapter 4.

Several numerical efforts have attempted to simulate the dynamics of cycloids as ice fractures on Europa but actual propagation events remain scarcely constrained given the paucity of available observations. On the other hand, the large availability of information from *in-situ* and remote sensing regarding ice fracture on the terrestrial ice sheets allowed a more advanced understanding of processes driving rifting and crack propagation.

To address this knowledge gap, in this chapter I built on an existing terrestrial-based numerical model of rift propagation on ice shelves and extend it to cycloids on the moon. The model reproduces a single cycloid by bursts of propagation events on the order of hundreds of meters per second, which are alternated with periods of inactivity, often experienced at the cusps. This is due to the abrupt change in cycloid orientation along the cusp, which drive the stress field to fall below the material threshold and arrest propagation. Moreover, the model results explain the presence of cycloids even without considering secular motion of the crust.

The model predicts that cycloids on Europa exhibit a behavior similar to that observed on rifts in Antarctica. In Antarctica, cracks grow at a rate that appears to be slower than the rate of episodic propagation events while rifts can remain dormant for years and generally grow at rates on the order of meters per day. Remote sensing observations suggest that rifts on terrestrial ice shelves experience variations in propagation rate that often have a strong seasonal dependence. Furthermore, several studies propose that the mixture of iceberg fragments, sea ice, and snow (often referred to as "ice melange") that fills the cracks can have a substantial influence on the propagation of rifts. The filling of crevasses on Europa should also play a significant role in determining how the cracks grow. However, unlike for Earth, Europa lacks key observations of crack behaviour and physical characterisation of rifts and their filling.

5.2   Perspectives and recommendations

This section concludes the dissertation. I formulate here final perspectives on the simulations performed, while presenting a list of recommendation for future work.

The simulations described in this dissertation serve to underscore the importance of considering the correct geometry of the ice shelf cavity. This is crucial to accurately reproduce ocean dynamics and the pathways of heat intrusions under the ice shelf base. Model results show that a prominent rift acts as a discontinuity in the ice shelf geometry and can alter sub-shelf dynamics and redistribute the exchange of heat between ocean and ice shelf base. This leads to a significant drop in melt rate of

up to 20% for an idealized ice shelf geometry considering temperature and salinity profiles representative of warm and cold Antarctic cavities. Additionally, the case of Larsen C was used to show that iceberg separation from the ice shelf geometry can also impact pathways of heat intrusion under the ice shelf, potentially leading to a positive feedback for destabilization. The simulations conducted in Chapter 2 are the first attempt to investigate the role of rifts in the heat delivery under the ice shelf base. There is therefore a crucial need for more numerical efforts to evaluate the impact of ice shelf geometry on the basal ablation of Antarctic ice shelves.

The results from the simulations presented in Chapter 2 and 3 suggest that the formation of ice rifts and frontal retreat may have contrasting effects on the melt rates under Antarctic ice shelves. However, it is important to note that, in both chapters, the highlight is the role of the hydrography of the ice-shelf cavity in the delivery of heat beneath the ice shelves. As ocean currents follow lines of constant depth (isobaths), the presence of rifts introduces a second discontinuity in the isobaths (after the ice front), diverting off-shelf water along the rift and replacing it with the outflow of denser Rift Water from within the rift. This process weakens the stratification of the water column, resulting in cooler ambient water under rifted ice shelves and subsequently reducing basal melt. On the other hand, a calving event, specifically the detachment of iceberg A-68 from the Larsen C Ice Shelf in 2017, may drive enhanced ocean heat intrusion and basal melt. The separation of iceberg A-68 leads the water column at the ice front to thicken, smoothing the gradient in the isobaths. These findings indicate that rift formation and iceberg calving have divergent short-term effects on melt rates. However, over longer time scales, it is likely that the net effect will be an overall enhancement of melting. This is because rift formation is temporary and does not permanently alter the ice shelf configuration, whereas iceberg calving results in the detachment of a substantial mass of ice, potentially exposing larger areas of deep water column, which facilitates heat intrusion under the ice shelf. Further numerical work, supported by observations, is necessary to quantify these processes under other Antarctic ice shelves.

One limitation of the simulations described in this dissertation is the absence of a realistic module to account for the presence of ice mélange. Modeling this heterogeneous material poses significant challenges, so it is often parameterized in numerical models. Moreover, the temporal evolution of ice mélange trapped between fractured ice is still unknown. In Chapter 2, I used the "ice-capped" approximation to represent the prominent rift near the ice front, while in Chapter 3, I did not distinguish between meteoric and ice mélange. However, further investigation is needed to fully understand its importance, as it could be a crucial link between climate forcing and ice shelf stability (Larour et al., 2021). Future models should aim to implement ice mélange accretion modules to better integrate the impact of this material in the dynamics of ice and ocean in Antarctica.

The presented work investigates ocean dynamics and fracture propagation using numerical models. Although the models are constrained by available data, they remain idealized versions since they provide solutions to simplified numerical equations. A better understanding of how these processes evolve, both in Antarctica and

on Europa, is only possible with more in-situ and remote observations. In particular, cruise expeditions and drilling sites are very important for constraining ice shelf ablation and the characteristics of the water near and below Antarctic ice shelves. On the other hand, the *Europa Clipper* mission will be pivotal in solving some of the puzzling questions about the physics of Europa, with the main goal of understanding whether the moon can sustain life.

The urgency to better understand how the Earth's system behaves is driven by the ongoing climate warming crisis. Consequently, our understanding of the dynamics of Antarctic ice shelves is advancing at a faster pace compared to our knowledge of ice on Europa. This progress is primarily due to fieldwork campaigns and remote sensing observations conducted in Antarctica. The insights gained from studying terrestrial ice sheets can contribute to expanding our understanding of physics on other celestial bodies. Overall, this dissertation shows the potential for synergy between Earth and planetary science. By leveraging advances in our understanding of physical processes on Earth, terrestrial-based models and theories contribute to expanding our knowledge of physics on other celestial bodies. This interdisciplinary approach, supported and validated by remote sensing and *in-situ* missions, is fundamental to advance our understanding of ice fractures, their interaction with the surrounding environment, and their dynamics throughout the Solar System.

Bibliography

Adcroft, A., C. Hill, and J. Marshall, 1997: The representation of topography by shaved cells in a height coordinate model. *Monthly Weather Reviews*, **125 (9)**, 2293–2315.

Adusumilli, S., H. A. Fricker, B. Medley, L. Padman, and M. R. Siegfried, 2020: Interannual variations in meltwater input to the southern ocean from antarctic ice shelves. *Nature Geosc.*, **13**, 616–620.

Adusumilli, S., H. A. Fricker, M. R. Siegfried, L. Padman, F. S. Paolo, and S. R. M. Ligtenberg, 2018: Variable basal melt rates of antarctic peninsula ice shelves, 1994–2016. *Geophys. Res. Lett.*, **40**, 4086–4095.

Amundson, J., C. Kienholz, A. O. Hager, R. H. Jackson, R. J. Motyka, J. D. Nash, and D. A. Sutherland, 2020: Formation, flow and break-up of ephemeral ice mélange at LeConte Glacier and Bay, Alaska. *Journal of Glaciology*, **66**, 577–590.

Anderson, J. D., G. Schubert, R. A. Jacobson, E. L. Lau, W. B. Moore, and W. L. Sjorgen, 1998: Europa's differentiated internal structure: Inferences from four Galileo encounters. *Science*, **281**, 2019–2022, doi:10.1126/science.281.5385.2019.

Armitage, T. W. K., R. Kwok, A. F. Thompson, and G. Cunningham, 2018: Dynamic topography and sea level anomalies of the southern ocean: Variability and teleconnections. *Journal of Geophysical Research: Oceans*, **123 (1)**, 613–630.

Arzeno, I. B., R. C. Beardsley, R. Limeburner, B. Owens, L. Padman, S. R. Springer, C. L. Stewart, and M. J. M. Williams, 2014: Ocean variability contributing to basal melt rate near the ice front of ross ice shelf, antarctica. *Journal of Geophysical Research: Oceans*, **119 (7)**, 4214–4233.

Bamber, J. L., R. E. M. Riva, B. L. A. Vermeersen, and A. M. LeBrocq, 2009: Reassessment of the potential sea-level rise from a collapse of the west antarctic ice sheet. *Science*, **324 (5929)**, 901–903, doi:10.1126/science.1169335.

Banwell, A. F., I. C. Willis, G. J. Macdonald, B. Goodsell, D. P. Mayer, and A. Powell, 2017: Calving and rifting on the McMurdo Ice Shelf, Antarctica. *Annals of Glaciology*, **58**, 78–87, doi:10.1017/aog.2017.12.

Bassis, J. N., R. Coleman, H. Fricker, and J. Minster, 2005: Episodic propagation of a rift on the Amery Ice Shelf, East Antarctica. *Geophysical Research Letters*, **32 (L06502)**, doi:10.1029/2004GL022048.

Billings, S. E., and S. A. Kattenhorn, 2005: The great thickness debate: Ice shell thickness models for Europa and comparisons with estimates based on flexure at ridges.he great thickness debate: Ice shell thickness models for europa and comparisons with estimates based on flexure at ridges. *Icarus*, **177**, 397–412, doi:10.1016/j.icarus.2005.03.013.

Bills, B. G., 2005: Free and forced obliquities of the Galilean satellites of Jupiter. *Icarus*, **175**, 233–247, doi:10.1016/j.icarus.2004.10.028.

Böning, C. W., A. Dispert, M. Visbeck, S. R. Rintoul, and F. U. Schwarzkopf, 2008: The response of the antarctic circumpolar current to recent climate change. *Nature Geoscience*, **1 (12)**, 864–869.

Borstad, C., D. McGrath, and A. Pope, 2017: Fracture propagation and stability of ice shelves governed by ice shelf heterogeneity. *Geophysical Research Letters*, **44**.

Borstad, C. P., E. Rignot, J. Mouginot, and M. P. Schodlok, 2013: Creep deformation and buttressing capacity of damaged ice shelves: theory and application to Larsen C ice shelf. *Cryosphere*, **7**, 1931–1947.

Bradley, A. T., D. T. Bett, P. Dutrieux, J. De Rydt, and P. R. Holland, 2022: The influence of pine island ice shelf calving on basal melting. *Journal of Geophysical Research: Oceans*, **127 (9)**, e2022JC018 621, doi:https://doi.org/10.1029/2022JC018621, e2022JC018621 2022JC018621.

Breyer, C., and H. Fricker, 2022: Spatiotemporal analysis of icesat-2 observation of ice mélange thickness in antarctic rifts. *AGU Fall Meeting Abstracts*, Vol. 2022.

Brisbourne, A., and Coauthors, 2020: An updated seabed bathymetry beneath larsen c ice shelf, antarctic peninsula. *Earth System Science Data*, **12 (2)**, 887–896, doi:10.5194/essd-12-887-2020, URL https://essd.copernicus.org/articles/12/887/2020/.

Brohan, P., J. J. Kennedy, I. Harris, S. F. B. Tett, and P. D. Jones, 2006: Uncertainty estimates in regional and global observed temperature changes: A new data set from 1850. *Journal of Geophysical Research: Atmospheres*, **111**.

Burchard, H., K. Bolding, A. Jenkins, M. Losch, M. Reinert, and L. Umlauf, 2022: The vertical structure and entrainment of subglacial melt water plumes. *Journal of Advances in Modeling Earth Systems*, **14(3)**, doi:10.1029/2021MS002925.

Campin, J. M., and Coauthors, 2020: MITgcm/MITgcm: mid 2020 version (Version checkpoint67s), Zenodo. URL https://doi.org/10.5281/zenodo.3967889.

Carr, M. H., and Coauthors, 1998: Evidence for a subsurface ocean on Europa. *Nature*, **177**, 363–365, doi:10.1038/34857.

Cook, A. J., and D. G. Vaughan, 2010: Overview of areal changes of the ice shelves on the antarctic peninsula over the past 50 years. *The Cryosphere*, **4 (1)**, 77–98, doi:10.5194/tc-4-77-2010, URL https://tc.copernicus.org/articles/4/77/2010/.

Cook, J., and Coauthors, 2013: Quantifying the consensus on anthropogenic global warming in the scientific literature. *Environmental Research Letters*, **8 (024024)**.

Cook, J., and Coauthors, 2016: Consensus on consensus: a synthesis of consensus estimates on human-caused global warming. *Environmental Research Letters*, **11 (048002)**.

Coulter, C. E., S. A. Kattenhorn, and P. A. Shenk, 2009: Topographic profile analysis and morphologic characterization of Europa's double ridges. *Lunar and Planetary Science XL*, Lunar and Planetary Institute, Houston., 363–365, 1960.

Crawford, G. D., and D. J. Stevenson, 1988: Gas-driven water volcanism and the resurfacing of Europa. *Icarus*, **73**, 66–79, doi:10.1016/0019-1035(88)90085-1.

Cuffey, K., and W. S. B. Paterson, 2006: *The Physics of Glaciers*. 4th ed., Elsevier.

Darelius, E., I. Fer, and K. W. Nicholls, 2016: Observed vulnerability of filchner-ronne ice shelf to wind-driven inflow of warm deep water. *Nature Communications*, **7 (1)**, 12 300, doi:10.1038/ncomms12300.

Davis, P. E. D., and K. W. Nicholls, 2019: Turbulence observations beneath larsen c ice shelf, antarctica. *J. Geophys. Res.: Oceans*, **124**.

DeConto, R. M., and D. Pollard, 2016: Contribution of antarctica to past and future sea-level rise. *Nature*, **531 (7596)**, 591–597, doi:10.1038/nature17145, URL https://doi.org/10.1038/nature17145.

DiGirolamo, N., C. L. Parkinson, D. J. Cavalieri, P. Gloersen, and H. J. Zwally, 2022: Sea Ice Concentrations from Nimbus-7 SMMR and DMSP SSM/I-SSMIS Passive Microwave Data, Version 2. NASA National Snow and Ice Data Center Distributed Active Archive Center, doi:10.5067/MPYG15WAA4WX.

Dinniman, M. S., X. S. Asay-Davis, B. K. Galton-Fenzi, P. R. Holland, A. Jenkins, and R. Timmermann, 2016: Modeling Ice Shelf/Ocean Interaction in Antarctica: A Review. *Oceanography*, **29(4)**, 144–153.

Doake, C. S. M., H. F. J. Corr, H. Rott, P. Skvarca, and N. W. Young, 1998: Breakup and conditions for stability of the northern Larsen Ice Shelf, Antarctica. *Nature*, **391 (6669)**, 778–780.

Donohue, K. A., K. L. Tracey, D. R. Watts, M. P. Chidichimo, and T. K. Chereskin, 2016: Mean antarctic circumpolar current transport measured in drake passage. *Geophysical Research Letters*, **43 (22)**, 11,760–11,767.

Dupont, T. K., and R. B. Alley, 2005: Assessment of the importance of ice-shelf buttressing to ice-sheet flow. *Geophysical Research Letters*, **32 (4)**.

Emetc, V., P. Tregoning, M. Morlighem, C. Borstad, and M. Sambridge, 2018: A statistical fracture model for Antarctic ice shelves and glaciers. *Cryosphere*, **12 (10)**, 3187–3213.

Fahnestock, M. A., W. Abdalati, and C. A. Shuman, 2002: Long melt seasons on ice shelves of the Antarctic Peninsula: an analysis using satellite-basedmicrowave emission measurements. *Annals of Glaciology*, **34 (1)**, 127–133.

Frederikse, T., and Coauthors, 2020: The causes of sea-level Rise since 1900. *Nature*, **584**, 393–397.

Fretwell, P., and Coauthors, 2013: Bedmap2: improved ice bed, surface and thickness datasets for antarctica. *The Cryosphere*, **7 (1)**, 375–393.

Fricker, H. A., N. W. Young, R. Coleman, J. R. Bassis, and J. B. Minster, 2005: Multi-year monitoring of rift propagation on the Amery Ice Shelf, East Antarctica. *Geophysical Research Letters*, **32**, L02 502, doi:10.1029/2004GL021036.

Fürst, J. J., G. Durand, F. Gillet-Chaulet, T. Tavard, M. Rankl, M. Braun, and O. Gagliardini, 2016: The safety band of Antarctic ice shelves. *Nature Climate Change*, **6 (5)**, 479–482.

Goelzer, H., and Coauthors, 2020: The future sea-level contribution of the greenland ice sheet: a multi-model ensemble study of ismip6. *The Cryosphere*, **14 (9)**, 3071–3096, doi:10.5194/tc-14-3071-2020, URL https://tc.copernicus.org/articles/14/3071/2020/.

Goldberg, D. N., C. M. Little, O. V. Sergienko, A. Gnanadesikan, R. Hallberg, and M. Oppenheimer, 2012: Investigation of land ice-ocean interaction with a fully coupled ice-ocean model: 1. Model description and behavior. *Journal of Geophysical Research*, **117**, 1–16.

Graham, A. G. C., and Coauthors, 2022: Rapid retreat of thwaites glacier in the pre-satellite era. *Nature Geoscience*, **15 (9)**, 706–713, doi:10.1038/s41561-022-01019-9, URL https://doi.org/10.1038/s41561-022-01019-9.

Greenberg, R., P. Geissler, B. R. Tufts, and G. V. Hoppa, 2000: Habitability of europa's crust: The role of tidal-tectonic processes. *Journal of Geophysical Research-Planets*, **105**, 17 551–17 562.

Greenberg, R., G. V. Hoppa, P. Geissler, A. Sarid, and B. R. Tufts, 2002: The rotation of europa. *Celestial Mechanics and Dynamical Astronomy*, **83**, 35–47.

Greenberg, R., and Coauthors, 1998: Tectonic Processes on Europa: Tidal Stresses, Mechanical Response, and Visible Features. *Icarus*, **135**, 54–78, doi:10.1006/icar.1998.5986.

Gregory, J. M., and Coauthors, 2013: Twentieth-century global-mean sea level rise: Is the whole greater than the sum of the parts? *Journal of Climate*, **26 (13)**, 4476 – 4499, doi:https://doi.org/10.1175/JCLI-D-12-00319.1, URL https://journals.ametsoc.org/view/journals/clim/26/13/jcli-d-12-00319.1.xml.

Grosfeld, K., R. Gerdes, and J. Determan, 1997: Thermohaline circulation and interaction between ice shelf cavities and the adjacent open ocean. **102**, 15 595–15 610, doi:10.1029/97JC00891.

Harada, Y., and K. Kurita, 2006: Tectonic Processes on Europa: Tidal Stresses, Mechanical Response, and Visible Features. *Planetary and Space Science*, **54**, 170–180, doi:10.1016/j.pss.2005.12.001.

Harrison, L. C., P. R. Holland, K. J. Heywood, K. W. Nicholls, and A. M. Brisbourne, 2022: Sensitivity of melting, freezing and marine ice beneath larsen c ice shelf to changes in ocean forcing. *Geophysical Research Letters*, **49 (4)**, e2021GL096 914, doi:https://doi.org/10.1029/2021GL096914, e2021GL096914 2021GL096914.

Hartmann, D. L., and Coauthors, 2013: *Observations: Atmosphere and Surface*, chap. 2. Cambridge University Press, Cambridge, United Kingdom and New York, NY, USA,.

Hattermann, T., O. A. Nøst, J. M. Lilly, and L. H. Smedsrud, 2012: Two years of oceanic observations below the fimbul ice shelf, antarctica. *Geophysical Research Letters*, **39 (12)**.

Hattermann, T., and Coauthors, 2021: Observed interannual changes beneath filchner-ronne ice shelf linked to large-scale atmospheric circulation. *Nature Communications*, **12 (1)**, 2961, doi:10.1038/s41467-021-23131-x, URL https://doi.org/10.1038/s41467-021-23131-x.

Hay, C. C., E. Morrow, R. E. Kopp, and J. X. Mitrovica, 2015: Probabilistic reanalysis of twentieth-century sea-level rise. *Nature*, **517 (7535)**, 481–484, doi:10.1038/nature14093, URL https://doi.org/10.1038/nature14093.

Hellmer, H. H., F. Kauker, R. Timmermann, J. Determann, and J. Rae, 2012: Twenty-first-century warming of a large antarctic ice-shelf cavity by a redirected coastal current. *Nature*, **485 (7397)**, 225–228, doi:10.1038/nature11064.

Hellmer, H. H., and D. J. Olbers, 1989: A two-dimensional model of the thermohaline circulation under an ice shelf. *Antarctic Science*, **1**, 325–336.

Hersbach, H., and Coauthors, 2020: The ERA5 global reanlysis. *Q. J. R. Met. Soc.*, **146**, 1999–2049, doi:10.1002/qj.3803.

Hewitt, I. J., 2020: Subglacial Plumes. *Annual Reviews of Fluid Mechanics*, **52**, 145 – 169.

Hofer, S., C. Lang, C. Amory, C. Kittel, A. Delhasse, A. Tedstone, and X. Fettweis, 2020: Greater greenland ice sheet contribution to global sea level rise in cmip6. *Nature Communications*, **11 (1)**, 6289,

doi:10.1038/s41467-020-20011-8, URL https://doi.org/10.1038/s41467-020-20011-8.

Hogg, A. M., M. P. Meredith, D. P. Chambers, E. P. Abrahamsen, C. W. Hughes, and A. K. Morrison, 2015: Recent trends in the southern ocean eddy field. *Journal of Geophysical Research: Oceans*, **120 (1)**, 257–267.

Holland, D. M., and A. Jenkins, 1999: Modeling thermodynamic ice-ocean interactions at the base of an ice shelf. *J. of Physical Oceanography*, **29 (8)**, 1787–1800.

Holland, P. R., H. F. J. Corr, D. G. Vaughan, and A. Jenkins, 2009: Marine ice in larsen ice shelf. *Geophys. Res. Lett.*, **36**.

Holland, P. R., and Coauthors, 2015: Oceanic and atmospheric forcing of larsen c ice-shelf thinning. *The Cryosphere*, **9 (3)**, 1005–1024, doi:10.5194/tc-9-1005-2015, URL https://tc.copernicus.org/articles/9/1005/2015/.

Hoppa, G. V., B. R. Tufts, R. Greenberg, and P. E. Geissler, 1999: Strike-slip faults on Europa: Global shear patterns driven by tidal stress. *Icarus*, **141**, 287–298, doi:10.1016/j.pss.2005.12.001.

Hoppa, G. V., B. R. Tufts, R. Greenberg, and P. E. Geissler, 2001a: Formation of cycloidal features on Europa. *Science*, **285**, 1899–1902, doi:10.1126/science.285.5435.1899.

Hoppa, G. V., B. R. Tufts, R. Greenberg, T. A. Hurford, O. D. P., and P. E. Geissler, 2001b: Europa's rate of rotation derived from the tectonic sequence in the Astypalaea region. *Icarus*, **153**, 208–213, doi:10.1006/icar.2001.6663.

Hulbe, C. L., C. LeDoux, and K. Cruikshank, 2010: Propagation of long fractures in the Ronne Ice Shelf, Antarctica, investigated using a numerical model of fracture propagation. *Journal of Glaciology*, **56**, 459–472, doi:10.3189/002214310792447743.

Hurford, T. A., A. R. Sarid, and R. Greenberg, 2007: Cycloidal cracks on Europa: Improved modeling and non-synchronous rotation implications. *Icarus*, **186**, 218–233, doi:10.1016/j.icarus.2006.08.026.

Hussmann, H., D. Shoji, G. Steinbrugge, A. Stark, and F. Sohl, 2016: Constraints on dissipation in the deep interiors of ganymede and europa from tidal phase-lags. *Celestial Mechanics and Dynamical Astronomy*, **126**, 131–144.

Hutchinson, K., and Coauthors, 2020: Water mass characteristics and distribution adjacent to larsen c ice shelf, antarctica. *Journal of Geophysical Research: Oceans*, **125 (4)**, e2019JC015 855, doi:https://doi.org/10.1029/2019JC015855, e2019JC015855 2019JC015855.

Jackett, D. R., and T. J. McDougall, 1995: Minimal adjustment of hydrographic profiles to achieve static stability. *J. Atmos. Ocean. Technol.*, **12 (4)**, 381–389, doi:10.1175/1520-0426(1995)012<0381:MAOHPT>2.0.CO;2.

Jacobs, S. S., H. H. Hellmer, C. S. M. Doake, A. Jenkins, and R. M. Frolich, 1992: Melting of ice shelves and the mass balance of Antarctica. *Journal of Glaciology*, **38**, 375–387.

Jansen, D., A. Luckman, B. Kulessa, P. R. Holland, and E. C. King, 2013: Marine ice formation in a suture zone on the Larsen C Ice Shelf and its influence on ice shelf dynamics. *Journal of Geophysical Research: Earth Surface*, **118**, 1–13.

Jansen, D., A. Luckman, A. J. Cook, S. Bevan, B. Kulessa, B. Hubbard, and P. R. Holland, 2015: Brief Communication: Newly developing rift in Larsen C Ice Shelf presents significant risk to stability. *Cryosphere*, **9**, 1223–1227.

Jara-Orué, H. M., and B. L. A. Vermeersen, 2011: Effects of low-viscous layers and a non-zero obliquity on surface stresses induced by diurnal tides and non-synchronous rotation: The case of Europa. *Icarus*, **215**, 417–438, doi:10.1016/j.icarus.2011.05.034.

Jenkins, A., 1991: A one-dimensional model of ice shelf-ocean interaction. *Journal of Geophysical Research*, **96 C(11)**, 20 671– 20 677, doi:10.1029/91JC01842.

Jenkins, A., and A. Bombosh, 1995: Modeling the effects of frazil ice crystals on the dynamics and thermodynamics of ice shelf water plumes. *J. Geophys. Res.: Oceans*, **100**, 6967–6981.

Jenkins, A., S. Dutrieux, S. Jacobs, G. H. Steig, G. H. Gudmundsson, J. Smith, and K. J. Heywood, 2016: Decadal ocean forcing and Antarctic ice sheet response: Lessons from the Amundsen Sea. *Oceanography*, **29 (4)**, 106–117.

Jordan, J. J., P. R. Holland, A. Jenkins, M. D. Piggot, and S. Kimura, 2014: Modeling ice-ocean interaction in ice-shelf crevasses. *Journal of Geophysical Research: Oceans*, **119**, 995–1008.

Joughin, I., and R. B. Alley, 2011: Stability of the west antarctic ice sheet in a warming world. *Nature Geoscience*, **4**, 506–511.

Kattenhorn, S. A., and T. Hurford, 2009: *Europa*, Vol. 215, chap. Tectonics on Europa., 199–236. University of Arizona Press, Tucson, Arizona.

Khazendar, A., and A. Jenkins, 2003: A model of marine ice formation within Antarctic ice shelf rifts. *Journal of Geophysical Research*, **108 (C7)**, 1–13.

Khazendar, A., E. Rignot, and E. Larour, 2009: Roles of marine ice, rheology, and fracture in the flow and stability of the Brunt/Stancomb-Wills Ice Shelf. *Journal of Geophysical Research*, **114**, F04 007, doi:10.1029/2008JF001124.

Khurana, K. K., M. G. Kivelson, D. J. Stevenson, G. Schubert, C. T. Russel, R. J. Walker, and C. Polanskey, 1998: Induced magnetic fields as evidence for subsurface oceans in Europa and Callisto. *Nature*, **395**, 777–780, doi:10.1038/27394.

Kivelson, M. G., K. K. Khurana, C. T. Russel, M. Volwerk, R. J. Walker, and C. Zimmer, 2000: Galileo magnetometer measurements: A stronger case for a subsurface ocean at Europa. *Science*, **289**, 1340–1343, doi:10.1126/science.289.5483.1340.

Kjeldsen, K. K., and Coauthors, 2015: Spatial and temporal distribution of mass loss from the greenland ice sheet since ad 1900. *Nature*, **528 (7582)**, 396–400, doi:10.1038/nature16183, URL https://doi.org/10.1038/nature16183.

Kopp, R. E., R. M. Horton, C. M. Little, J. X. Mitrovica, M. Oppenheimer, D. J. Rasmussen, B. H. Strauss, and C. Tebaldi, 2014: Probabilistic 21st and 22nd century sea-level projections at a global network of tide-gauge sites. *Earth's Future*, **2 (8)**, 383–406, doi:https://doi.org/10.1002/2014EF000239, URL https://agupubs.onlinelibrary.wiley.com/doi/abs/10.1002/2014EF000239, https://agupubs.onlinelibrary.wiley.com/doi/pdf/10.1002/2014EF000239.

Kulessa, B., D. Jansen, A. J. Luckman, E. C. King, and P. R. Sammonds, 2014: Marine ice regulates the future stability of a large Antarctic ice shelf. *Nature Communications*, **5**.

Lam, T., B. Buffington, S. Campagnola, C. Scott, and O. M, 2018: A robust mission tour for NASA's planned Europa Clipper mission. *AIAA SciTech Forum*, AIAA 2018 Space Flight Mechanics Meeting, Vol. 2018-0202, doi:10.2514/6.2018-0202.

Large, W., J. McWilliams, and S. Doney, 1994: Oceanic vertical mixing: A review and a model with nonlocal boundary layer parameterization. *Reviews of Geophysics*, **32**, 363–403.

Larour, E., A. Khazendar, C. P. Borstad, H. Seroussi, M. Morlinghem, and E. Rignot, 2014: Representation of sharp rifts and faults mechanics in modeling ice shelf flow dynamics: Application to Brunt/Stancomb-Wills Ice Shelf, Antarctica. *Journal of Geophysical Research: Earth Surface*, **119**, 1918–1935, doi:10.3189/172756504781829837.

Larour, E., E. Rignot, and D. Aubry, 2004a: Modelling of rift propagation on Ronne Ice Shelf, Antarctica, and sensitivity to climate change. *Geophysical Research Letters*, **31 (L16404)**, doi:10.1029/2004GL020077.

Larour, E., E. Rignot, and D. Aubry, 2004b: Processes involved in the propagation of rifts near Hemmen Ice Rise in the Ronne Ice Shelf, Antarctica. *Journal of Glaciology*, **50 (170)**, 329–341, doi:10.3189/172756504781829837.

Larour, E., E. Rignot, M. Poinelli, and B. Scheuchl, 2021: Physical processes controlling the rifting of Larsen C Ice Shelf, Antarctica, prior to the calving of iceberg A68. *Proceedings of the National Academy of Sciences of the United States of America*, **118**, doi:10.1073/pnas.2105080118.

Larour, E., H. Seroussi, M. Morlighem, and E. Rignot, 2012: Continental scale, high order, high spatial resolution, ice sheet modeling using the Ice Sheet System Model (ISSM). *Journal of Geophysical Research*, **117 (F01022)**.

Lawrence, J. D., and Coauthors, 2023: Crevasse refreezing and signatures of retreat observed at kamb ice stream grounding zone. *Nature Geoscience*, **16 (4)**, 238–243, doi:10.1038/s41561-023-01129-y.

Lee, S., R. T. Pappalardo, and N. C. Makris, 2005: Mechanics of tidally driven fractures in Europa's ice shell. *Icarus*, **177**, 367–379, doi:10.1016/j.icarus.2005.07.003.

Lee, S., M. Zanolin, A. M. Thode, R. T. Pappalardo, and N. C. Makris, 2003: Probing Europa's interior with natural sound sources. *Icarus*, **165**, 144–167, doi:10.1016/S0019-1035(03)00150-7.

Lewis, E. L., and R. G. Perkin, 1983: Supercooling and Energy Exchange Near the Arctic Ocean Surface.

Geophysical Research Letters, **88**, 7681–7685.

Lin, X., X. Zhai, Z. Wang, and D. R. Munday, 2018: Mean, variability, and trend of southern ocean wind stress: Role of wind fluctuations. *Journal of Climate*, **31 (9)**, 3557 – 3573.

Lipovsky, B., 2020: Ice shelf rift propagation: stability, three-dimensional effects, and the role of marginal weakening. *Cryosphere*, **14, 1673–1683**.

Losch, M., 2008: Modeling ice shelf cavities in a z coordinate ocean general circulation model. *Journal of Geophysical Research: Oceans*, **113**.

Losch, M., D. Menemenlis, J.-M. Campin, P. Heimback, and C. Hill, 2010: On the formulation of sea-ice models. part 1: Effects of different solver implementations and parameterizations. *Ocean Modelling*, **33**, 129–144.

MacAyeal, D. R., E. Rignot, and C. L. Hulbe, 1998: Ice-shelf dynamics near the front of the Filchner-Ronne Ice Shelf, Antarctica, revealed by SAR interferometry: model/interferogram comparison. *Journal of Glaciology*, **44 (147)**, 419–428.

Marshall, S. T., and C. Kattenhorn, 2005: A revised model for cycloid growth mechanics on Europa: Evidence from surface morphologies and geometries. *Icarus*, **177**, 341–366, doi:10.1016/j.icarus.2005.02.022.

Masson-Delmotte, V., and Coauthors, 2021: IPCC, 2021: Climate Change 2021: The Physical Science Basis. Contribution of Working Group I to the Sixth Assessment Report of the Intergovernmental Panel on Climate Change. Tech. rep.

McGranahan, G., D. Balk, and B. Anderson, 2007: The rising tide: assessing the risks of climate change and human settlements in low elevation coastal zones. *Environment and Urbanization*, **19 (1)**, 17–37, doi:10.1177/0956247807076960, URL https://doi.org/10.1177/0956247807076960, https://doi.org/10.1177/0956247807076960.

McGrath, D., K. Steffen, P. Holland, T. Scambos, H. Rajaram, W. Abdalati, and E. Rignot, 2014: The structure and effect of suture zones in the Larsen C Ice Shelf, Antarctica. *Journal of Geophysical Research: Earth Surface*, **119 (3)**, 588 – 602.

Menemenlis, D., I. Fukumori, and T. Lee, 2007: Atlantic to Mediterranean Sea Level Difference Driven by Winds near Gibraltar Strait. *Journal of Physical Oceanography*, **37 (2)**, doi:10.1175/JPO3015.1.

Morice, C. P., J. J. Kennedy, N. A. Rayner, and P. D. Jones, 2012: Quantifying uncertainties in global and regional temperature change using an ensemble of observational estimates: The hadcrut4 data set. *Journal of Geophysical Research: Atmospheres*, **117**.

Morlighem, M., E. Rignot, J. Mouginot, H. Seroussi, and E. Larour, 2014: Deeply incised submarine glacial valleys beneath the greenland ice sheet. *Nature Geoscience*, **7 (6)**, 418–422.

Morlighem, M., and Coauthors, 2020: Deep glacial troughs and stabilizing ridges unveiled beneath the margins of the Antarctic ice sheet. *Nature Geoscience*, **13 (2)**, 132–137.

Mottram, R. H., and D. I. Benn, 2005: Testing crevasse-depth models: a field study at Breidamerkurjökull. *Journal of Glaciology*, **55**, 746–752, doi:10.3189/002214309789470905.

Mueller, R. D., L. Padman, M. S. Dinniman, S. Y. Erofeeva, H. A. Fricker, and M. A. King, 2012: Turbulence observations beneath larsen c ice shelf, antarctica. *J. Geophys. Res.: Oceans*, **117**.

Nakayama, Y., C. Cai, and H. Seroussi, 2021: Impact of Subglacial Freshwater Discharge on Pine Island Ice Shelf. *Geophysical Research Letters*, **48 (18)**, e2021GL093 923, doi:10.1029/2021GL093923.

Nakayama, Y., D. Menemenlis, M. Schodlok, and E. Rignot, 2017: Amundsen and Bellingshausen Seas simulation with optimizedocean, sea ice, and thermodynamic ice shelf model parameters. *Geophys. Res. Lett.*, **(122)**, 6180–6195.

Nakayama, Y., D. Menemenlis, H. Zhang, M. Schodlok, and E. Rignot, 2018: Origin of Circumpolar Deep Water intruding onto the Amundsen and Bellingshausen Sea continental shelves. *Nature Communication*, **9**, 3403.

Nakayama, Y., and Coauthors, 2019: Pathways of ocean heat towards Pine Island and Thwaites grounding lines. *Scientific Reports*, **9**, 16 649.

Nicholls, K. W., K. Makinson, and E. J. Venables, 2012: Ocean circulation beneath Larsen C Ice Shelf, Antarctica from in situ observations. *Geophys. Res. Lett.*, **39 L19608**, 995–1008, doi:10.1029/2012GL053187.

Nicholls, K. W., S. Østerhus, K. Makinson, T. Gammelsrød, and E. Fahrbach, 2009: Ice-ocean processes over the continental shelf of the southern weddell sea, antarctica: A review. *Reviews of Geophysics*, **47 (3)**.

Nicholls, K. W., C. J. Pudsey, and P. Morris, 2004: Summertime water masses off the northern Larsen C Ice Shelf, Antarctica. *Geophysical Research Letters*.

Nicholls, R. J., and A. Cazenave, 2010: Sea-level rise and its impact on coastal zones. *Science*, **328 (5985)**, 1517–1520.

NOAA, 2021: Noaa national centers for environmental information, monthly global climate report for annual 2020. Tech. Rep. https://www.ncei.noaa.gov/access/monitoring/monthly-report/global/202013., NOAA.

Obase, T., A. Abe-Ouchi, K. Kusahara, H. Hasumi, and R. Ohgaito, 2017: Responses of basal melting of antarctic ice shelves to the climatic forcing of the last glacial maximum and co2 doubling. *Journal of Climate*, **30 (10)**, 3473 – 3497.

Ojakangas, G. W., and D. J. Stevenson, 1989: Thermal state of an ice shell on europa. *Icarus*, **81**, 220–241.

Orheim, O., J. O. Hagen, S. Østerhus, and A. C. Saetrang, 1990: Glaciological and oceanographic studies on fimbulisen during nare 1989/90, in filchner-ronne ice shelf programme. *edited by H. Oerter*, **Rep. 4.**, 120–129.

Orsi, A. H., and T. Whitworth, 2005: *Hydrographic Atlas of the World Ocean Circulation Experiment (WOCE).*, Vol. 1. International WOCE Project Office, Southampton, UK.

Otosaka, I. N., and Coauthors, 2023: Mass balance of the greenland and antarctic ice sheets from 1992 to 2020. *Earth System Science Data*, **15 (4)**, 1597–1616, doi:10.5194/essd-15-1597-2023, URL https://essd.copernicus.org/articles/15/1597/2023/.

Padman, L., H. A. Fricker, R. Coleman, S. Howard, and L. Erofeeva, 2002: A new tidal model for the antarctic ice shelves and seas. *Ann. Glaciol.*, **34**, 247–254.

Paolo, F., H. A. Fricker, and L. Padman, 2015: Volume loss from Antarctic ice shelves is accelerating. *Science*, **348**.

Pappalardo, R., and M. D. Coon, 1996: A sea analog for the surface of europa. *Lunar Planetary Science Conference XXVII*, Vol. XXVII, 997-998.

Pappalardo, R. T., W. B. McKinnon, and K. K. Khurana, 2009: *Europa*. The University of Arizona Press.

Pappalardo, R. T., and Coauthors, 1999: Does Europa have a subsurface ocean? Evaluation of the geological evidence. *Journal of Geophysical Research*, **104**, 24 015–24 055, doi:10.1029/1998JE000628.

Petty, A. A., D. L. Feltham, and P. Holland., 2013: Impact of atmospheric forcing on Antarctic continental shelf water masses. *Journal of Physical Oceanography*, **43**, 920–940.

Poertner, H. O., and Coauthors, 2019: IPCC, 2019: IPCC Special Report on the Ocean and Cryosphere in a Changing Climate. Tech. rep.

Poinelli, M., 2023: MPoinelli/Poinelli2023aTC: v1 (Version v1), Zenodo. URL https://doi.org/10.5281/zenodo.7905547.

Poinelli, M., E. Larour, J. Castillo-Rogez, and B. Vermeersen, 2019: Crevasse Propagation on Brittle Ice: Application to Cycloids on Europa. *Geophysical Research Letters*, **46**, 11 756–11 763, doi:10.1029/2019GL084033.

Poinelli, M., Y. Nakayama, E. Larour, M. Vizcaino, and R. Riva, 2023a: Ice-front retreat controls on ocean dynamics under larsen c ice shelf, antarctica. *Geophysical Research Letters*, **50 (18)**, e2023GL104 588, doi:10.1029/2023GL104588.

Poinelli, M., M. Schodlok, E. Larour, M. Vizcaino, and R. Riva, 2023b: Can rifts alter ocean dynamics beneath ice shelves? *The Cryosphere*, **17 (6)**, 2261–2283, doi:10.5194/tc-17-2261-2023.

Potter, J. R., and J. G. Paren, 1985: *Oceanology of the Antarctic Continental Shelf. Antarct. Res. Ser.*, chap. Interaction between ice shelf and ocean inGeorge VI Sound, Antarctica. AGU, Washington DC.

Pritchard, H., S. Ligtenberg, H. Fricker, D. Vaughan, and van den Broeke M., 2012: Antarctic ice-sheet loss driven by basal melting of ice shelves. *Nature*, **484**, 502–505.

Qin, R., W. R. Buck, and L. Germanovich, 2007: Comment on "mechanics of tidally driven fractures in europa's ice shell" by s. lee, r.t. pappalardo, and n.c. makris [2005. icarus 177, 367-379]. *Icarus*, **189**, 595–597.

Rahmstorf, S., G. Foster, and N. Cahill, 2017: Global temperature evolution: recent trends and some pitfalls. *Environmental Research Letters*, **12**.

Rambaux, N., Van Hoolst, T., and Karatekin, Ö., 2011: Librational response of europa, ganymede, and callisto with an ocean for a non-keplerian orbit. *A&A*, **527**, A118, doi:10.1051/0004-6361/201015304, URL https://doi.org/10.1051/0004-6361/201015304.

Rhoden, A. R., T. A. Hurford, L. Roth, and K. Retherford, 2010a: Linking Europa's plume activity to tides, tectonics, and liquid water. *Icarus*, **253**, 168–178, doi:10.1016/j.icarus.2015.02.023.

Rhoden, A. R., B. Militzer, E. M. Huff, T. A. Hurford, M. Manga, and M. A. Richards, 2010b: Constraints on Europa's rotational dynamics from modeling of tidally-driven fractures. *Icarus*, **210**, 770–784, doi:10.1016/j.icarus.2010.07.018.

Rignot, E., G. Casassa, P. Gogineni, W. Krabill, A. Rivera, and R. Thomas, 2004: Accelerated ice discharge from the Antarctic Peninsula following the collapse of Larsen B ice shelf. *Geophysical Research Letters*, **31 (L18401)**, 479–482.

Rignot, E., S. Jacobs, J. Mouginot, and B. Scheuchl, 2013: Ice shelf melting around Antarctica. *Science*, **341 (6143)**, 266–270.

Rignot, E., and S. S. Jacobs, 2002: Rapid bottom melting widespread near antarctic ice sheet grounding lines. *Science*, **296 (5575)**, 2020–2023.

Rignot, E., and D. R. MacAyeal, 1998: Ice-shelf dynamics near the front of the Filchner-Ronne Ice Shelf, Antarctica, revealed by SAR interferometry. *Journal of Glaciology*, **44**, 405–418.

Rignot, E., J. Mouginot, B. Scheuchl, M. van den Broeke, M. J. van Wessem, and M. Morlighem, 2019: Four decades of Antarctic Ice Sheet mass balance from 1979 to 2017. *Proceedings of the National Academy of Sciences of the United States of America*, **116 (4)**, 1095–1103.

Rintoul, S., 2009: Antarctic circumpolar current. *Encyclopedia of Ocean Sciences (Second Edition)*, J. H. Steele, Ed., second edition ed., Academic Press, Oxford, 178–190, doi:https://doi.org/10.1016/B978-012374473-9.00603-2.

Rist, M. A., and S. A. F. Murrel, 1994: Ice triaxial deformation and fracture. *Journal of Glaciology*, **40**, 305–318, doi:10.3189/S0022143000007395.

Rist, M. A., P. R. Sammonds, H. Oerter, and C. S. M. Doake, 2002: Fracture of Antarctic shelf ice. *Journal of Glaciology*, **107**, 305–318, doi:10.1029/2000JB000058.

Roth, L., J. Saur, K. D. Retherford, D. F. Strobel, P. D. Feldman, M. A. McGrath, and F. Nimmo, 2014: Transient water vapor at europa's south pole. *Science*, **343**, 171–174.

Rott, H., W. Rack, P. Skvarca, and H. De Angelis, 2002: Northern Larsen Ice Shelf, Antarctica: further retreat after collapse. *Annals of Glaciology*, **34**, 277–282.

Rott, H., P. Skvarca, and T. Nagler, 1996: Rapid collapse of northern Larsen Ice Shelf, Antarctica. *Science*, **271 (5250)**, 788–792.

Rudolf, M. L., and M. Manga, 2009: Fracture penetration in planetary ice shells. *Icarus*, **199**, 536–541, doi:10.1016/j.icarus.2008.10.010.

Sasgen, I., and Coauthors, 2020: Return to rapid ice loss in greenland and record loss in 2019 detected by the grace-fo satellites. *Communications Earth & Environment*, **1 (1)**, 8, doi:10.1038/s43247-020-0010-1, URL https://doi.org/10.1038/s43247-020-0010-1.

Scambos, T. A., J. A. Bohlander, C. A. Shuman, and P. Skvarca, 2004: Glacier acceleration and thinning after ice shelf collapse in the Larsen B embayment, Antarctica. *Geophysical Research Letters*, **31 (L18402)**, 1–4.

Scambos, T. A., C. Hulbe, and M. Fahnestock, 2003: *Climate-induced ice shelf disintegration in the Antarctic Peninsula.*, chap. Antarctic Peninsula Climate Variability: Historical and Paleoenvironmental Perspectives, Antarct. Res. Ser, 79–92. AGU, Washington DC.

Scambos, T. A., C. Hulbe, M. Fahnestock, and J. Bohlander, 2000: The link between climate warming and break-up of ice shelves in the Antarctic Peninsula. *Journal of Glaciology*, **46 (154)**, 516–530.

Schmidtko, S., K. J. Heywood, A. F. Thompson, and S. Aoki, 2014: Multidecadal warming of antarctic waters. *Science*, **346 (6214)**, 1227–1231.

Schodlok, M., D. Menemenlis, E. Rignot, and M. Studinger, 2012: Sensitivity of the ice-shelf/ocean system to the sub-ice-shelf cavity shape measured by nasa icebridge in Pine Island Glacier, West Antarctica.

53, 156–162.

Seroussi, H., Y. Nakayama, E. Larour, D. Menemenlis, M. Morlighem, E. Rignot, and A. Khazendar, 2017: Continued retreat of Thwaites Glacier, West Antarctica, controlled by bed topography and ocean circulation. *Geophysical Research Letters*, **44 (12)**, 6191–6199.

Shepherd, A., D. Wingham, and E. Rignot, 2004: Warm ocean is eroding West Antarctic Ice Sheet. *Geophysical Research Letters*, **31**.

Skvarca, P., 1993: Fast recession of the northern Larsen Ice Shelf monitored by space images. *Annals of Glaciology*, **17**, 317–321.

Skvarca, P., 1994: Changes and surface features of the Larsen Ice Shelf, Antarctica, derived from Landsat and Kosmos mosaics. *Annals of Glaciology*, **20**, 6–12.

Sohl, F., T. Spohn, T. Breuer, and K. Nagel, 2002: Implications from Galileo Observations on the Interior Structure and Chemistry of the Galilean Satellites. *Icarus*, **157**, 104–119, doi:10.1006/icar.2002.6828.

Sparks, W. B., K. P. Hand, M. A. McGrath, E. Bergeron, M. Cracraft, and S. E. Deustua, 2017: Probing for evidence of plumes on europa with hst/stis. *Astrophysical Journal*, **829**.

Spencer, J. R., L. K. Tamppari, T. Z. Martin, and L. D. Travis, 1999: Temperatures on Europa from Galileo photopolarimeter- radiometer: nighttime thermal anomalies. *Science*, **284**, 1514–1516, doi:10.1126/science.284.5419.1514.

Tada, H., P. C. Paris, and G. R. Irwin, 2000: *The Stress Analysis of Cracks Handbook*. Third Edition, ASME Press, New York., 2-7, 40-57 pp.

Thomas, R., E. Rignot, P. Kanagaratnam, W. Krabill, and G. Casassa, 2004: Force-perturbation analysis of Pine Island Glacier, Antarctica, suggests cause for recent acceleration. *Annals of Glaciology*, **39**, 133–138.

Thomas, R. H., 1979: Ice shelves: A review. *Journal of Glaciology*, **24 (90)**, 273–286, doi:10.3189/S0022143000014799.

Thompson, A. F., A. L. Steward, P. Spence, and K. J. Heywood, 2018: The Antarctic Slope Current in a Changing Climate. *Reviews of Geophysics*, **56**, 741–770.

Timoshenko, P., S., and N. Goodier, J., 1970: *Theory of Elasticity*. Third edition ed., Engineering Societies Monographs.

Tomczak, M., and J. S. Godfrey, 1994: *Regional Oceanography, an Introduction*. Pergamon.

Torinesi, O., M. Fily, and C. Genthon, 2003: Variability and trends of the summer melt period of Antarctic melt margins since 1980 from micro- wave sensors. *Journal of Climate*, **16**, 1047–1060.

Tufts, B., R. Greenberg, G. Hoppa, and P. Geissler, 1999: Astypalaea linea: A large-scale strike-slip fault on europa. *Icarus*, **141 (1)**, 53–64, doi:https://doi.org/10.1006/icar.1999.6168, URL https://www.sciencedirect.com/science/article/pii/S0019103599961687.

van Caspel, M., M. Schröder, O. Huhn, and H. Hellmer, 2015: Precursors of antarctic bottom water formed on the continental shelf off larsen ice shelf. *Deep Sea Research Part I: Oceanographic Research Papers*, **99**, 1–9.

Van den Broeke, M., 2005: Strong surface melting preceded collapse of Antarctic Peninsula ice shelf. *Geophysical Research Letters*, **32 (L12)**, 815–.

Van der Veen, C. J., 1998a: Fracture mechanics approach to penetration of bottom crevasses on glaciers. *Cold Regions Science and Technology*, **27**, 213–223, doi:10.1016/S0165-232X(97)00022-0.

Van der Veen, C. J., 1998b: Fracture mechanics approach to penetration of surface crevasses on glaciers. *Cold Regions Science and Technology*, **27**, 31–47, doi:10.1016/S0165-232X(97)00022-0.

van Wessem, J. M., and Coauthors, 2018: Modelling the climate and surface mass balance of polar ice sheets using racmo2 – part 2: Antarctica (1979–2016). *The Cryosphere*, **12 (4)**, 1479–1498, doi:10.5194/tc-12-1479-2018.

Vankova, I., and D. M. Holland, 2017: A model of icebergs and sea ice in a joint continuum framework. *Journal of Geophysical Research: Oceans*, **122**, 9110–9125.

Vreugdenhil, C. A., and J. R. Taylor, 2019: Stratification Effects in the Turbulent Boundary Layer beneath a Melting Ice Shelf: Insights from Resolved Large-Eddy Simulations. *Journal of Physical Oceanography*, **(49)**, 1905–1925, doi:10.1175/JPO-D-18-0252.1.

Wåhlin, A. K., and Coauthors, 2020: Ice front blocking of ocean heat transport to an Antarctic ice shelf.

Nature, **578**, 568–571, doi:10.1038/s41586-020-2014-5.

Wahr, J., Z. Selvans, M. Mullen, A. Barr, G. Collins, M. Selvans, and R. T. Pappalardo, 2009: Modeling stresses on satellites due to nonsynchronous rotation and orbital eccentricity using gravitational potential theory. *Icarus*, **200**, 188–206, doi:10.1016/j.icarus.2008.11.002.

Walker, C. C., J. Bassis, H. A. Fricker, and R. J. Czerwinski, 2013: Structural and environmental controls on Antarctic ice shelf rift propagation inferred from satellite monitoring. *Journal of Geophysical Research: Earth Surface*, **118**, 2354–2364, doi:10.1002/2013JF002742.

Walker, C. C., J. Bassis, H. A. Fricker, and R. J. Czerwinski, 2015: Observations of interannual and spatial variability in rift propagation in the Amery Ice Shelf, Antarctica, 2002-2014. *Journal of Glaciology*, **61**, 243–252, doi:10.3189/2015JoG14J151.

Walker, C. C., and A. Gardner, 2019: Evolution of ice shelf rifts: Implications for formation mechanics and morphological controls. *Earth and Planetary Science Letters*, **526**, 115 764, doi:10.1016/j.epsl.2019.115764.

Weertman, J., 1973: Can a water-filled crevasse reach the bottom surface of a glacier? *IASH Publ.*, **95**, 139–145.

Wei, W., and Coauthors, 2020: Getz ice shelf melt enhanced by freshwater discharge from beneath the west antarctic ice sheet. *The Cryosphere*, **14 (4)**, 1399–1408, doi:10.5194/tc-14-1399-2020.

Wertz, J. R., 2001: *Mission Geometry: Orbit and Constellation Design and Management: Spacecraft Orbit and Attitude Systems*. Microcosmos Press.

Xu, Y., E. Rignot, C. Menemenlis, and M. Koppes, 2012: Numerical experiments on subaqueous melting of Greenland tidewater glaciers in response to ocean warming and enhanced subglacial discharge. *Annals of Glaciology*, **53**, 229 – 234.

Yamazaki, K., S. Aoki, K. Katsumata, D. Hirano, and Y. Nakayama, 2021: Multidecadal poleward shift of the southern boundary of the antarctic circumpolar current off east antarctica. *Science Advances*, **7 (24)**, eabf8755.

Yoon, S.-T., and Coauthors, 2022: Ice front retreat reconfigures meltwater-driven gyres modulating ocean heat delivery to an Antarctic ice shelf. *Nature Communications*, **13**, 306, doi:10.1038/s41467-022-27968-8.

Zhang, H., D. Menemenlis, and I. Fenty, 2018: ECCO LLC270 Ocean-Ice State Estimate. doi:1721.1/119821.

List of Publications

First Author, Peer Reviewed:

Poinelli, M., E. Larour, J. Castillo-Rogez, and B. Vermeersen, 2019: Crevasse Propagation on Brittle Ice: Application to Cycloids on Europa. *Geophysical Research Letters*, **46**, 11 756–11 763, doi:10.1029/2019GL084033

Poinelli, M., M. Schodlok, E. Larour, M. Vizcaino, and R. Riva, 2023b: Can rifts alter ocean dynamics beneath ice shelves? *The Cryosphere*, **17 (6)**, 2261–2283, doi:10.5194/tc-17-2261-2023

Poinelli, M., Y. Nakayama, E. Larour, M. Vizcaino, and R. Riva, 2023a: Ice-front retreat controls on ocean dynamics under larsen c ice shelf, antarctica. *Geophysical Research Letters*, **50 (18)**, e2023GL104 588, doi:10.1029/2023GL104588

Co-author, Peer Reviewed:

Larour, E., E. Rignot, M. Poinelli, and B. Scheuchl, 2021: Physical processes controlling the rifting of Larsen C Ice Shelf, Antarctica, prior to the calving of iceberg A68. *Proceedings of the National Academy of Sciences of the United States of America*, **118**, doi:10.1073/pnas.2105080118

Curriculum Vitae

Born in Verona, Italy

2011–2014	Bachelor of Science in Aerospace Engineering Polytechnic University of Milan, Italy
2015–2017	Master of Science *cum laude* in Aerospace Engineering Delft University of Technology, Netherlands
2016	**Research Intern** University of Hawaii at Manoa
2017	**Graduate Research Fellow** Jet Propulsion Laboratory, California Institute of Technology
2018–present	**Doctoral Candidate** Delft University of Technology, The Netherlands
2018–present	**Research Affiliate** Jet Propulsion Laboratory, California Institute of Technology
2020–present	**Assistant Specialist** University of California, Irvine